UNIVERSITÀ DEGLI STUDI DELL'INSUBRIA
Dipartimento di Scienza e Alta Tecnologia - DiSAT

TESTING COHERENT CHANNELING PHENOMENA FOR THE K_LEVER PROJECT

LAUREA MAGISTRALE IN FISICA

CANDIDATO: Giovanni Ballerini
MATRICOLA 720977

RELATORE: Prof.ssa Michela Prest
Università degli Studi dell'Insubria

CORRELATORE: Dott. Valerio Mascagna
Università degli Studi dell'Insubria

ANNO ACCADEMICO
2017-2018

Università degli Studi dell'Insubria
Dipartimento di Scienza e Alta Tecnologia - DiSAT

Giovanni Ballerini
Testing coherent channeling phenomena for the $K_L EVER$ project
Laurea Magistrale in Fisica

RELATORE: Prof.ssa Michela Prest
CORRELATORE: Dott. Valerio Mascagna

Como, 28 Marzo 2019

A Stefano e Alberto,
due terzi fondamentali di tante avventure

L'etimologia di esperienza è illuminante.
Essa nasconde dietro a sé il verbo ex-per-ire:
l'idea di "partire da" (ex),
di "passare attraverso" (per)
e di "andare verso" (ire).
Ecco l'esperienza. Ecco la vita stessa.
– Luciano Manicardi –

CONTENTS

RIASSUNTO

La ricerca di una nuova fisica oltre il Modello Standard risulta essere, all'interno del vasto panorama della fisica moderna, una tra le avventure più entusiasmanti ed avvincenti del mondo scientifico. Sono infatti diversi i fenomeni osservati in natura che non trovano una precisa spiegazione in tale modello: l'asimmetria tra materia ed antimateria, i processi di mixing o le violazioni delle simmetrie discrete sono solo alcuni esempi.
Diversi gruppi sperimentali sono già da tempo alla ricerca delle possibili risposte, seguendo due approcci opposti e complementari tra loro. Da una parte si effettuano indagini tramite la ricerca diretta, che utilizza le più potenti macchine acceleratrici attualmente disponibili e che ancora non ha evidenziato alcun limite della struttura del Modello Standard. D'altro canto, le energie raggiunte nei moderni acceleratori non sono sufficientemente elevate per sondare direttamente possibili nuovi processi alla scala dei TeV.
Dall'altra parte, la ricerca indiretta permette di porre limiti sui parametri e sulle costanti delle nuove teorie, confrontandole allo stesso tempo con le previsioni dettate dal Modello Standard: un esempio di tale ricerca è lo studio dei decadimenti rari ed estremamente rari previsti dalla fisica dei sapori, descritti attraverso gli elementi della matrice CKM (Cabibbo-Kobayashi-Maskawa) di mixing. In questo campo, un ruolo di primo piano è quello dedicato ai kaoni, i cui decadimenti a corrente neutra (detti processi FCNC, Flavour Changing Neutral Current) risultano processi di ordine superiore al primo e coinvolgono al loro interno parametri legati al quark top: la misura delle possibili branching ratio (BR) di tali processi può dunque avere accesso alla scala di energia richiesta per l'osservazione della nuova fisica.
La proposta dell'esperimento K_LEVER (K_L Experiment for VEry Rare events), pianificato per il 2026, si cala esattamente in questo contesto: il suo obiettivo è la misura del decadimento $K_L \to \pi^0 \nu \bar{\nu}$ con una precisione del 20%, tramite la raccolta di $\sim$ 60 eventi in cinque anni di presa dati. Tra tutti i processi legati alla nuova fisica, questo decadimento è quello con lo stato finale più "pulito", dato dai due fotoni provenienti dal decadimento del π^0; il background da tenere maggiormente in considerazione è quello dovuto ai pioni neutri provenienti dal decadimento $\mathrm{K}_L \to \pi^0\pi^0$, molto più intenso di quello di interesse ($3{\times}10^7$ volte più abbondante) e che coinvolge a sua volta fotoni nello stato finale. L'uso di un fascio di K_L molto collimato e ad energia elevata (circa 40 GeV/c di momento medio) facilita l'eliminazione del segnale di fondo tramite la rivelazione dei fotoni aggiuntivi, ma pone in contemporanea alcune importanti sfide nella gestione del massiccio fondo neutro proveniente dal target primario, in particolare nel collimatore all'inizio della linea sperimentale e nel calorimetro a piccolo angolo (SAC, Small Angle Calorimeter) posto in fondo alla linea di fascio.

Una possibile soluzione al problema può essere l'utilizzo di componenti in tungsteno cristallino: nel caso del collimatore si può così ottenere una efficiente conversione dei fotoni di alta energia del fascio primario in coppie leptoniche cariche, minimizzando la dispersione della componente adronica; nel caso del SAC, si può sviluppare un detector che presenti una sensibilità variabile in funzione dell'energia e della natura delle particelle che lo attraversano, selezionando i fotoni provenienti dai decadimenti del K_L in mezzo all'intenso background neutro. Entrambi gli effetti possono essere ottenuti tramite l'interazione coerente del fotone, che attraversa il reticolo cristallino con un angolo piccolo rispetto alla direzione dei suoi piani: questo può portare ad un aumento della probabilità di interazione elettromagnetica nel mezzo, lasciandone invariata la lunghezza di interazione adronica.
Per verificare la validità di queste idee, è stato condotto un test di fattibilità sulla linea di fascio estratto H2 del Super Proton Synchrotron presso il CERN di Ginevra, durante il mese di Agosto 2018. Lo sviluppo di questa tesi si concentra su questo test, descrivendone il setup sperimentale, i dati raccolti e i risultati ottenuti nel successivo lavoro di analisi.
Un fascio di fotoni di bremsstrahlung di alta energia (fino a 120 GeV) è stato fatto incidere su due campioni di tungsteno cristallino: un sample commerciale di $10\times10\times10$ mm^3 prodotto dalla Princeton Scientific, e un cristallo ad alta purezza di 2.2 mm di spessore proveniente dai laboratori del RAS - ISSP di Mosca. Il fascio di fotoni è stato "taggato" in energia attraverso la misura del rispettivo elettrone di bremsstrahlung (deflesso su uno spettrometro multicanale da un magnete curvante); la traiettoria del fascio neutro è stata ricostruita sfruttando quella della particella carica primaria, ottenuta tramite un sistema di tracciamento ad alta precisione basato su detector a microstrip di silicio; un sistema di allineamento micrometrico, controllato dal sistema di acquisizione, ha permesso il preciso posizionamento dei campioni cristallini rispetto alla direzione delle particelle incidenti.
La prima parte del lavoro si è concentrata sullo studio delle caratteristiche del fascio primario, sulla procedura di posizionamento dei cristalli e sulla calibrazione e caratterizzazione dello spettrometro.
La seconda parte si è invece focalizzata sulle misure effettuate sui due cristalli: ogni campione è stato caratterizzato tramite lo spettro energetico e la molteplicità di particelle cariche in uscita dal campione stesso in funzione dell'energia del fotone e dell'angolo di disallineamento tra cristallo e fotone, studiando la risposta di un rivelatore a scintillazione e di un calorimetro omogeneo a luce Cherenkov posti nella sezione finale dell'apparato sperimentale. L'evidenza dell'interazione coerente nella condizione di channeling rispetto alla configurazione amorfa è stata ottenuta osservando una decrescita consistente del segnale all'interno del calorimetro, in parallelo ad un sostanziale aumento del segnale dello scintillatore: la combinazione dei due effetti è segno di un maggiore deposito di energia nel reticolo cristallino e di un maggior numero di particelle secondarie prodotte, dimostrando in questo modo la riduzione della lunghezza di radiazione "efficace" del campione nel caso assiale rispetto alla condizione amorfa e, allo stesso tempo, un maggiore sviluppo dello sciame elettromagnetico al suo interno.

A causa della non perfetta performance di alcuni dei rivelatori utilizzati nello spettrometro durante il test, i dati raccolti sono stati sottoposti ad una necessaria revisione offline via software con lo scopo di compensare tali imperfezioni (ovvero un abbassamento sistematico in funzione del tempo nel segnale in uscita dei calorimetri dello spettrometro, a causa di un difetto nel loro sistema di alimentazione). Tale software di correzione, ideato ed ottimizzato nei mesi successivi al test presso il laboratorio INSU-Lab dell'Università degli Studi dell'Insubria, risulta parte integrante di questo lavoro di tesi.
Il calcolo del fattore di enhancement della molteplicità carica in uscita dai cristalli testati, ottenuto come rapporto del segnale medio dello scintillatore nella condizione di channeling e in quella amorfa, ha ulteriormente permesso di evidenziare l'effetto previsto, ottenendo indicazioni utili per il futuro sviluppo di K_LEVER.

INTRODUCTION

The history of scientific research has always witnessed moments in which it has been considered complete, needing only further refinements in the calculation of constants and parameters. As an example, this was the situation in the early twentieth-century, just before the huge revolution that was going to start with Planck and Einstein. From that time to now, less than a century of studies has led to the development of the most effective description of the physical world, the Standard Model: with the help of the Quantum Field Theory, it has proven itself to be a great instrument for describing the measurements that are in the reach of today accelerators. Despite being the most successful theory to date, however, the Standard Model is not perfect: there are many fundamental physical phenomena that the Standard Model cannot adequately consider, predict or justify, such as gravity, asymmetry between matter and antimatter, particles masses and mixing processes, or general symmetry violations (such as the Charge-Parity violation).
For these reasons several groups are looking for "Beyond the Standard Model" new physics. The current experiments with the most powerful accelerators have not yet shown limits of the Standard Model structure: the energies reached so far are not enough to directly probe the processes imagined beyond the Standard Model (expected to be at the TeV scale). While waiting for more powerful and performing machines (HL-LHC[1], FCC[2]), researches have moved to the study of rare and extremely rare decays, and to the comparison with the predictions of the Standard Model. The basic idea of flavour physics (described by the Cabibbo-Kobayashi-Maskawa mixing matrix) is to probe these decay processes which are expected to be very sensitive to new physics, and use the results to put new limits on the parameters and constants of the new theories. A major role in this field is played by the study of heavy mesons (such as kaons) or heavy baryons decays: the former are preferred because they require much less complicated interaction modeling, experimental techniques, measurement devices and calculations. A privileged role is given to K mesons, among all the rare Flavour Changing Neutral Current (FCNC) decays: rare kaons decays branching ratios involve in fact the CKM elements linked to the top quark, thus they can access the energy scale required for the observation of new physics; since their potentiality, a vast program is being pursued with several operative experiments (NA62, KOTO), and near future ones.
In this context, the K_LEVER (K_L Experiment for VEry Rare events) proposal aims at reaching a 20% accuracy on the $K_L \to \pi^0 \nu \bar{\nu}$ branching ratio, that is one of the most sensitive to new physics among the observables in the quark-flavour sector. K_LEVER intends to start data taking in LHC Run4 (2026); the experimental layout is based

1 High Luminosity Large Hadron Collider.
2 Future Circular Collider.

on the challenging use of tungsten crystals in channeling condition: the K_LEVER collaboration wants to test the intriguing possibility of the use of a compact crystalline tungsten converter sensitive to photons and blind to hadrons, exploiting the fact that the coherent interactions of high-energy photons with a crystal lattice can lead to increased rates of electromagnetic processes while, on the other hand, the hadronic interaction length does not change. The most important background in the measurement of the $K_L \rightarrow \pi^0 \nu \bar{\nu}$ branching ratio is due to the neutral pions coming from $K_L \rightarrow \pi^0 \pi^0$, expected to be about 3×10^7 times more abundant and which also involves photons in the final state. The use of a high energy boosted K_L beam facilitates the rejection of background channels via the detection of the additional photons in the final state, but poses some challenges due to the high rate neutral beam γ/n background. The crystalline technology would be used thus in the very upstream beam collimator, to efficiently convert high-energy beam photons into charged leptonic pairs that are then swept, minimizing the scattering of the beam hadronic component, and in the Small-Angle Calorimeter (SAC), placed directly on the neutral beamline, that needs a variable insensitivity which must reject photons from K_L decays between the intense background of soft photons, neutrons and neutral hadronic contributions (such as Λ^0 decays).
In this framework K_LEVER has proposed a beamtest on the H2 beamline at the CERN[3] SPS[4] North Area, performed in August 2018. The test goals were the following:

- to observe the pair-conversion enhancement in a commercially available tungsten crystal;
- to measure the pair-conversion probability as a function of the particle impinging angle and for different photon energies, providing information to be compared with the SAC simulation results;
- to measure the pair-production probability and the spectrum of the transmitted photon energy due to a thick (10 mm) tungsten crystal at different angles (chosen respectively to maximize the pair-production enhancement and to minimize it), providing direct information about the possibility of using a crystal converter to reduce the photon flux in the neutral beam.

The K_LEVER beamtest used a high-energy (up to 120 GeV) tagged photon beam impinging on two crystalline samples (named respectively W(111) and W(100) from the major crystalline plane facing the beam), and focused on the study of the output spectrum downstream the crystals. The experimental layout was rather complicated:

- the upstream section consisted of a tracking system with two high spatial resolution silicon detectors, the trigger system (made by two plastic scintillators) and the copper target, employed as bremsstrahlung converter;

3 European Organization for Nuclear Research.
4 Super Proton Synchrotron.

- after the target a large area silicon detector was used as a beam monitor and as a single-cluster event selector, followed by a horizontal magnet to deflect the charged particles from the beamline axis;
- the last part of the experimental line was composed by two sections, one near the other: the first one, aligned with the direction of the neutral beam, included a veto scintillator, the crystalline sample with the micrometric precision positioning system, a second plastic scintillator, a silicon detector and a homogeneous Cherenkov calorimeter; the other section was placed slightly out of the beamline and consisted of two large-area silicon detectors to reconstruct the charged particle tracks deflected by the magnet and a multichannel homogeneous Cherenkov spectrometer, used to measure the deflected particle energy.

Two tungsten samples were tested: W(111), a 10×10×10 mm^3 crystalline tungsten commercial sample by Princeton Scientific and W(100), a high purity and high quality 2.2 mm thick tungsten crystal from RAS ISSP[5] - Moscow.

The first chapter of this work, after a brief introduction on the Standard Model and its inaccuracies, describes the formalism of the CKM matrix. The second part focuses on the correlation between the CKM constraints and the study of rare kaons semileptonic decay processes, together with a brief introduction of the NA62 and the KOTO experiments, to move then to the K$_L$EVER experiment goals and layout.
Chapter 2 is a short guide to crystals, describing the particle interaction in a crystalline lattice and the channeling condition, providing a detailed view of the coherent effects that channeling induces.
Chapter 3 deals with the goals and the preliminary tests performed on the H2 line at the CERN SPS-North Area during the K$_L$EVER beamtest, with a particular attention on the setup, the alignment operations and the calibration procedure. This chapter includes also the analysis developed to correct the non perfect performance of some of the detectors.
The key points of the final chapter are the analysis and the results obtained with the two crystalline samples, starting from the description of the tagged photon beam to concentrate on the two crystalline samples characterization in order to compute the increase in the electromagnetic interaction probability.

5 Russian Academy of Sciences - Institute of Solid State Physics.

1

THE K_LEVER EXPERIMENT

Everything in the Universe is found to be made from a few basic building blocks and four fundamental forces. Since the early 1970s, the Standard Model has successfully explained almost all the experimental results and precisely predicted a wide variety of phenomena concerning these particles and three of the fundamental interactions [1]. However time and experiments have demonstrated that the Standard Model seems to be missing a few elements, such as the gravity description, the "dark matter" contribution or the observed asymmetry between baryonic matter and antimatter [2]. These elements have pushed the scientific research to look for what is called the "new physics" beyond the Standard Model.

Direct observation and indirect research have always been the two sides of the same coin in the study of a new physics model; however, given the fact that the development of accelerators powerful enough requires long times, the indirect research has turned out to be the main probe to the existence of new physical phenomena, especially in the flavour physics (described by the Cabibbo-Kobayashi-Maskawa[1] mixing matrix [3]) and rare decay (such as the ones of the kaon meson) fields. In this framework, the precise measurements of the branching ratios of the flavor-changing neutral current $K \rightarrow \pi \nu \bar{\nu}$ decays (both the charged and the neutral one) can provide unique constraints on the CKM matrix unitarity and, potentially, the evidence of a new physics model, if measured with a precision better than 10% [4]. While the charged channel is currently studied at this precision level by the NA62 collaboration [5] at CERN, just a neutral mode limit has been set by the J-PARC KOTO experiment [6]; however, there is no planned upgrade to this experiment, that is mandatory to reach the 10% limit. Thus, the K_LEVER collaboration [7] is investigating the possibility of performing a measurement of the $K_L \rightarrow \pi^0 \nu \bar{\nu}$ branching ratio using a high energy secondary neutral beam at the CERN SPS starting in LHC Run4, in a complementary way to the KOTO experiment, and as a natural evolution of the NA62 program.

This chapter will first describe in a short way the Standard Model and its inaccuracies; the formalism of the CKM mechanism and the CKM matrix will be summarized in Sec. 1.1.2, while Sec. 1.1.4 is devoted to the link between the CKM constraints and the study of rare decays, in particular the ones of kaons, before concentrating on the

1 The Cabibbo-Kobayashi-Maskawa matrix is also known as the CKM matrix.

$K \rightarrow \pi \nu \bar{\nu}$ golden decays and the NA62 and the KOTO experiments. Finally, Sec. 1.2 describes the K_LEVER experiment and its goals.

1.1 TESTING THE STANDARD MODEL

The Standard Model is the gauge quantum field theory that currently describes the fundamental building blocks of the ordinary matter. The internal symmetry that defines the Standard Model is the local SU(3)×SU(2)×U(1) gauge symmetry, and the most general Lagrangian that describes its processes dynamics is both remarkably simple and powerful at the same time. It involves only 19 parameters: 6 quark masses, 3 masses of the charged leptons, 3 mixing angles in the quark sector and one CP[2] violating phase (that generate the Cabibbo-Kobayashi-Maskawa mixing matrix), 3 coupling constants, the vacuum expectation value, the Θ_{QCD} strong CP violation parameter and the Higgs boson mass. With the use of these 19 parameters and within the formalism of the Quantum Field Theory (which unifies quantum mechanics and special relativity), it is possible to describe a huge number of processes involving elementary particles, covering energies from few MeV to the highest energies reached in particle accelerators and astroparticle physics [1].
All the ordinary matter is made up of two types of particles: leptons and quarks, and their antiparticles of opposite charge. There are three types of charged leptons: electrons, muons and taus. Only the electrons are stable; the other charged leptons, which are heavier, decay in a small fraction of a second. Neutrinos, on the other side, are electrically neutral leptons with very tiny masses. There are six types of quarks: down, up, strange, charm, bottom and top. Two up-quarks and one down-quark compose a proton, while two down-quarks and one up-quark compose a neutron: protons and neutrons fused together form the atomic nucleus, which is the tiny, central core of an atom. The heavier quarks (strange, charm, bottom and top) decay into lighter quarks and other particles through the weak subnuclear interaction.
Vector gauge bosons generate the particle forces: the electromagnetic field is due to the exchange of a photon between two charged particles, while the exchange of virtual W or Z bosons between quarks and leptons produces the weak subnuclear force; gluons and quarks are linked together by the strong nuclear interaction (fig. 1.1).
The masses of the quarks, the leptons and the W and Z bosons are generated through what is known as the electroweak symmetry breaking by means of a mass field, whose carrier is the Higgs particle. However, the task is not complete: there are some new processes that show how the Standard Model seems not to be the last answer in the ordinary matter description [2].

2 The CP transformation combines charge coniugation C with parity P; under C, particles and antiparticles are interchanged, by conjugating all internal quantum numbers. Under P, the handedness of space is reversed. Thus, CP violation is studied by proving that a process is able to happen with a different rate with respect to its antimatter counterpart [8].

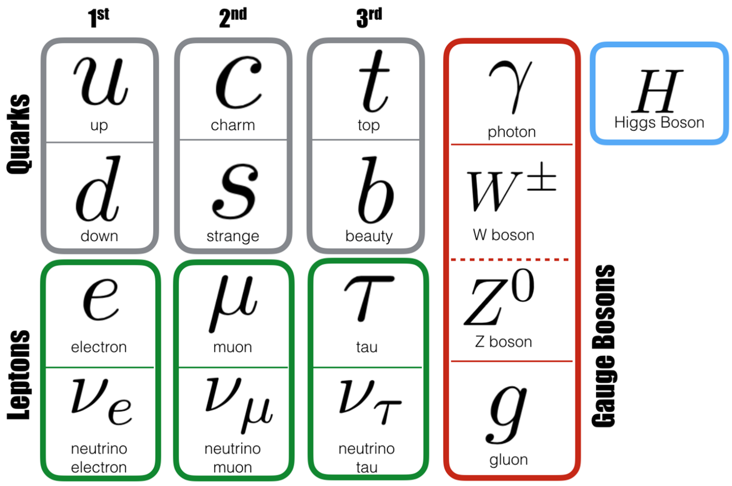

Figure 1.1: The Standard Model of elementary particles [9].

1.1.1 A BEAUTIFUL BUT INCOMPLETE THEORY

Many physics processes are only partially described by or are completely excluded from the Standard Model framework:

- it does not include gravity, one of the four fundamental forces, failing to explain why this force is so much weaker (10^{-39} times) than the electromagnetic or nuclear ones [10];
- it lacks robustness at higher energy (as the ordinary quantum mechanics theory fails in the relativistic limit, *i.e.* at arbitrarily short distances), where its equations start getting waver [11];
- it does not clearly justify the wide mass spectrum among the matter building particles [12];
- it gives an incomplete picture of the content of the Universe, describing only the visible matter and neglecting the "dark matter" contribution, that manifests itself through its gravitational effects [13];
- it does not solve the baryon asymmetry problem, that is the unexpected imbalance between the baryonic ordinary matter and the antibaryonic one in the observable Universe [14].

Thus the majority of the particle physics community is searching for physics beyond the Standard Model. There are three main ways, complementary to each other, to obtain the experimental evidence of the incompleteness of the Standard Model, and to find evidence of new physics beyond it:

- the direct discovery, based on the experimental evidence, of a new particle and/or new interactions and decays not previously observed;

- the observation of very high energy astrophysical phenomena (such as ultra high energy neutrinos [15]);

- the indirect investigation of new interactions in high order processes and the test of their deviations from the Standard Model predictions.

Although the direct research scenario has the advantage to be the cleanest way to find new physics, it is limited by the energy and the luminosity of the modern particle colliders (fig. 1.2) [16]; thus the indirect observation of new physics processes becomes the portal used to predict the existence of particles, before a new experiment with high enough energy could produce them. By the indirect observation one can probe the radiative corrections to perturbatively calculable processes, as well as the rare transition decays which are either suppressed or forbidden in the Standard Model. Both these scenarios carry the advantage of being able to explore the existence of new physics at very high energy scales [17]. In this framework, the study of the rare decay transition rates (usually located in the field of heavy mesons, such as B^0, D^0, kaons or heavy baryons) acquires a major role in the search of new physics beyond the Standard Model.

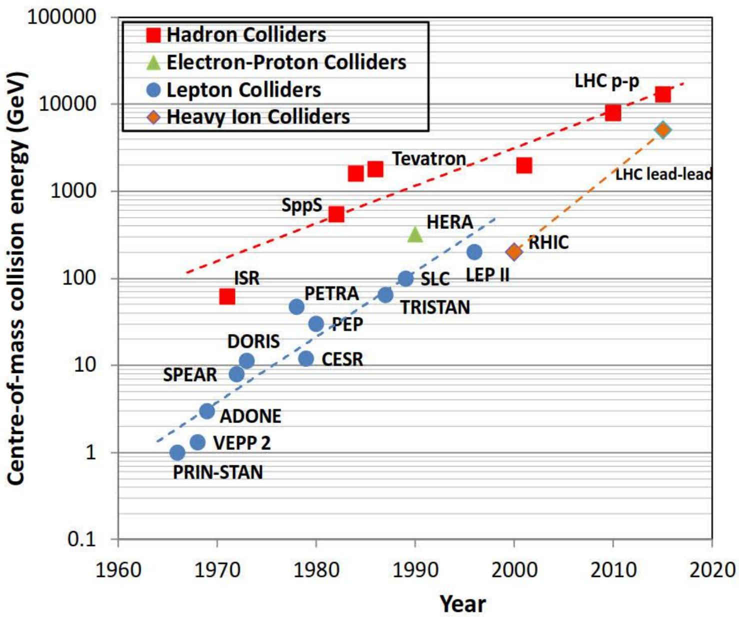

Figure 1.2: The centre-of-mass energy of several particle colliders versus time [18].

1.1.2 RARE DECAYS AND THE QUARK MIXING

The rare decays involved in the search for new physics processes are strictly related to the weak interaction description, because of its most intriguing effect: flavor changing [19]. A neutron, that is heavier than a proton, may decay into a proton only changing the flavor (type) of one of its two down quarks to an up quark. In the same way, a kaon can decay into a pion, and so on. The concept of flavour change is at the base of the study of rare decays. The very first description of the mixing process has been given by Nicola Cabibbo in 1963, to explain two different phenomena:

- the magnitudes of the transition between a quark up and a quark down (such as the β-decay of the neutron), of the ones involving an electron and an electronic neutrino and of the ones involving a muon and a muonic neutrino appear to be the same [3];
- the transitions involving a $\Delta S = 1$ strangeness[3] variation have decay rates equal to one fourth of those with $\Delta S = 0$ [19].

Starting from the idea proposed by Murray Gell-Mann and Maurice Lévy for the strong interaction [20], Cabibbo postulated a weak universality to solve the first problem, and introduced a unitarity mixing matrix and a mixing angle θ_c (the Cabibbo mixing angle) between the d and s quarks (eigenstates of the nuclear strong interaction) to solve the second problem [21]. The d' quark eigenstate of the weak interaction does not correspond to the d strong eigenstate, but it is a linear combination of the latter and the strong s quark according to the relation:

$$d' = \cos\theta_c \cdot d + \sin\theta_c \cdot s \tag{1.1}$$

In this way θ_c denotes the mismatch between the flavour symmetry breaking directions chosen by the strong and weak interactions. According to the current-current amplitude model for the weak interaction[4] and with only three quark flavours, Cabibbo postulated that the corresponding charged current was given by:

$$J_\mu = \bar{u}(1+\gamma_5)(\cos\theta_c \cdot d + \sin\theta_c \cdot s) \tag{1.2}$$

where $\gamma_5 = i\gamma^0\gamma^1\gamma^2\gamma^3$ is the product of the four γ Dirac matrices. The latter expression suggests that the u quark is coupled to the weak d' quark and not to the strong d eigenstate. In this picture the d' orthogonal combination, namely $s' = -\sin\theta_c \cdot d + \cos\theta_c \cdot s$, remains uncoupled.

3 The strangeness of a particle is a quantum number defined as:

$$S = -(n_s - n_{\bar{s}})$$

where n_s is the number of strange quarks and $n_{\bar{s}}$ is the number of strange antiquarks in the particle itself.

4 The structure of the weak interaction currents is of the type of vector minus axial-vector, also expressed as V-A interaction [22].

A prediction of the Cabibbo mixing matrix was the existence of the Flavour Changing Neutral Currents (FCNC), weak interactions that change the flavor of a fermion current without altering its electric charge; in other words, by means of a FCNC process a strange quark would become a down quark. FCNC processes were thought to be responsible of a great variety of strangeness-changing decays; however, the expected rates for these decays were significantly suppressed in the experimental measurements [19]. The introduction of the charm quark c in 1970 by Sheldon Lee Glashow, John Iliopoulos and Luciano Maiani [23] led to form two left-handed doublets:

$$\begin{pmatrix} u \\ d' \end{pmatrix} \tag{1.3}$$

and

$$\begin{pmatrix} c \\ s' \end{pmatrix} \tag{1.4}$$

so that the weak eigenstates d' and s' could be expressed in a matrix notation as:

$$\begin{pmatrix} d' \\ s' \end{pmatrix} = \begin{pmatrix} \cos\theta_c & \sin\theta_c \\ -\sin\theta_c & \cos\theta_c \end{pmatrix} \begin{pmatrix} d \\ s \end{pmatrix} \tag{1.5}$$

The orthogonality of the mixing matrix guaranteed the observed suppression of the strangeness-flavor changing neutral current: the plain destructive interference effects in neutral current loop diagrams (also known as the GIM mechanism [24]) led in fact to their complete cancellation, and thus a null effect (fig. 1.3). The θ_c Cabibbo angle became thus a full description of the 2-generation mixing. The new full charged weak current was given by:

$$J_\mu(x) = \bar{u}(x)\gamma_\mu(1+\gamma_5)d'(x) + \bar{c}(x)\gamma_\mu(1+\gamma_5)s'(x) \tag{1.6}$$

A new problem appeared in 1964, when the CP violation was discovered in the observation of the odd-CP $K_L \to \pi^+\pi^-$ decay [26], that couldn't be explained in the framework of the Cabibbo theory, due to the absence of a CP non-zero phase. The problem was overcome in 1973 by Kobayashi and Maskawa, with the necessary addition of a third generation of quarks (t and b) that extended the two-flavor model: thus the flavour mixing in the quark sector and the CP violation in the weak interaction were unified with a single theory [27].
Considering three left handed quark doublets, the mixing of the quark states is now given by a 3×3 unitarity matrix (known as the Cabibbo-Kobayashi-Maskawa matrix) which characterizes the charged current interactions of the quark sector (fig. 1.4):

$$J_\mu^{cc} = (\bar{u}, \bar{c}, \bar{t})\gamma_\mu \cdot \begin{pmatrix} V_{ud} & V_{us} & V_{ub} \\ V_{cd} & V_{cs} & V_{cd} \\ V_{td} & V_{ts} & V_{tb} \end{pmatrix} \begin{pmatrix} d \\ s \\ b \end{pmatrix} \tag{1.7}$$

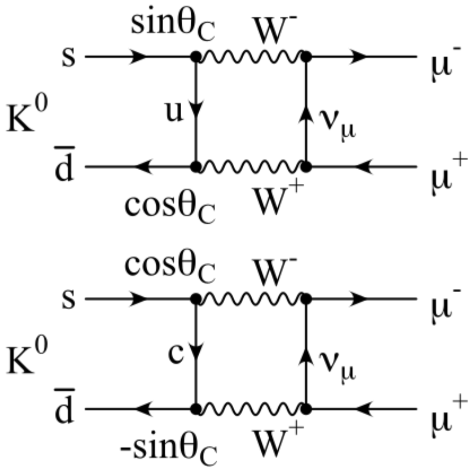

Figure 1.3: The GIM mechanism in the rare $K_L \to \mu^+\mu^-$ decay: the minus sign between the two interfering box diagrams (itself a consequence of the unitarity of the Cabibbo matrix) would lead to its complete cancellation [25].

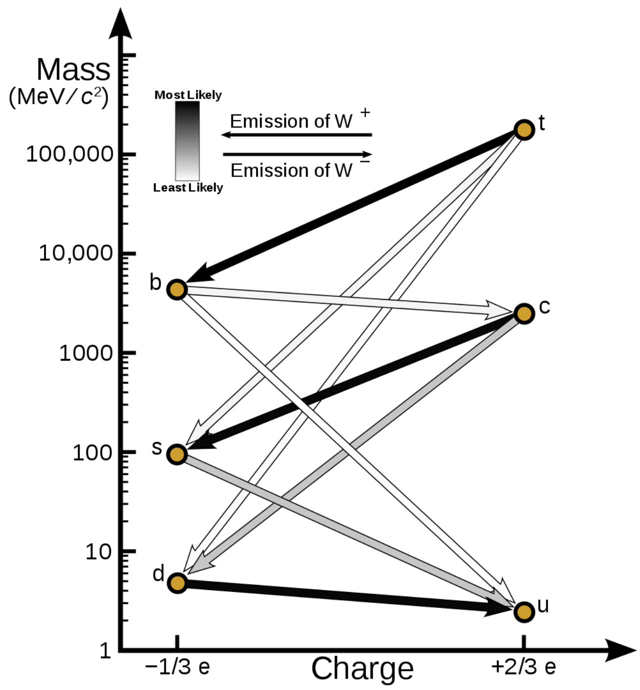

Figure 1.4: A diagram depicting the various charged decay routes due to the weak interaction; the intensity of the lines is given by the CKM parameters [28].

The CKM matrix is characterized by three angles and one phase, that gives the CP violation effects; a standard representation is [29]:

$$V_{CKM} = \begin{pmatrix} 1 & 0 & 0 \\ 0 & c_{23} & s_{23} \\ 0 & -s_{23} & c_{23} \end{pmatrix} \begin{pmatrix} c_{13} & 0 & s_{13}e^{i\delta} \\ 0 & 1 & 0 \\ -s_{13}e^{i\delta} & 0 & c_{13} \end{pmatrix} \begin{pmatrix} c_{12} & s_{12} & 0 \\ -s_{12} & c_{12} & 0 \\ 0 & 0 & 1 \end{pmatrix} \tag{1.8}$$

where $s_{ij} = \sin\theta_{ij}$, $c_{ij} = \cos\theta_{ij}$ and δ is the CP violation phase. It is customary to express the CKM matrix in terms of four Wolfenstein parameters (λ, A, ρ, η) [30], defined as:

$$\begin{aligned} s_{12} = \lambda &= \frac{|V_{us}|}{\sqrt{|V_{ud}|^2 + |V_{us}|^2}} \\ s_{23} = A\lambda^2 &= \lambda \frac{|V_{cb}|}{|V_{us}|} \\ s_{13}e^{i\delta} &= A\lambda^3(\rho + i\eta) = \frac{A\lambda^3(\bar{\rho} + i\bar{\eta})\sqrt{1 - A^2\lambda^4}}{\sqrt{1-\lambda^2}[1 - A^2\lambda^4(\bar{\rho} + i\bar{\eta})]} \end{aligned} \tag{1.9}$$

with $\lambda = |V_{us}| = 0.22$ and η representing the CP violating phase. The CKM matrix can be written as:

$$V_{CKM} = \begin{pmatrix} 1 - \lambda^2/2 & \lambda & A\lambda^3(\rho - i\eta) \\ -\lambda & 1 - \lambda^2/2 & A\lambda^2 \\ A\lambda^3(1 - \rho - i\eta) & -A\lambda^2 & 1 \end{pmatrix} + O(\lambda^4) \tag{1.10}$$

The unitarity of the CKM matrix imposes $\Sigma_i V_{ij} V^*_{ik} = \delta_{jk}$ and $\Sigma_j V_{ij} V^*_{kj} = \delta_{ik}$. The six combinations can be represented as triangles in the complex plane; the most commonly used arises from:

$$V_{ud}V^*_{ub} + V_{cd}V^*_{cb} + V_{td}V^*_{tb} = 0 \tag{1.11}$$

rescaling it by $|V_{cd}V^*_{cb}| = A\lambda^3$, as shown in fig. 1.5. The CKM matrix vertices are (0,0), (1,0) and, due to the definition of the Wolfenstein parametrization, $(\bar{\rho},\bar{\eta})$.

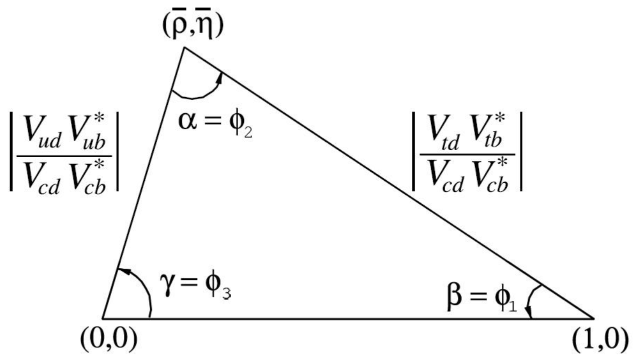

Figure 1.5: A sketch of the unitarity triangle [31].

The (0,0)-(1,0), (0,0)-($\bar{\rho}$,$\bar{\eta}$) and (1,0)-($\bar{\rho}$,$\bar{\eta}$) lengths are equal respectively to:

$$1 \tag{1.12}$$
$$R_b = \sqrt{\bar{\rho}^2 + \bar{\eta}^2} = (1 - \frac{\lambda^2}{2})|\frac{V_{ub}}{V_{cb}}|$$
$$R_t = \sqrt{(1-\bar{\rho})^2 + \bar{\eta}^2} = \frac{1}{\lambda}|\frac{V_{td}}{V_{cb}}|$$

1.1.3 TREE, PENGUIN AND BOX PROCESSES

Since each decay due to the weak interaction involves the CKM matrix terms in its rate expression, the study of the decay rate allows to overconstrain the elements of the matrix itself. Thanks to the large number of possible decay combinations, many independent measurements can be done, comparing their results in the ($\bar{\rho}$,$\bar{\eta}$) plane, as shown in fig. 1.6. It is essential to calculate as many branching ratios as possible, checking if they all can be described by the same set of the (λ,A,ρ,η) Wolfenstein parameters.
In the language of the unitarity triangle, this means that the various curves in the ($\bar{\rho}$,$\bar{\eta}$) plane extracted from each different decay should cross each other at a single point. The amplitudes for the decays of mesons composed of a heavy quark and a light quark, such as K and B mesons, are generally classified, according to the weak diagram topology, in the so called tree and loop (also known as penguin, or box) diagrams [32].
However, due to the GIM mechanism, at a first order correction only tree diagrams (fig. 1.7) contribute to the decay amplitude of the corresponding meson, and none can change the CKM parameters determination, due to the presence of the same CKM element and the same CP weak phase. On the other hand, in box and penguin diagrams (fig. 1.8) the decay rate is a function of many different combinations of the CKM elements, depending on the quark involved within the loop. But in the loop diagrams of the Standard Model, particles can be replaced by new particles: as a result, the rates and the kinematic distributions of FCNC decays (that can occur only at a loop level) can significantly deviate from the Standard Model predictions. In this way, processes suppressed at a tree level and dominated by a loop-level contribution in the Standard Model framework are particularly sensitive to new physics, and they could change the constraints of the unitarity triangle: that is, the different curves based on the Standard Model expressions, will not cross each other at a single point and the (α,β,γ) angles extracted from CP asymmetries in B-decays will disagree with the ones determined from rare K and B decays.

1.1.4 KAON DECAYS: A PROBE FOR NEW PHYSICS

Among all the rare decay processes, the kaon decays provide the cleanest environment where to search for new physics. Since 1949, when K mesons were discovered,

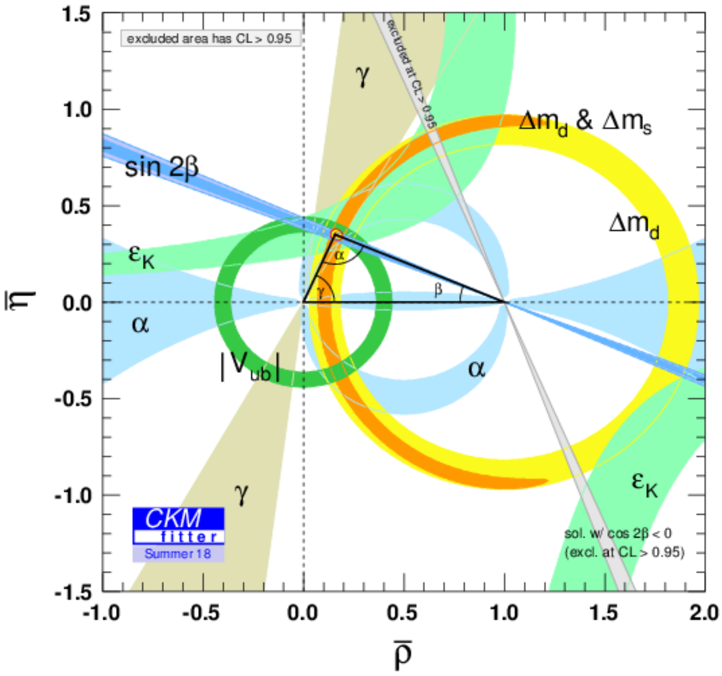

Figure 1.6: Constraints on the unitarity triangle in the ($\bar{\rho}$,$\bar{\eta}$) plane [33].

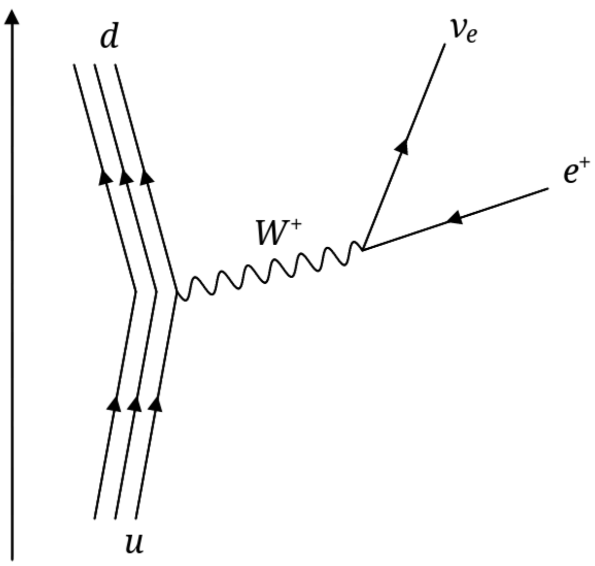

Figure 1.7: The β^+ decay Feynman diagram, as an example of a tree process.

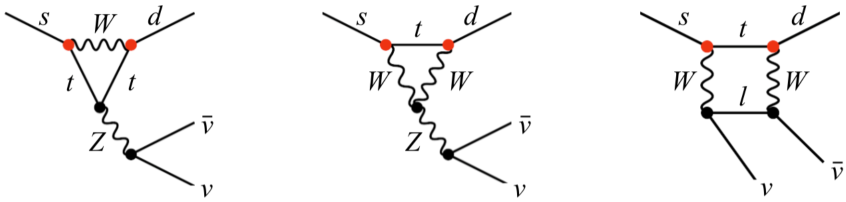

Figure 1.8: The neutral kaon penguin and box diagrams, as an example of loop processes.

kaon physics has represented one of the richest sources of information in the study of fundamental interactions. kaons are particles consisting of a strange quark and an up or down antiquark (or alternatively, a strange antiquark and an up or down quark), which are bound together by the strong force. kaons can have one unit of electric charge, or they can be neutral: both charged and neutral kaons played a great role in the history of particle physics, and may yet be the source of new discoveries [34].
One of the most encouraging features in the study of kaons is the reachable energy scale (up to $\approx 3.2\times 10^5$ TeV) involved in their decay processes [35]. In the neutral kaon mixing system, FCNC processes can arise only at the loop level and they are suppressed by loop factors and small CKM elements related to the top quark. In this way, measuring kaons low energy flavor observables may give information on the new physics flavor couplings of the heavier quark, and on the new physics mass scale (fig. 1.9).

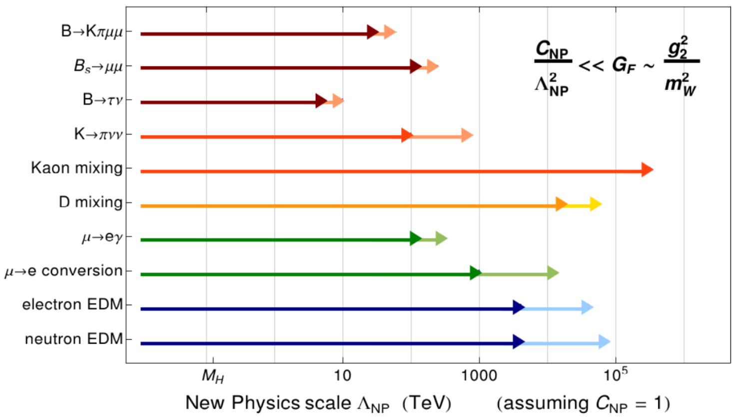

Figure 1.9: The Λ_{NP} energy scale of a possible new physics, achievable with the study of different rare decay processes; the direct research currently has it highest value at $\approx$10 TeV (LHC) [36].

From the study of each possible decay model of the K mesons (both neutral and charged) it is possible to put constraints on the unitarity triangle, and thus to obtain information about many elements of the CKM matrix; a summary of the possible measurements linked to the corresponding CKM constraint is shown in fig. 1.10.

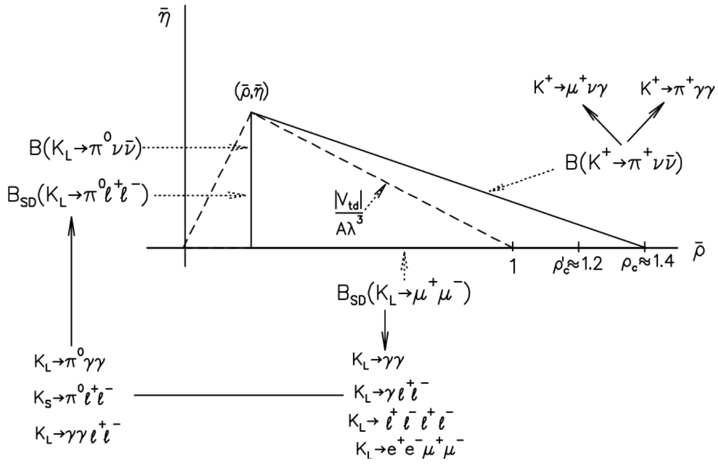

Figure 1.10: Role of rare kaon decays in determining the unitarity triangle; the solid arrows point to auxiliary modes needed to interpret the main results and the potential backgrounds [37].

THE K$\to\pi\nu\bar{\nu}$ GOLDEN MODE

The branching ratios for the K$\to\pi\nu\bar{\nu}$ decays are, between all the observables in the quark-flavor sector, the most sensitive to new physics. Both the charged decay and the neutral one are FCNC transitions, and since they are suppressed at the tree-level by the GIM mechanism and the CKM hierarchy within the Standard Model, the relative probability of their occurrence is extremely small ($\approx 10^{-11}$ [4]). Because of the dominance of the diagrams with top quark loops, the lack of contributions from intermediate photons, and the fact that the hadronic matrix element can be obtained from K_{e3}[5] decay data, the predicted Standard Model rates can be calculated very precisely to within 20% [4]:

$$BR(K^+\to\pi^+\nu\bar{\nu}) = (8.39\pm0.30)\times10^{-11}\cdot\left[\frac{|V_{cb}|}{0.0407}\right]^{2.8}\cdot\left[\frac{\gamma}{73.2^o}\right]^{0.74}$$

$$BR(K_L\to\pi^0\nu\bar{\nu}) = (3.36\pm0.05)\times10^{-11}\cdot\left[\frac{|V_{ub}|}{3.88\times10^{-3}}\right]^{2}\cdot\left[\frac{|V_{cb}|}{0.0407}\right]^{2}\cdot\left[\frac{\sin\gamma}{\sin(73.2^o)}\right]^{2}$$

where γ is the CKM angle. The uncertainties are dominated by the external contributions from the V_{cb} and V_{ub} CKM elements, and the non-parametric theoretical uncertainties are about 3.5% and 1.5%, respectively. Measurements with a precision of the order of 10% can be used as a probe for new physics scenarios [4].
The $K^+\to\pi^+\nu\bar{\nu}$ process is CP conserving, while $K_L\to\pi^0\nu\bar{\nu}$ is CP violated. Since the Standard Model does not explain the domination of matter on antimatter, a precise measurement of the CKM parameter describing CP violation is a key element for the

5 The $K^+\to\pi^0e^+\nu$ (K_{e3}) has BR=$(0.9641\pm^{0.014}_{0.012})$% [38].

study of this phenomenon and the verification of the Standard Model. In addition, a measurement of the amplitude of the $K^+ \to \pi^+\nu\bar{\nu}$ process implies a constraint on the R_t parameter of the unitarity triangle and, correspondingly, on the V_{td} parameter of the CKM matrix; on the other hand, the value of the $K_L \to \pi^0\nu\bar{\nu}$ amplitude is directly proportional to the η parameter of the CKM matrix (in the Wolfenstein parametrization), and thus to the height of the unitarity triangle (fig. 1.11). It is important to measure both decay modes, since different new physics models affect the rates for each channel, as shown in fig. 1.12 [39].

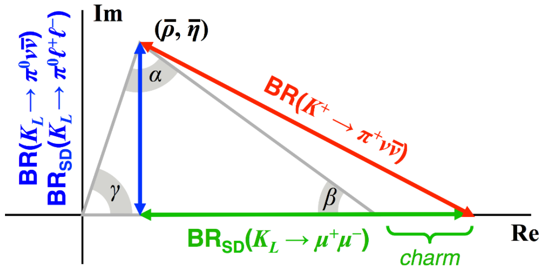

Figure 1.11: The $K \to \pi\nu\bar{\nu}$ decay constraints on the unitarity triangle [40].

$K^+ \to \pi^+\nu\bar{\nu}$: THE NA62 EXPERIMENT

One of the most promising experiments that currently studies the charged $K^+ \to \pi^+\nu\bar{\nu}$ decay is the NA62 experiment [5] (fig. 1.13) at the CERN SPS; its main goal is to measure the BR for the charged channel with a 10% precision, collecting 100 signal events in two years of data taking. NA62 is a fixed-target experiment installed in the CERN North Area, that uses a secondary K^+ beam (from the 400 GeV/c SPS protons) with mean momentum of 70 GeV/c. Its schematic setup is drawn in fig. 1.14. The NA62 experiment can be seen as a follower of the physical program of the NA48 experiment [41], inheriting some of its hardware elements (such as the beamline and the LKr calorimeter). The kinematic signature of the $K^+ \to \pi^+\nu\bar{\nu}$ process is rather simple:

- the π^+ meson is registered with a Ring Imaging Cherenkov Detector (RICH) counter, and it is associated with the incoming K^+ by matching them in a time gate. In this framework, in addition to the RICH, two detectors with excellent time resolution have been built: the CEDAR differential Cherenkov counter (with a time resolution $\sigma_t = 100$ ps), and the GigaTracker ($\sigma_t = 200$ ps per station) [42][43];
- the K^+ momentum and track are detected by means of the GigaTracker;
- a Straw Tracker Spectrometer [44] measures the momentum of the π^+, the only visible particle in the final state of the decay;

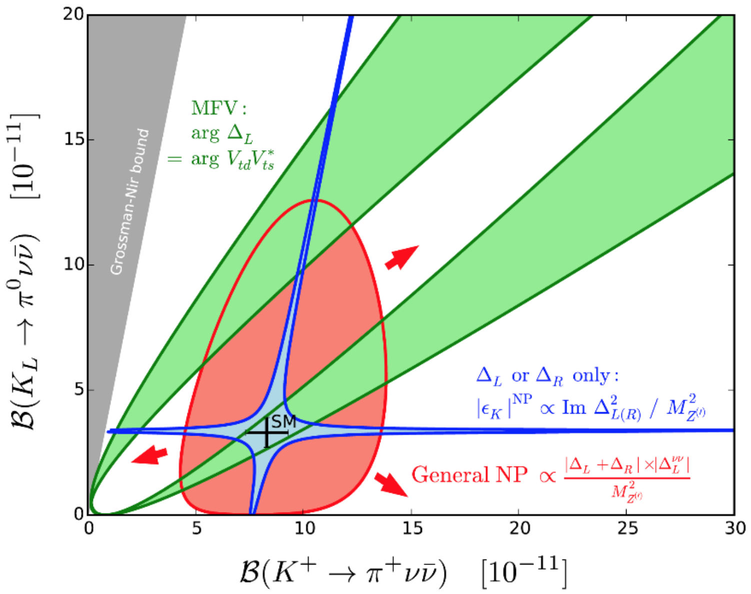

Figure 1.12: The K→ $\pi\nu\bar{\nu}$ charged and neutral decays correlation in the Standard Model; if the new physics has a CKM-like structure of flavor interactions, with only couplings to left-handed quark currents, the two branching ratio values will lie along the green band. If the new physics contains only left-handed or right-handed couplings to the quark currents, then the branching ratios must lie on one of the two branches of the blue cross-shaped region, induced by the constraint from the $K\bar{K}$ mixing parameter ϵ_K. The red region illustrates the lack of correlation for models with general Littlest Higgs model without T-parity (LH) and right-handed new physics couplings [39].

- the missing mass (due to the escaping neutrinos) of the event should belong to the signal region;
- any additional particle with respect to the decay model should be detected by the hermetic veto system.

Figure 1.13: A picture of the NA62 experiment [45].

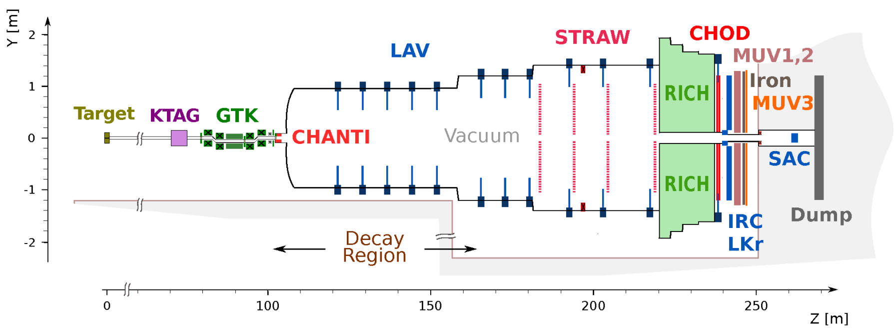

Figure 1.14: Schematic section of the NA62 experimental setup; the main elements for the detection of the K^+ decay products are located along a 150 m long region, starting 121 m downstream of the kaon production target [46].

$K_L \to \pi^0 \nu \bar{\nu}$: THE KOTO EXPERIMENT

The KOTO experiment (fig. 1.15) at J-PARC[6] is the only experiment currently studying the $K_L \to \pi^0 \nu \bar{\nu}$ decay, following the tradition of the E391 KEK[7] experiment [6].

6 Japan Proton Accelerator Research Complex [47].
7 KEK - High Energy Accelerator Research Organization [48].

A schematic layout is drawn in fig. 1.16. The experiment uses a highly collimated, low-energy (mean momentum of 2.1 GeV/c) kaon beam, a very high performance hermetic calorimeter and an efficient photon veto system. The kinematic signature of the signal candidate event is based on the following conditions:

- two photons (the only visible particles in the final state) produced by the $\pi_0 \to \gamma\gamma$ decay[8] should be identified in the main CsI calorimeter;
- a hermetic veto system surrounding the experimental decay region rejects any additional particles;
- the reconstructed decay vertex has to be located in the decay volume;
- the reconstructed transverse momentum and angle of the two γs should lie inside the allowed kinematical boundaries.

KOTO has recently obtained the limit BR($K_L \to \pi^0\nu\bar{\nu}$) $<3\times10^{-9}$ (at 90% confidence level), with an expected background of 0.42±0.18 events and no candidate events observed [50]. To reach the single-event sensitivity for the Standard Model decay and thus a 10% precision, KOTO would need about a factor of 40 more data, that means increasing the primary beam power over 100 kW with a secondary K_L mean momentum of 5.2 GeV/c. However, a KOTO step-2 upgrade would require the construction of a completely new detector several times larger than the present one; at the moment there is no such proposal.

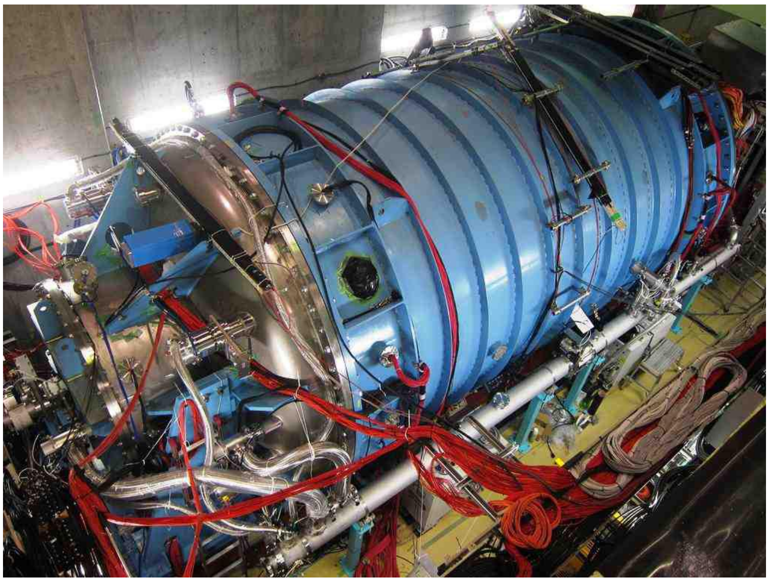

Figure 1.15: A picture of the KOTO experiment vessel [6].

8 The $\pi_0 \to \gamma\gamma$ decay has a BR = (98.823±0.034)% and a mean lifetime $\tau = 8.4\pm0.4\times10^{-17}$ s [49].

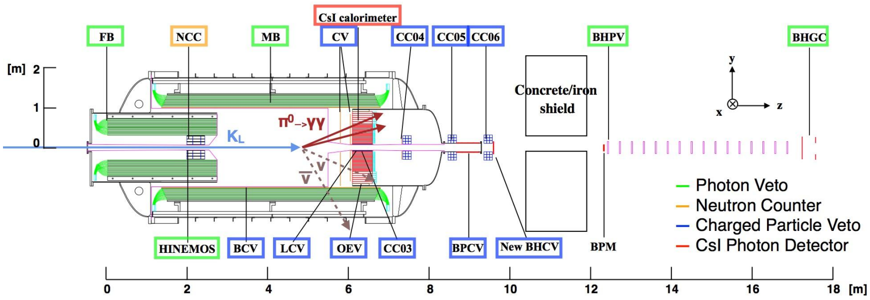

Figure 1.16: Schematic section of the KOTO experimental setup [51].

1.2 A K_L EXPERIMENT FOR VERY RARE EVENTS

In the field of neutral kaons rare decays, the K_LEVER collaboration [52] is investigating the possibility of performing a measurement of the $K_L \to \pi^0 \nu \bar{\nu}$ branching ratio, using a high energy secondary neutral beam at the CERN SPS. The K_LEVER experiment intends to be the natural evolution of the multi-decade North Area program in kaon physics: in fact it will use the NA62 experimental area, and some of its components and detectors. The decay measurement technique will be complementary to the one of the KOTO experiment at J-PARC, and will provide a comparable sensitivity, studying the branching ratio by means of a neutral high energy neutral kaon beam (≈40 GeV/c of average momentum) generated by the SPS primary proton beam. The timescale for research and development, construction, and commissioning of the new experiment will cover the next few years, assuming that the experiment would be ready at the start of LHC Run4 (early 2026, fig. 1.17).
The main goal to be reached by the collaboration is a sensitivity of about 60 $K_L \to \pi^0 \nu \bar{\nu}$ decay events over the total K_L primary flux in five years of data taking, to be compared with the branching ratio foreseen by the Standard Model: with a signal to background ratio of 1, the experiment would obtain a relative uncertainty of $\delta_{BR}/BR(K_L \to \pi^0 \nu \bar{\nu})$ =20% with respect to the Standard Model branching ratio. This would demonstrate a discrepancy with 5σ significance if the true rate is a bit more than twice or less than one-quarter of the predicted Standard Model rate, or with 3σ significance if the true rate is less than half of the Standard Model one (fig. 1.18).

1.2.1 THE GENERAL LAYOUT

The experimental signature of the $K_L \to \pi^0 \nu \bar{\nu}$ decay consists of two high energy photons with unbalanced transverse momentum due to the escaping neutrinos, in an event in which there are no additional particles (fig. 1.19). The only available kinematic constraint is the two-photon invariant mass, which needs to be equal to $M(\gamma\gamma) = m(\pi_0)$.

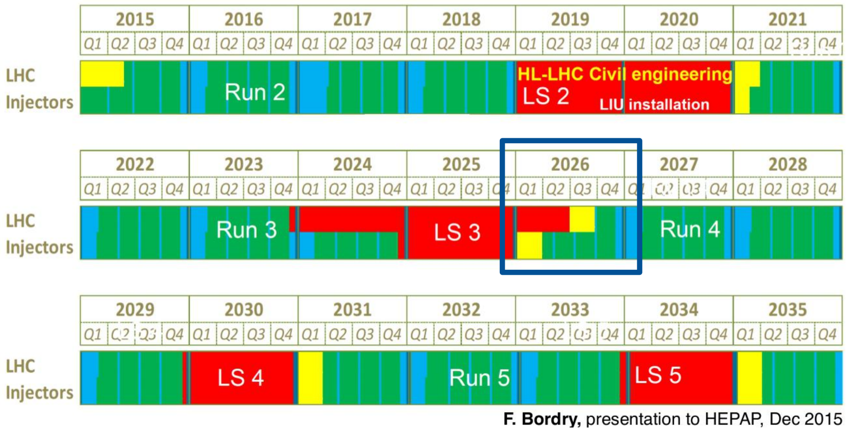

Figure 1.17: The planned LHC schedule beyond LS1; K_LEVER should be ready at the start of LHC Run4, highlighted by the blue box [53].

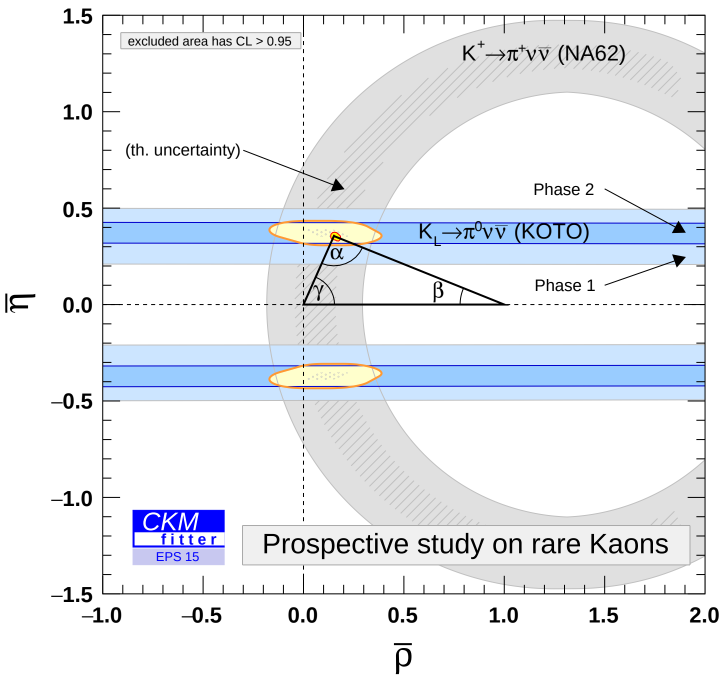

Figure 1.18: Constraints in the ($\bar{\rho}$,$\bar{\eta}$) plane, using a prospective scenario for the NA62 (light gray) and the KOTO (phase 1, lighter blue and phase 2, darker blue) results; the current ϵ_k value resolves ambiguities on the selection of the unitarity triangle vertex. K_LEVER wants to improve the measurement of the η CKM parameter, in a complementary way to the KOTO experiment [54].

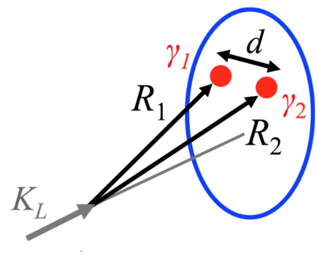

Figure 1.19: A schematic view of the $K_L \to \pi^0 \nu \bar{\nu}$ decay; R_1 and R_2 are the photons trajectories from the π^0 decay, while the escaping neutrinos are not shown.

The most insidious background is due to the neutral pions coming from $K_L \to \pi^0 \pi^0$, expected to be about 3×10^7 times more abundant than the one of interest, which also involves photons in the final state. The boost from the high-energy beam on one hand facilitates the rejection of background channels by the detection of the additional photons in the final state, but on the other poses some challenges due to the neutral beam γ/n background: thus stringent requirements are needed on the insensitivity of the active components placed near the beamline, which must reject photons from K_L decays escaping through the beam exit between the intense background of soft photons and neutrons. Also the background signal due to $\Lambda^0 \to n\pi^0$ decays must be kept under control.

The foreseen experimental setup, shown in fig. 1.20, is the following:

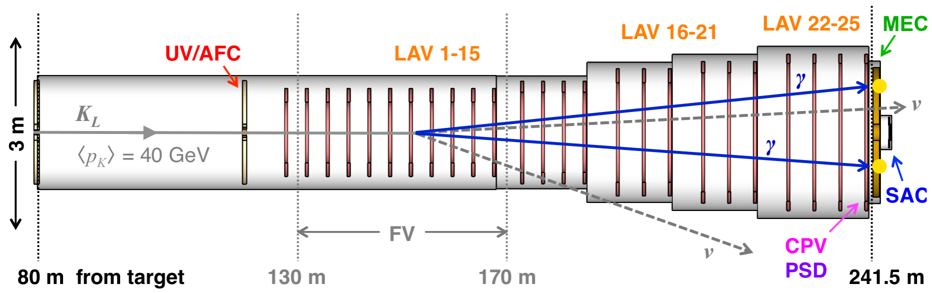

Figure 1.20: The K_LEVER foreseen setup [7].

- the very first upstream section is the primary beryllium target on which protons from the CERN SPS impact, producing the neutral beam and other secondaries;
- a vertical magnet placed immediately after the target deflects the primary protons below 5.6 mrad, where they are stopped by a TAX[9] collimator (with a hole to allow the passage of the neutral beam) together with the rest of the charged particles;

9 Target Attenuator to eXperimental areas.

- two collimation stations (40 m and 80 m downstream the target respectively) collimate, define and further clean the beam; both are followed by horizontal sweeping magnets;
- the final collimation stage is the Active Final Collimator (AFC), incorporated into the Upstream Veto (UV, rejecting $K_L \to \pi^0\pi^0$ decays in the 40 m upstream section) at z = 120 m;
- in the downstream part of the apparatus, a cylindrical structure with increasing diameter in z (in which the vacuum is created) contains 25 large-angle photon veto stations which measure the energy of the photons from the beam decays;
- at the end of the structure, the Main Electromagnetic Calorimeter (MEC) is used to reconstruct the π^0 decays from the signal events, and to reject the events with additional photons; a PreShower Detector (PSD) placed just before the MEC measures the directions of the photons impinging on the MEC itself;
- a Charged-Particle Veto (CPV) rejects the final state electrons of the large BR K_{e3} decay channel, that can be mistaken for photons;
- a Small-Angle Calorimeter (SAC) is placed directly on the neutral beamline, rejecting photons from K_L decays that would otherwise escape via the downstream beam exit, providing at the same time a good γ/n discrimination.

1.2.2 THE NEUTRAL BEAM SOURCE

The 400 GeV/c primary proton beam impinges on a 400 mm long, 2 mm radius beryllium rod target with an angle of 2.4 mrad, optimizing the K_L to neutron and photon flux ratios. The neutral secondary beam will be produced at an angle of 8 mrad with an opening angle of 0.4 mrad, according to the FLUKA and GEANT4 simulations[10]: the choice of the production angle increases the K_L production with high momentum at small angle improving K_L/n and K_L/Λ ratios at larger angles (fig. 1.21).

The neutral beam has a mean K_L momentum of 40 GeV/c, resulting in a decay fiducial volume from 130 to 170 m (with an acceptance of 4%) downstream of the target position due to the K_L decay time ($5.116 \pm 0.021 \times 10^{-8}$ s) and a K_L yield of $2 \cdot 10^{-5}$ per proton on target. With a selection efficiency of 5%, the collection of 60 SM events would require a six-fold increase in the current primary intensity with respect to the NA62 one. Feasibility tests about an extensive upgrade of the NA62 beamline (the P42 beamline, the TCC8 target gallery and the ECN3 experimental cavern of the CERN-Prevessin site, fig. 1.22) to handle the needed intensity have been studied by the Conventional Beams working group in the framework of Physics Beyond Colliders [57], and preliminary indications are positive.

10 FLUKA and GEANT4 (for GEometry ANd Tracking) are general purpose tools for the simulation of the passage of particles through matter using Monte Carlo methods [55]-[56].

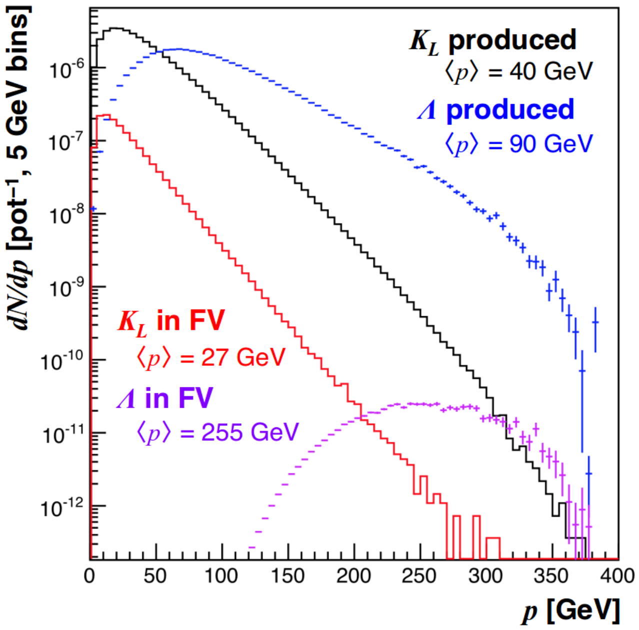

Figure 1.21: The K_L neutral beam flux compared with Λ^0 hadronic contribution as modeled in the FLUKA simulation [7].

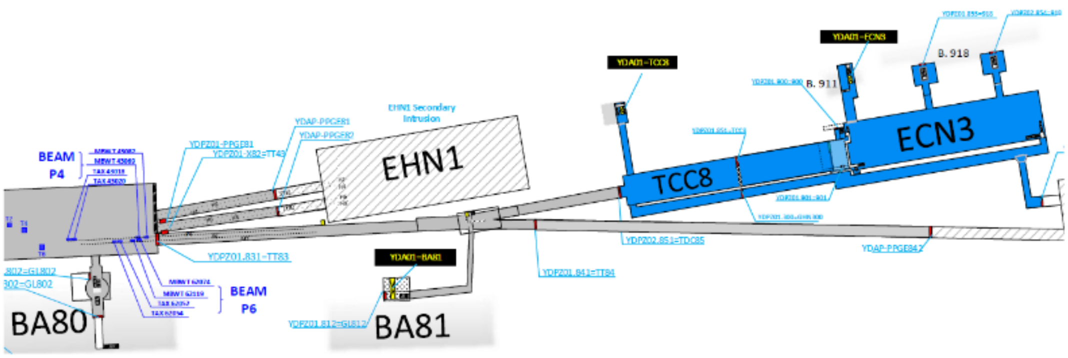

Figure 1.22: The SPS beamline to the TCC8 target gallery and the ECN3 experimental cavern (highlighted in blue) [58].

The four-collimator neutral beamline layout developed for ECN3, shown in fig. 1.23, is optimized in order to minimize the beam halo and the muon background. The final stage of collimation is the Active Final Collimator (AFC) incorporated into the Upstream Veto (UV) at z = 120 m from the target: according to the simulation, for an intensity of 2×10^{13} protons per pulse and an effective spill length of 3 s, the secondary beam will be composed by 140 MHz of K_Ls and 440 MHz of neutrons [59].

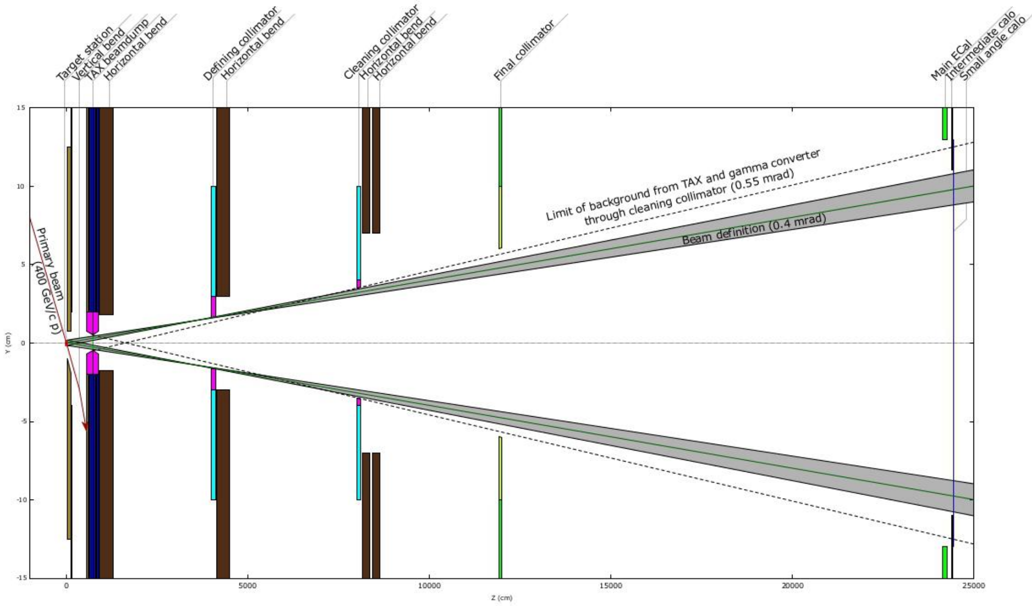

Figure 1.23: The K_LEVER four collimation stages (corresponding to TAX-dump, definig, cleaning and final beam collimators) as modeled in the FLUKA simulation [60].

1.2.3 THE TAX PHOTON CONVERTER

A central role in the apparatus for the attenuation of the large photon background in the secondary beam is performed by the TAX photon converter, a high Z-component placed in the center of the TAX collimator. Its primary task is to reduce the flux of photons in the neutral beam, while maintaining at the same time an adequate transparency to the hadronic component, in order to minimize the hadrons multiple scattering. An intriguing possibility for the construction of an instrument that is sensitive to photons and blind to hadrons is to use a compact crystalline tungsten tile as a converter: the crystal structure combined with the high atomic number induces coherent interactions of high energy photons with the crystal lattice, increasing the rate of $\gamma \rightarrow e^+e^-$ pair conversions with respect to the one obtained with amorphous materials (fig. 1.24). The effect depends on the photon energy and on the incident angle, and will be described in more detail in Chap. 2 [61]: in the case of K_LEVER, it is expected that the $\frac{X_0}{\lambda_{int}}$

ratio (where X_0 is the radiation length[11] and λ_{int} the hadronic interaction length[12]) will decrease of a factor 2-3.

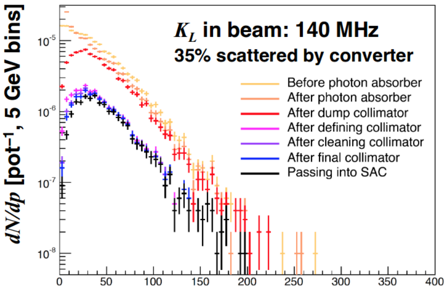

(a) K_L simulation

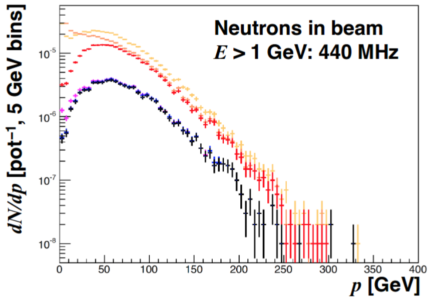

(b) n simulation

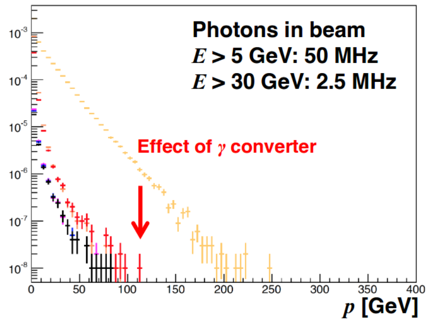

(c) γ simulation

Figure 1.24: The FLUKA K_L beam and neutral background simulation, showing (a) the K_L beam and (b) the neutrons and (b) the photons background contribution along the beamline, where the red arrow highlights the effect due to the presence of the TAX crystalline converter [7].

1.2.4 THE MAIN ELECTROMAGNETIC CALORIMETER

Two different scenarios are under study for the design of the electromagnetic calorimeter used for the reconstruction of the π^0 decays and the signal events. The first one foresees to use the liquid krypton calorimeter of the NA62 experiment [62] (fig. 1.25). The major problem is the temporal resolution with which the event is measured (500 ps) which would be completely dominated by the accidental vetoes rate from beam photons interacting in the SAC, of the order of 100 MHz. The detector time resolution might be improved via a huge readout upgrade.

11 The X_0 electromagnetic radiation length of a medium is the length equal to the mean distance over which an impinging high-energy electron loses all but 1/e of its energy via bremsstrahlung; it is usually measured in g·cm^{-2}.

12 The λ_{int} hadronic interaction length is the distance that a hadron can travel before a nuclear interaction occurs.

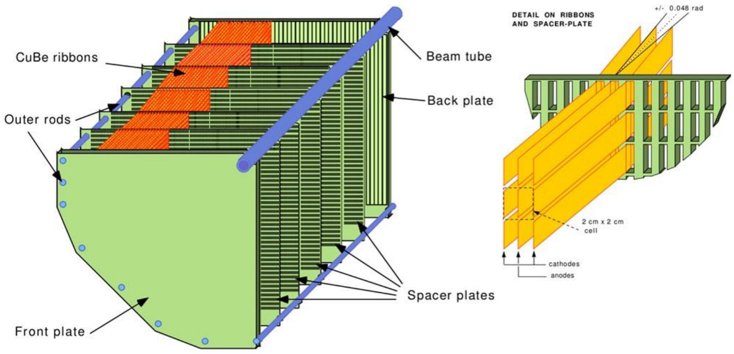

Figure 1.25: The NA62 LKr-calorimeter structure; the detector could be a possible candidate for the main electromagnetic calorimeter of K$_L$EVER [63].

The second option is to use a shashlik electromagnetic calorimeter with 1 mm diameter WaveLength Shifter (WLS) fibers read out by Silicon PhotoMultipliers (SiPM), developed according to the structure of the $\bar{P}$ANDA [64] Forward Spectrometer calorimeter. The $\bar{P}$ANDA FS calorimeter is composed by modules of 110×110 mm^2, in which 0.275 mm thick lead absorber layers are alternated with 1.5 mm thick scintillator tiles. A stochastic energy resolution of $\sigma_E/E = 4\%/\sqrt{E}$ and a time resolution of $\sigma_t = 72$ ps/E have been obtained in preliminary tests [65]. A slightly different version could be used in the K$_L$EVER experiment adding inside the structure of the detectors 10 mm thick scintillator "spy tiles", optically isolated from the shashlik structure and read out by dedicated WLS fibers (fig. 1.26). The spy tiles would be located at key points in the longitudinal shower development, providing a longitudinal sampling of the shower that would result in additional information for the γ/n separation.

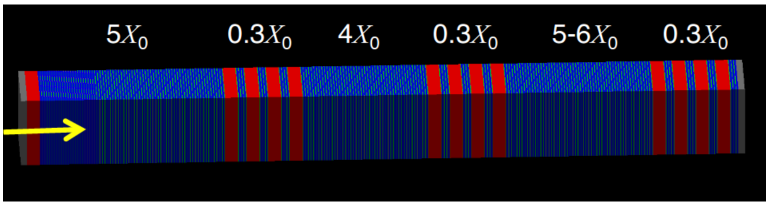

Figure 1.26: The prototype model of the $\bar{P}$ANDA shashlik calorimeter with integrated the K$_L$EVER spy tiles [7].

1.2.5 THE UPSTREAM VETO

The main task of the Upstream Veto is to reject the K$_L \to \pi^0\pi^0$ decays in the 40 m upstream of the fiducial volume, where there are no large-angle photon vetoes. It is mandatory to obtain information on these background decays in this section of the experiment, since it is possible for K$_L \to \pi^0\pi^0$ decays to result in two photons in the fiducial area of the MEC. The upstream veto is designed as a shashlik calorimeter with the same basic structure of the main electromagnetic calorimeter, without the spy tiles.

1.2.6 THE ACTIVE FINAL COLLIMATOR

The Active Final Collimator is inserted into a 100 mm hole in the center of the UV: it is a LYSO [66] multi-collar counter with angled inner surfaces to provide the last stage of beam collimation, while vetoing photons from the K_Ls that decay in transit through the collimator itself. It is formed by 100 LYSO crystals with a trapezoidal cross section, with bases of 15 and 25 mm and a height of 40 mm; each collar is made of 24 crystals, forming a detector with an inner radius of 60 mm, read out on the back side with two Avalanche PhotoDiodes (APDs). Fig. 1.27 shows the UV and AFC structures, as foreseen by the feasibility study.

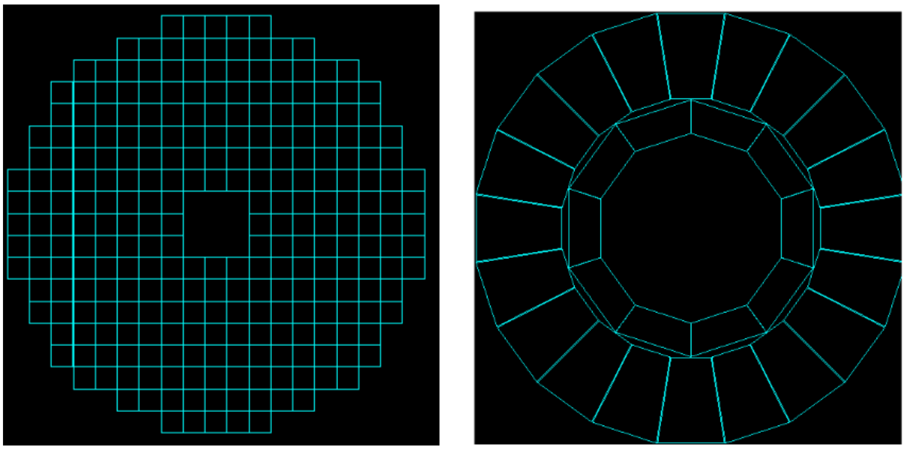

(a) The UV layout **(b)** The AFC layout

Figure 1.27: A schematic layout of (a) the UV detector and (b) the AFC LYSO collar [7].

1.2.7 THE LARGE ANGLE PHOTON VETOES

25 photon veto stations are placed along the length of the vacuum structure. The detectors are lead/scintillating sampling calorimeters with wavelength-shifting fiber readout, oriented in vertical annular rings around the beam, developed according to the CKM Vacuum Veto System (VVS) design [67]. Because of the boost from the high-energy beam, it is enough for the Large-Angle photon Vetoes (LAVs) to cover a range of polar angles up to 100 mrad. The veto system is organized in stations, at a distance of 4-5 m one from the other with increasing sensitive radius (from 0.85 to 1.5 m). Each

detector needs a good detection efficiency at low energy (1-$\epsilon \approx 0.5\%$ at 20 MeV, where ϵ is the inefficiency parameter[13]), in order to reject low-energy photon events.

1.2.8 THE CHARGED PARTICLE VETO

A special attention must be devoted to the rejection of events involving charged particles in the final states, in particular related to the dominant process of the K_{e3} decay (a benchmark channel because of its large branching ratio [68]), whose electrons and positrons can easily be mistaken as photons in the electromagnetic calorimeter; another key point is the distinction of the processes containing $\mu^{\pm}$ and $\pi^{\pm}$ in the final states. The latter problem can be solved by using the NA62 hadronic calorimeter and its muon vetoes; for the first one, simulations indicate that the needed rejection can be achieved with two planes of Charged Particle Veto, each one providing 99.5% of detection efficiency. The two CPV layers will be positioned ≈3 m upstream of the electromagnetic calorimeter and they will be composed by 5 mm thick (1.2 X_0) square scintillator tiles, supported on carbon fiber membrane, in a design carefully optimized to avoid insensitive gaps (thus cracks staggering in between the two planes is needed).

1.2.9 THE PRESHOWER DETECTOR

The PreShower Detector will be composed by a 0.5 X_0 converter and two tracking planes with a spatial resolution of 100 μm, placed 50 cm apart. Its primary function is to measure the directions of the photons incident on the electromagnetic calorimeter: the presence of a preshower detector is mandatory in order to reconstruct the z-position of the single π^0 vertex, by projecting the photon trajectories to the beamline. As the π^0 invariant mass is an independent quantity, $K_L \rightarrow \pi^0\pi^0$ decays with mispaired photons can be efficiently rejected. The tracking detectors must cover a surface of about 5 m^2 and, at the same time, they must minimize the material along the decay line: the MicroPattern Gas Detector (MPGD) technology could be the solution to the problem.

1.2.10 THE SMALL-ANGLE CALORIMETER

The Small-Angle Calorimeter (SAC) is another crucial point of the experimental setup: it perpendicularly intercepts the neutral beam and because of the high rates of neutrons and photons in the beam, its design is one of the most challenging aspects of the experiment. The fundamental feature of this instrument is its detection efficiency: the detector can be blind to photons with E<5 GeV, but needs a very high detection efficiency for photons with E>30 GeV in order to reject high-energy γs from the $K_L \rightarrow \pi^0\pi^0$ decay escaping through the beamline. In addition, due to the 430 MHz neutron background, the SAC must have a good longitudinal and transverse segmentation,

13 The ϵ inefficiency fraction is defined as the ratio between the number of the events contributing to the detector inefficiency and the total number of the events.

in order to provide a good γ/n signal discrimination. An alternative, and at the same time intriguing solution, that can solve both the problems, is given by high-Z oriented crystals, using their ability to increase the X_0/λ_{int} ratio due to the coherent effects induced by the crystalline structure with respect to the ones obtained with amorphous materials (Chap. 2 [61]); a detector that is sensitive to photons and blind to hadrons may be developed as a compact Si-W sampling calorimeter with crystalline tungsten tiles as the absorber material, in a way similar to the one used in the TAX photon converter. The proof-of-concept simulation for the baseline solution is a 14 layer, 1 mm crystal W-Si pad calorimeter, oriented with respect to the incoming photon beam at an angle $\theta_{inc} = 2$ mrad, in order to obtain a $14X_0$ detector for E$\gamma = 30$ GeV, but only $4X_0$ for E$\gamma = 5$ GeV (according to the state-of-art of the theoretical predictions of the crystals coherent effects). In order to keep the false veto rate from accidental coincidence of beam neutrons to an acceptable level ($<$ 10 MHz), and assuming that about 25% of the beam neutrons generate signals above threshold in the SAC, the topological information from the SAC must allow residual neutron interactions to be identified with 90% efficiency, while maintaining 99% detection efficiency for photons with 5 GeV $<$ E$\gamma <$ 30 GeV. A further challenging problem is the acquisition rate that this detector must sustain: an innovative readout solution to handle rates of 100 MHz (due to the detector position with respect to the beamline) is currently under development.

This thesis work has been performed in the K_LEVER experiment R&D framework, and is devoted to the analysis of the results of the collaboration beamtest hold in August 2018 at the CERN-SPS North Area. The beamtest goal was the characterization of straight tungsten crystals as means to increase the electromagnetic radiation produced by a high energy photon beam impinging on a crystal in channeling condition, in order to verify the design solution for the SAC calorimeter and the TAX photon converter in the K_LEVER final layout.

2

A SHORT GUIDE TO CRYSTALS

The word *crystal* is synonymous with an ordered periodic structure: since the early XVII Century [1] crystals have been the subject of many researches and studies ([71]-[72]), given their particular features. Any particle crossing an amorphous medium or a misaligned crystal loses energy mainly via ionization, and shifts its trajectory in a totally random way due to the Coulomb multiple scattering caused by the totally unrelated collisions with the lattice atoms. On the contrary, if the target atoms are arranged according to a precise scheme, the distribution of the impact parameters and the physical processes yields are found to be strongly dependent on the relative orientation between the particle and the target: the random collisions turn into a coherent interaction of the particle with the whole atomic structure.

The interatomic potential generated by the individual lattice atoms in fact can be approximated with a continuous potential due to the crystal planes and axes, which are thus able to confine the motion of a charged particle within them and to induce coherent radiation effects. This effect is known as channeling. In 1912 Stark [73] had the first idea that the atomic ordered structure of a crystal could be important for the process of interaction of charged particles with matter; fifty years later, crystal channeling was proposed by Lindhard [74] in 1964. From that moment on, crystals have found many different uses in accelerators physics [75] (as tools for collimation, extraction, beam steering and beam cleaning), but they are also leading to new and exciting results in high energy calorimetry [76].

This chapter wants to be a short guide to crystals, combining the theoretical view with a much more practical approach. Sec. 2.1 describes the crystalline lattice and the particle interactions in a crystalline medium, focusing on the channeling condition in Sec. 2.1.1, while Sec. 2.2 provides a detailed view of the coherent effects that channeling may induce.

1 The very first studies on crystals were performed by Kepler (1571-1630) regarding the shape of snowflakes [69]; the first work that developed a classification system for the crystalline structures and the first crystallography formulations was written by Hauly (1743-1822) [70].

2.1 CRYSTALS AND CHANNELING: A BASIC IDEA

The simplest (and in some way, the most effective) definition of a crystalline structure is an ordered ensemble of a set of elementary components, such as atoms, ions or molecules, located in a lattice. According to the orientation of the material with respect to a reference system, an external observer who looks at the crystalline structure can notice how the atoms of the crystal itself may be arranged in different ways (fig. 2.1): in a unordered structure (amorphous material), in parallel planes or strings.

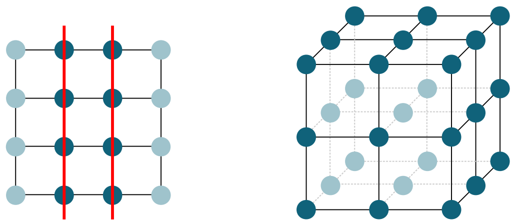

Figure 2.1: Depending on the orientation, the crystal lattice appears as (left) arranged in planes, (center) as an amorphous material and (right) as axes parallel with each other, perpendicular to the observer.

The schematic structure of a crystalline lattice can be described by the appropriate Miller indices, which provide a complete notation in the classification of the planes and the axes directions inside a crystal [77]. Fig. 2.2 shows some of the more frequent crystalline planes with their proper Miller indices in a crystal with a simple cubic structure, such as Silicon (fcc, face-centered cubic system) or Tungsten (bcc, body-centered cubic system).

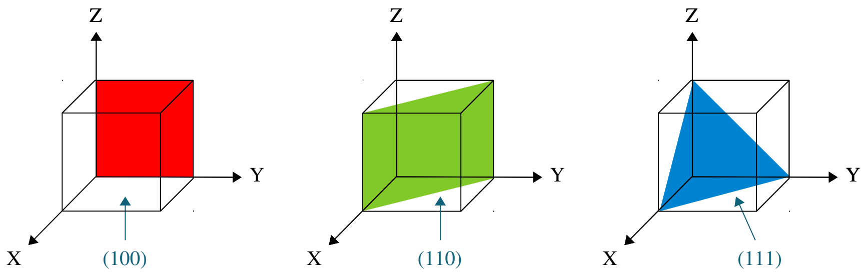

Figure 2.2: Different crystalline planes in a simple cubic face lattice, along with their proper Miller indices.

A great variety of physical phenomena can occur when an energetic particle impinges upon a solid target: these processes have different cross sections depending on the impact parameter b involved in the collisions with the atoms of the target medium. The channeling effect in a crystalline structure can be described as follows:

- if the charged particle impinges on the crystal in a randomic way, it interacts with the crystal as an amorphous medium, and the collisions inside the crystalline structure will be completely unrelated one to each other (fig. 2.3-a);
- on the other hand, the electrostatic potential can confine the particle motion between two atomic planes if the particle motion direction lies close to a major crystal direction. The particle will suffer small angle scatterings, oscillating in the open channel generated by the continuous potential approximation. Such a motion is referred to as planar channeling (fig. 2.3-b);
- the same phenomena occur when the direction of the impinging particle lies close to a major crystalline high symmetry axis; the particle undergoes a correlated series of gentle small angle collisions moving along the string direction, in what is known as axial channeling (fig. 2.3-c).

The channeled trajectories are thus those that lie close to a major crystal direction and which (in case of positive particles) originate in the open spaces between atomic rows or planes.

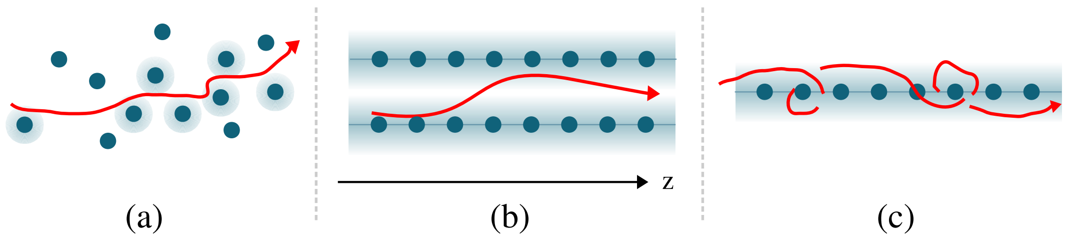

Figure 2.3: A schematic view of (a) the amorphous interaction, (b) the planar and (c) the axial channeling condition in a medium; the red lines are the trajectories of the incident particles.

2.1.1 THE CONTINUUM DESCRIPTION

The interaction of a charged particle with a crystal can be described in an analytical way starting from the study of a moving particle inside an ordered structure of many charged scattering points (fig. 2.4). The potential describing the collision between a charged particle and an isolated atom can generally be expected to be a rather complicated function of many parameters (such as the nuclear separation distance d, the relative velocity v, the masses and the atomic numbers of the collision partners, and the impact parameter b). In order to reduce the problem complexity, several approximations can be made [78]:

- the scattering can be described with a two-body potential function;
- the charged particles are so closely aligned with the crystalline axis that their motion is completely governed by many correlated collisions with the lattice atoms;
- the inelastic electron scattering can be neglected.

The constraint on the particle motion plays a fundamental role: considering a particle that moves inside a crystal almost aligned with a privileged direction of the crystal itself (as shown in fig. 2.5), the angle θ between the total momentum p of the particle and the atoms direction has to be small ($\theta \ll 1$). Considering now the components $p_\perp$ and $p_\parallel$ (respectively the transverse momentum and the momentum parallel to the direction of the atomic plane or string), since $\theta = p_\perp / p_\parallel$, then $p_\perp / p_\parallel \ll 1$ [79]. In terms of the particle motion, the transversal momentum has to be small compared to the longitudinal one, so that the particle travels a long distance and interacts with many lattice atoms in the longitudinal direction while it moves slightly in the transverse direction.

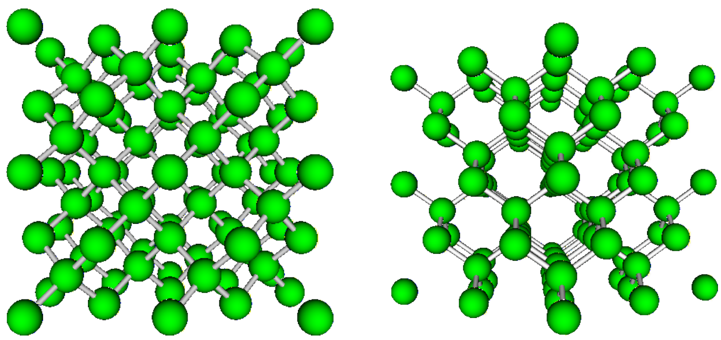

(a) Planar structure **(b)** Axial structure

Figure 2.4: A crystalline silicon lattice shown as an ordered sequence of scattering points organized as (a) planes or (b) rows.

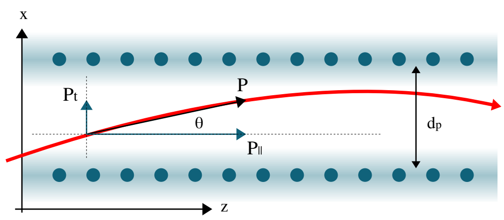

Figure 2.5: A particle impinging on a crystalline lattice with an angle $\theta = p_\perp / p_\parallel$ with respect to the planes directions will be channeled; d_p is the interplanar distance, while the red line shows the particle path.

Due to the periodic structure, the particle path is determined by the average effect of many atoms and the collisions are correlated, as if the crystalline plane or axis were physical objects formed by a continuous charge distribution. Each atomic row or plane defines a continuous, electrostatic potential that is obtained by smearing the atomic charges uniformly along the z direction of the string itself; thus the name continuum approximation. These distributions inside the crystal lattice form a series of planar (or axial) potential-wells which are able to confine the particle motion in a channeled condition [80]. A comprehensive treatment of the continuum model was given by Lindhard [74]; this model can describe the average properties of a given trajectory inside a crystalline lattice.

PLANAR MOTION IN THE CONTINUUM MODEL

Considering a particle travelling inside a crystal aligned with one of its planes (fig. 2.6), if $V(r)$ is the electrostatic potential between the particle and a single atom, the continuous potential at a distance x from a string of atomic nuclei can be written as the average of the inter-atomic potential $V(r) = V(\sqrt{x^2+y^2+z^2})$:

$$U_{pl}(x) = Nd_p \cdot \int_{-\infty}^{\infty} dydz \cdot V(x,y,z) \tag{2.1}$$

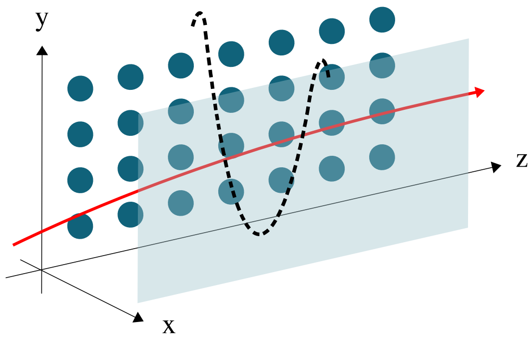

Figure 2.6: A schematic view of the planar channeling.

where d_p is the interplanar atomic spacing, and N is the number of atoms. The potential $V(x,y,z)$ that describes the elastic interaction between the particle and the atom at a distance r is the Coulomb repulsion of the atomic nucleus modified by an appropriate screening function describing the electronic cloud contribution. Lindhard proposed the Thomas-Fermi model to approximate the screened Coulomb potential [74]:

$$V(r) = \frac{Z_p Z_n e^2}{r} \cdot \Phi\left(\frac{r}{a_{TF}}\right) \tag{2.2}$$

where $Z_p e$ and $Z_n e$ denote respectively the projectile and the nuclear charge (Z_i are the atomic number of the particle and the atom respectively, and e is the electronic charge), while r is the distance between the particle and the atom. $\Phi\left(\frac{r}{a_{TF}}\right)$ is the screening function which takes into account the charge distribution of the target nuclei. a_{TF} is the Thomas-Fermi screening radius, given by:

$$a_{TF} = 0.89 \cdot a_0 \cdot \sqrt{(Z_p^{2/3} + Z_r^{2/3})} \tag{2.3}$$

where a_0 is the Bohr radius for hydrogen [81]. A widely used analytical form for ϕ is given by Molière [82]:

$$\Phi\left(\frac{r}{a_{TF}}\right) = \left(0.1e^{-\frac{6r}{a_{TF}}} + 0.35e^{-\frac{0.3r}{a_{TF}}} + 0.55e^{-\frac{1.2r}{a_{TF}}}\right) \tag{2.4}$$

Lindhard proposed the alternative form [74]:

$$\Phi\left(\frac{r}{a_{TF}}\right) = 1 - \left(1 + \frac{3a_{TF}^2}{r^2}\right)^{-\frac{1}{2}} \tag{2.5}$$

Substituting eq. 2.2 in eq. 2.1 gives the standard Lindhard continuous potential generated by a single crystal plane:

$$U_{pl}(x) = 2\pi \cdot Z_p Z_n e^2 \cdot N d_p \left(\sqrt{x^2 + 3a_{TF}^2} - x\right) \tag{2.6}$$

x is the distance of the particle trajectory from the plane: $x = 0$ is the plane position and it corresponds to the maximum potential value considering positive particles. Note how the expression of the potential depends on the features of the crystal and on the interatomic distance d_p of the atomic planes. Silicon crystals are the most used for channeling in high energy experiments, due to the high technology standard reached in terms of quality of the crystals themselves: fig. 2.7 shows the interplanar (110) and (111) planes potentials in a crystalline Si-structure.

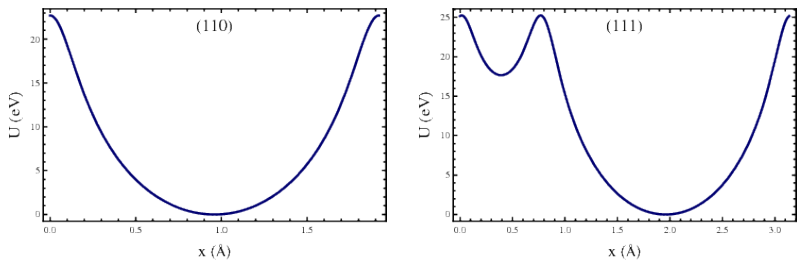

(a) (110) plane **(b)** (111) plane

Figure 2.7: The interplanar Molière potential for (a) the (110) plane and (b) (111) plane for a silicon crystal [83].

AXIAL MOTION IN THE CONTINUUM MODEL

The axial channeling potential can be easily computed by slightly modifying the expressions of the planar case: considering a particle motion such as the one described in fig. 2.8, the elastic interaction between the ion and the atom at a distance r is described by the interaction potential $V(r)$ (using the Lindhard expression):

$$V(r) = \frac{Z_p Z_n e^2}{r} \cdot \left(1 - \frac{r}{(r^2 + (Ca_{TF})^2)^{\frac{1}{2}}}\right) \tag{2.7}$$

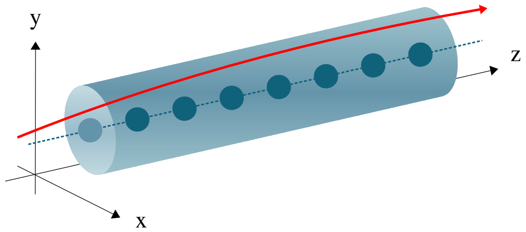

Figure 2.8: A schematic view of the axial channeling.

The continuous potential at a distance $r_\perp$ from a string of atomic nuclei is written as the average of the inter-atomic potential $V(r)$:

$$U_a(r_\perp) = \frac{1}{d} \cdot \int_{-\infty}^{\infty} V(\sqrt{z^2 + r_\perp^2})dz \tag{2.8}$$

where d is the interatomic spacing along the atomic row, z is the distance of the particle from the nucleus along the row in the channeling direction so that

$$r = \sqrt{z^2 + r_\perp^2} \tag{2.9}$$

is the distance between the charged particle and the nucleus. By combining eq. 2.7 and eq. 2.8, one obtains the expression of the standard Lindhard potential in the axial case at a distance $r_\perp$ from the string (fig. 2.9):

$$U_a(r_\perp) = \frac{Z_p Z_n e^2}{d} \cdot \log\left(1 + \frac{(Ca_{TF})^2}{r_\perp^2}\right) \tag{2.10}$$

2.1.2 THE CRITICAL ANGLE

A charged particle channeled in the potential well (by two atomic planes or by an atomic string) must undergo particular conditions to maintain the channeling. The total energy E of the system is composed by two contributions: one due to the particle motion, and the other to the ion-lattice interaction $U(x)$. In the framework of the continuum approximation, the transversal momentum must be much smaller than the parallel one, and thus the total energy of the system can be approximated as [85]:

$$E = \sqrt{p_\perp^2 + p_\parallel^2 + m^2c^2} + U(x) \approx \frac{p_\perp^2 c^2}{2E_\parallel} + E_\parallel + U(x) \tag{2.11}$$

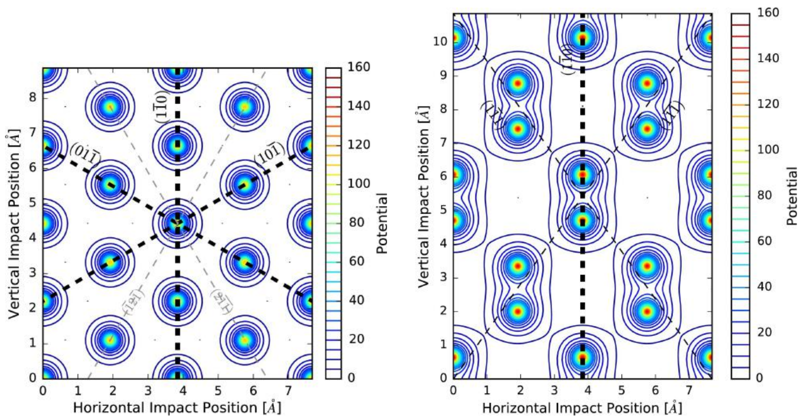

(a) (111) Si-axis **(b)** (110) Si-axis

Figure 2.9: (a) The average potential along the (111) axis of a silicon crystal (the directions of the (110) and (211) planes are shown) and (b) the average potential along the (110) axis of a silicon crystal (the directions of the (111) planes are shown) [84].

where $E_{\parallel} = \sqrt{p_{\parallel}^2 + m^2c^2}$; $p_{\parallel}$ is not affected by the potential: it is a conserved quantity, and so are $E_{\parallel}$ and $\frac{p_{\perp}^2 c^2}{2E_{\parallel}} + U(x)$ due to the energy conservation law. $E_{\perp}$ can be expressed in terms of the misalignment angle θ between the particle trajectory and the crystal planes:

$$E_{\perp} = \frac{p_{\parallel}^2 c^2}{2E_{\parallel}}\theta^2 + U(x) \approx \frac{p^2c^2}{2E}\theta^2 + U(x) \tag{2.12}$$

Given that $p_{\perp}/p_{\parallel} \ll 1$, $p_{\parallel}$ can be approximated with the total momentum p and $E_{\parallel}$ with the total energy E, thus $E_{\perp}$ is a conserved quantity. Each particle entering the crystal medium has a transversal energy value as a function of the alignment angle θ with respect to the crystalline plane and of its relative position x in the channel (fig. 2.10).

If $E_{\perp}$ is somewhat below the potential maximum $U(d_p/2)$, the charged particle is kept away from the region near to the string of high atomic density. Considering the thermal displacements of the target nuclei which can induce a shift of the nuclear target average position $x_0 = d_p/2$, the slightly lower critical value $U(x_c) = U(x_0 - \rho)$ could be chosen, where ρ is the mean amplitude of the atomic thermal vibration of the lattice. The channeling condition in terms of θ and x is given by [85]:

$$\frac{p^2c^2}{2E}\theta^2 + U(x) \leq U(x_c) \tag{2.13}$$

As $pc^2 = vE$, substituting this expression in eq. 2.13, $E_{\perp}$ can be written as:

$$E_{\perp} = \frac{pv}{2}\theta^2 + U(x) \tag{2.14}$$

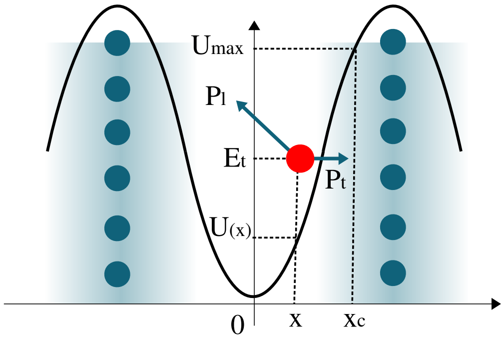

Figure 2.10: Schematic description of the interplanar potential; the red dot is a particle trapped in channeling condition with transversal energy E_t lower than $U(x_c)$.

The critical channeling angle can be obtained by expressing the maximum and minimum values in terms of the energy $E_\perp = U_{max}$ and the position with respect to the atomic plane $x = 0$:

$$\theta_c = \sqrt{\frac{2U(max)}{pv}} = \sqrt{\frac{4Z_pZ_ne^2Nd_pCa}{pv}} \tag{2.15}$$

For a silicon crystal $U_{max} \approx 20$ eV, θ_c is 280 μrad at 500 MeV, 9.42 μrad at 450 GeV and 2.39 μrad at 7 TeV [85]. The critical angle decreases as the square root of the energy, while the multiple scattering as the energy of the incoming particles; therefore, the effects due to multiple scattering which reduce the channeling efficiency become less important at high energy. The critical angle for axial effects can be obtained in the same way:

$$\theta_c = \sqrt{\frac{4Z_pZ_ne^2}{pvd}} \tag{2.16}$$

The θ_c angle can be expressed as $\frac{dx}{dz}$ where dx and dz are the infinitesimal increases in the transversal and longitudinal spatial directions; substituting the latter relation in eq. 2.15, the following differential equation describes the particle motion in the channel:

$$E_\perp = \frac{pv}{2} \cdot \left(\frac{dx}{dz}\right)^2 + U(x) \tag{2.17}$$

Differentiating with respect to z, one obtains:

$$pv \cdot \left(\frac{d^2x}{dz^2}\right) + U'(x) = 0 \tag{2.18}$$

and taking into account the harmonic potential approximation $U(x) = U_0 \cdot (x\frac{2}{d_p})^2$:

$$pv \cdot \left(\frac{d^2x}{dz^2}\right) + U_0 \cdot \frac{8x}{d_p^2} = 0 \tag{2.19}$$

The solution of eq. 2.19 gives the particle trajectory in space, which corresponds to a sinusoidal oscillation:

$$x = \frac{d_p}{2} \cdot \frac{E_\perp}{U_0} \cdot \sin(\frac{2\pi z}{\lambda} + \phi) \tag{2.20}$$

The length of the oscillation period is:

$$\lambda = \pi d_p \sqrt{\frac{pv}{2U_0}} \tag{2.21}$$

For example, a 400 GeV/c proton in silicon has a wavelength $\lambda \approx$25.5 μm [85].

2.1.3 CHANNELING OF NEGATIVE AND POSITIVE PARTICLES

The form of the continuous potential changes dramatically if the incident particle has a positive or a negative charge, and so do the channeling conditions. The two particle families are subjected to potentials equal in form, but opposite in sign: a negative particle (such as an electron) will experience a potential with a minimum centered along the crystal axis or the atomic plane; on the contrary, a positively charged particle will feel a potential centered at the midpoint with respect to two planes or two adjacent axes (fig. 2.11). Negative channeled particles are thus focused on the nuclei and have an increased probability for hard collisions with atoms, while positive particles are steered away, so that the channeling states are much more stable.

The difference in channeling motion for particles of opposite charge is more dramatic in the axial case: positive particles move freely from channel to channel, whereas negative ones are bound to one single string (or to a pair of strings) [86].

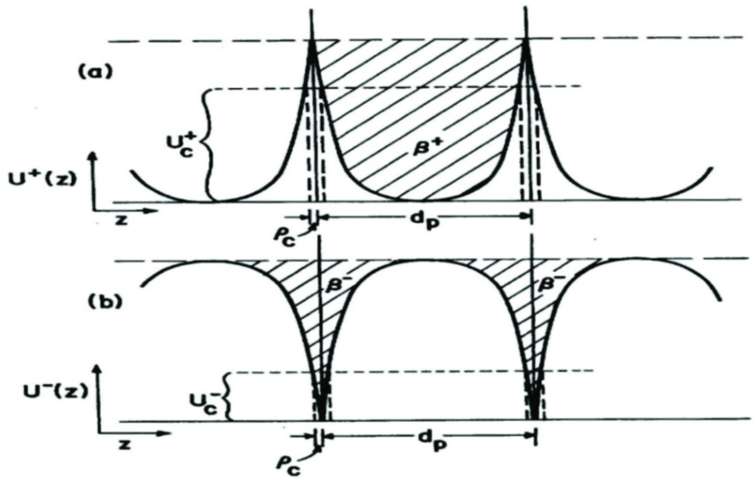

Figure 2.11: The channeling potential for positrons (up) and for electrons (down); the scattering nuclei in the first case correspond to the maximum potential value, while in the other they are positioned at the minimum [87].

2.2 STRONG FIELD EFFECTS IN CRYSTALS

Energetic heavy charged particles in an amorphous substance (or a misaligned crystal) lose energy mainly in inelastic collisions with atomic electrons, *i.e.* through ionization energy losses. The stopping power dE/dx, x being the depth penetration, is described by the Bethe-Bloch formula [88] and the energy loss follows the Landau distribution [89]. On the other hand, because of their small mass, electrons and positrons not only lose energy in collisions with atoms, but also in the emission of electromagnetic radiation (also known as bremsstrahlung) arising from scattering in the electric field of a nucleus. At energies larger than the E_c critical energy

$$E_c \approx \frac{610 \text{ MeV}}{Z + 1.24} \tag{2.22}$$

the bremsstrahlung process dominates the energy losses of electrons and positrons [90]. The situation deeply changes considering an ordered crystalline structure and the continuum approximation: when relativistic particles interact with aligned crystals, most of the physical processes acquire new features compared to amorphous targets, caused by the periodic arrangement of crystal atoms. One of the results of these features is the occurrence of coherent effects in the interaction of high-energy photons and charged particles with crystal targets, which is caused by the quantization of the momentum transferred to the crystal. Thus a particle impinging in a crystal with an angle θ similar to the critical angle θ_c can feel strong field effects and considerably change its interaction model in comparison with an amorphous medium [91]. Depending on the angle, on the trajectory followed within the lattice and on the outgoing spectrum, the process is called channeling radiation or coherent bremsstrahlung:

- in coherent bremsstrahlung, particles are not channeled but they cross the crystalline planes at a small angle. The particle scattering by atoms in a plane is still correlated, and the characteristic oscillation period (corresponding to the periodic crossing of the atomic planes) is $T = \theta_0 d$, where θ_0 is the particle impinging angle and d is the interplanar distance [92];
- in channeling radiation, the particle velocity is nearly parallel to either a crystal axis or a plane. The particle undergoes correlated soft collisions with the atoms so that it is forced in an oscillatory motion within the potential well, whose amplitude depends on the initial transversal energy value. The oscillatory motion of the channeled electrons and positrons leads to a coherent electromagnetic emission due to the constructive interference of the electromagnetic radiation emitted in the correlated deflections [93].

2.2.1 COHERENT BREMSSTRAHLUNG

The coherent bremsstrahlung (fig. 2.12) is associated with a fast-charged particle striking a crystalline medium at a small angle with respect to a crystalline plane [94].

In the bremsstrahlung process, a charged particle deflected by an electromagnetic field (typically an electron by an atomic nucleus) radiates, emitting a photon with an energy $\omega = \epsilon - \epsilon'$, being ϵ and ϵ' the initial and final energies of the impinging particle. In the case of coherent bremsstrahlung, the minimal value δ of the transferred momentum along the motion direction of the primary particle is:

$$\delta = \frac{\omega mc^2}{2\epsilon\epsilon'} mc \tag{2.23}$$

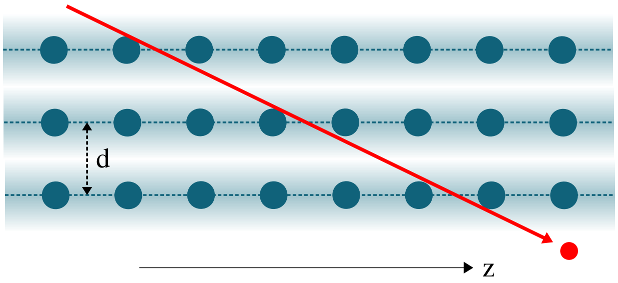

Figure 2.12: A schematic view of the coherent bremsstrahlung by a charged particle in a crystal lattice.

where m is the particle mass. From this expression, one can obtain the distance l_c which characterizes the formation length of the radiation process:

$$l_c = \frac{1}{\delta} = \frac{2\epsilon\epsilon'}{\omega mc^2}\frac{1}{mc} \approx \frac{c}{\omega(1 - v/c)} \tag{2.24}$$

The l_c parameter is called coherence length, and increases with the primary particle energy and with the decreasing of the energy of the emitted photon [95]. Consider now a charged particle crossing a crystal with a speed v and at an angle θ with respect to its planes, larger than the critical one θ_c and small enough for the continuum approximation to be valid: when the electron or the positron crosses the crystal planes periodically along the interatomic distance d, it has a fair chance to scatter coherently on many target atoms along its way. The coherence in scattering causes the radiation emission, that adds coherently at every plane crossing: such effect takes the name of coherent bremsstrahlung, to be distinguished from the ordinary bremsstrahlung in an amorphous medium. The condition of constructive interference between the bremsstrahlung radiation emitted between two scattering atomic points can be derived from fig. 2.13: if the θ impinging angle is small, then the radiation emitted at point 1 at the time t_0 and the radiation emitted at point 2 at the time $t_0 + d/(\theta v)$ sum constructively if [96]:

$$\frac{\omega d}{\theta}\left(\frac{1}{v} - \frac{1}{c}\right) = 2\pi n \tag{2.25}$$

Considering eq. 2.24, the constructive condition can be written as:

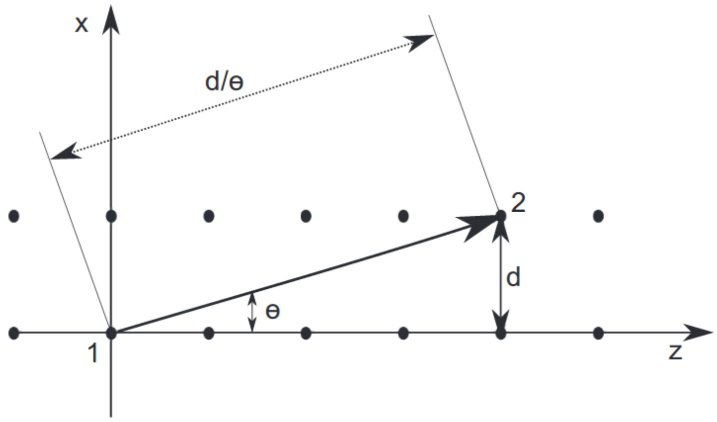

Figure 2.13: The classical interpretation of the interference processes in a crystal lattice [97].

$$\frac{\delta}{\theta} = n\frac{2\pi}{d} \tag{2.26}$$

The $2\pi/d$ factor has the dimensions of a reciprocal lattice vector[2]: in this way, the coherent bremsstrahlung process can be described as the enhancement of bremsstrahlung radiation when the momentum transferred by the positron (or the electron) to the crystal matches a reciprocal lattice vector (fig. 2.14). In a crystalline medium, due to the presence of the periodic ordered structure, the total emission in a single crystal may greatly exceed the bremsstrahlung emission in a similarly dense but amorphous medium composed of the same type of atoms (fig. 2.15). The peak emission energies depend on the crystal geometry and on the incident angle of the particle with respect to the planes; the most common use of the coherent bremsstrahlung radiation process is the production of high intensity, linearly polarized monochromatic gamma beams [99].

The same formalism of the coherent bremsstrahlung can be used to describe the e^+e^- pair production process of a high-energy γ-quantum moving in a periodic lattice [101].

2.2.2 CHANNELING RADIATION

When the particle velocity is nearly parallel to either a crystal axis or a plane ($\theta < \theta_c$), the straight trajectory approximation used in the coherent bremsstrahlung description is no longer valid, since the charged particle is forced in an oscillatory motion within the planar or axial potential well, in one of the accessible discrete energy levels generated by the crystal lattice electrostatic potential (fig. 2.16): it is trapped in the channeling condition. As coherent bremsstrahlung, the channeling motion produces coherence effects and the resulting radiation is called channeling radiation (fig. 2.17).

2 Given $\boldsymbol{a_1}$, $\boldsymbol{a_2}$ and $\boldsymbol{a_3}$ the primitive vectors of a cystal lattice, the reciprocal lattice vectors $\boldsymbol{b_1}$, $\boldsymbol{b_2}$ and $\boldsymbol{b_3}$ are the vectors orthogonal to two of the axis vectors of the crystal lattice [98].

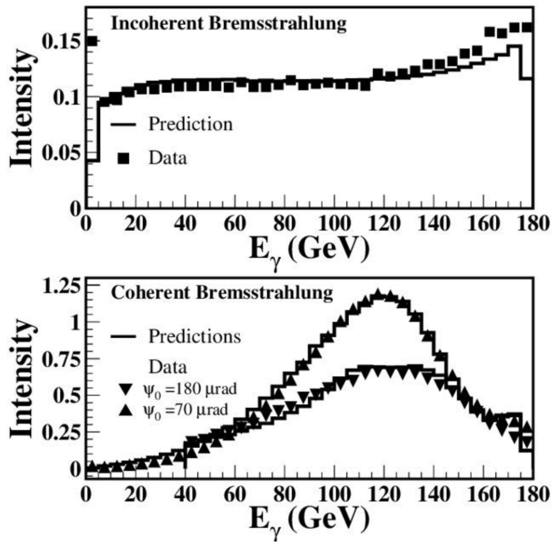

Figure 2.14: Total energy radiated for incoherent (top) and coherent (bottom) bremsstrahlung radiation in a 1.5 cm thick silicon crystal. The solid curves represent the Monte Carlo simulation results [100].

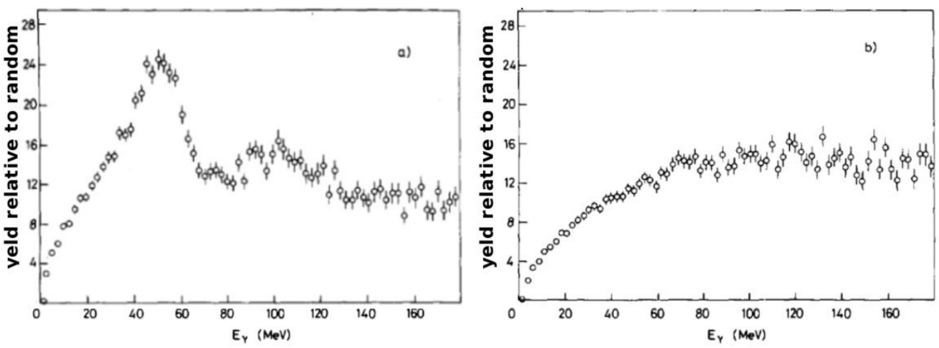

Figure 2.15: The photon energy spectra for a 10 GeV/c positron (left) and electron (right) beam impinging on a 0.1 mm silicon (110) crystal plane (normalized to the incoherent spectra intensity): in the positron spectrum the peak structure is relative to the first and second harmonics, while in the electron case the spectrum does not show any relevant structure over the general increase, due to the presence of the atomic nuclei in the minimum of the interatomic potential [85].

Consider the motion of a channeled positron in the harmonic interplanar potential $U(x) = (2x/d_p)^2$ (where d_p is the distance between two adjacent atomic planes); the angular frequency of the motion can be obtained from the oscillation wavelength expression of eq. 2.21 as [102]

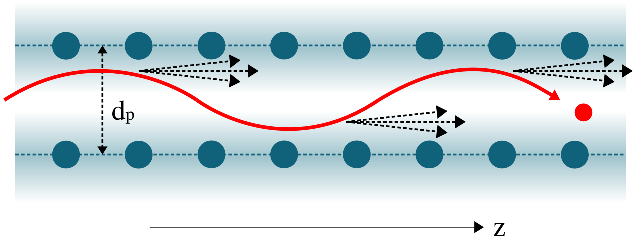

Figure 2.16: A schematic view of the channeling radiation by a charged particle in a crystal lattice.

$$\omega_0 = 2\pi\frac{\nu}{\lambda} = \frac{2}{d_p}\sqrt{\frac{2U_0}{m\gamma}} \tag{2.27}$$

where $\gamma = 1/\sqrt{1-v^2/c^2}$ is the Lorentz factor. In the rest frame, the particle oscillates at a frequency $\gamma\omega_0$ owing to the relativistic time dilatation, and it radiates at this frequency (and higher harmonics) with the angular distribution characteristic of a dipole. A Doppler transformation to the laboratory frame gives the photon frequency:

$$\omega_\gamma = n \cdot \frac{\gamma\omega_0}{\gamma(1-\beta\cos\theta)} = n \cdot \frac{\omega_0}{1-\beta\cos\theta} \tag{2.28}$$

In the ultrarelativistic limit one can consider $\gamma \gg 1$, so that the radiation frequency emitted in the $\theta = 0$ forward direction is given by:

$$\omega \approx 2\gamma^2\omega_0 = \frac{4}{d_p}\sqrt{\frac{2U_0}{m}}\gamma^{3/2} \tag{2.29}$$

To summarize, under certain conditions a high-energy charged particle that crosses a crystal with an appropriate angle is induced by in coherent bremsstrahlung or channeling radiation to emit high-energy photons in the direction of motion. Similarly, the coherent interaction of high-energy photons with a crystal lattice can enhance the probability of electron-positron pair production. The combination of these phenomena in the strong field regime is therefore characterized by the acceleration of an electromagnetic shower development, which results in a strong reduction of the shower length and thereby of the radiation length X_0 compared with the one of an amorphous material (fig. 2.18).
The radiation enhancement by coherent processes in a crystalline field was predicted in

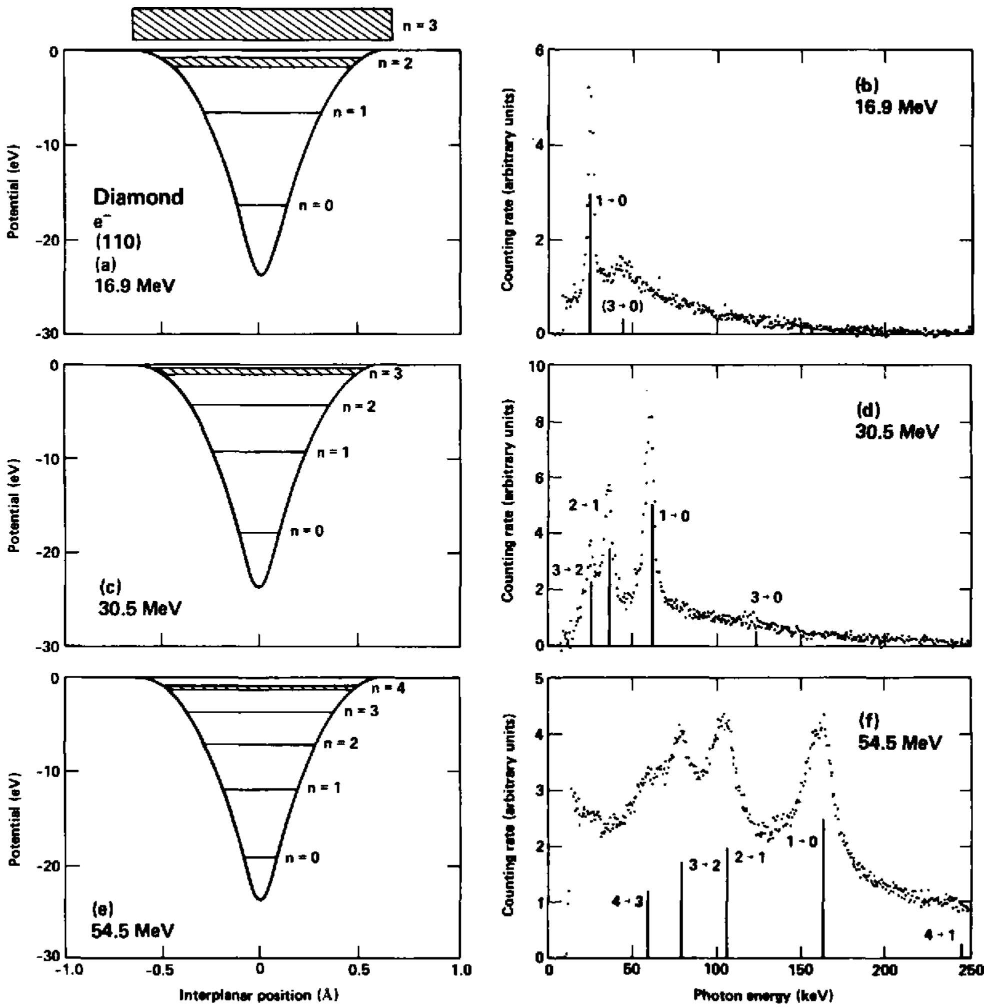

Figure 2.17: From top to bottom, the (110) potential and energy levels (left) with the corresponding channeling-radiation spectra (right) for 16.9 MeV, 30.5 MeV and 54.5 MeV electrons in a diamond lattice [103].

the late 80's [104]-[105] and observed at CERN and IHEP[3], employing single metallic crystals (as for example diamond, Si, Ge or W [107]).

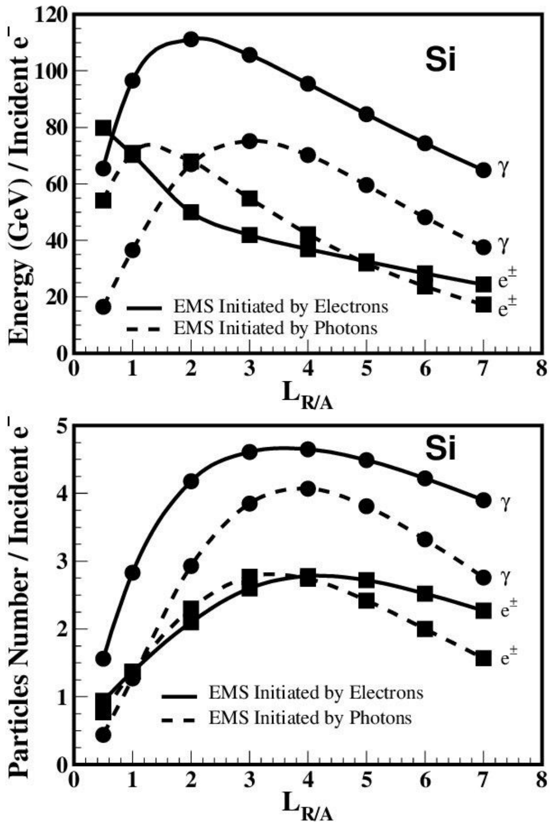

Figure 2.18: The energy (top) and the number of secondary particles (bottom) of the electromagnetic shower (EMS) generated by a particle impinging on an aligned silicon crystal, as a function of the sample thickness. $L_{R/A}$ is the effective radiation/the absorption length of the crystal for the shower started by an electron or a photon; dots refer to the γ component of the shower, while squares to the electron one [100].

3 Institute of High Energy Physics [106].

3

THE K_LEVER BEAMTEST AT THE CERN-SPS

The main goal of this master thesis is to understand the feasibility of using straight tungsten crystals in the experimental setup designed by the K_LEVER collaboration, exploiting the coherent effects of the interaction of a particle impinging on a crystalline structure (Chap. 2). In order to obtain an in-depth study of the main features and behavior of these crystals, a beamtest has been performed at the CERN laboratory. This chapter describes in the first part the goals, the experimental setup and the preliminary tests performed on the H2 line at the CERN SPS-North Area during the K_LEVER beamtest in August 2018: each section describes in a detailed way each component of the experimental layout, the alignment operations and the calibration procedure. The chapter also includes a short description of the Data AcQuisition (DAQ) system. The data collected by means of this setup needed a non trivial analysis to be exploited, because of the non perfect performance of some of the detectors during the data taking: the preliminary analysis procedure and the data correction are presented in Sec. 3.6.

3.1 TEST GOALS AND EXPERIMENTAL SETUP

The K_LEVER goals addressed at the test performed at CERN during summer 2018 were (mainly) two:

- the measurement of the effective increase in pair conversion of an incoming high energy photon beam using a high-Z metallic crystal due to the enhancement of coherent effects in the periodic crystal lattice, in order to be used as an efficient converter to eliminate photons from the neutral beam with minimal scattering of neutral kaons (as described in Sec. 1.2.10);
- the validation of the use of tungsten straight crystals as an efficient absorber for the sampling calorimeter to veto photons from K_L decays, while offering relative transparency to the intense flux of neutrons (Sec. 1.2.3).

These goals were transformed into three main results to be achieved during the beamtest:

- to observe the $\gamma \to e^+e^-$ pair-conversion enhancement by means of a commercially available tungsten crystal;

- to measure the pair-production probability and the spectrum of the transmitted γ-beam with a thick (10 mm) crystal;

- to measure the pair-conversion efficiency as a function of E_γ and θ in an energy range from 5 to 120 GeV, where θ is the angle of incidence of the photon with respect to the direction of the crystalline planes.

The test was performed in August 2018 on the H2 extracted beamline of the North Area at the CERN Prevessin site (figg. 3.1-3.2). The H2 facility is a high-energy secondary beamline: the beam that can be delivered to fixed target experiments consists of 400 GeV/c protons (primary SPS beam) or secondary mixed hadron beams within the 10 - 400 GeV/c range, in a variety of production angles; moreover, electron/positron beams with variable purity (10 - 99.5%) are also possible. The maximum Δp/p acceptance of the line is 2%; the beam composition, the rate, the momentum and the polarities of the transported particles in the line are a function of the configuration of the target station, the collimator settings and the materials present in the beamline. The sophisticated beamline equipment (a sequence of various magnets located downstream of the primary targets) allows the beam focusing towards the experimental area [108]. Lastly, by means of appropriate secondary targets, the SPS-H2 line can produce tagged photon beams of an energy up to 150 GeV. Fig. 3.3 presents a scheme of the North Area site; the experimental H2 area plan is shown in fig. 3.4.

This section will provide a complete description of the experimental layout.

3.1.1 A GENERAL OVERVIEW

Fig. 3.5 displays the 2018 beamtest layout: the particle beam crosses different detectors and components with different purposes and characteristics. From the upstream area to the end of the setup they are the following:

- two small plastic scintillator detectors (S1+S2), used for the basic trigger;

- two modules of double side *x*-*y* small area silicon microstrip detectors (T1 and T2) employed as a high performance tracking system for the upstream particle beam;

- a 1 mm thick copper target, converting the primary electron beam of the H2 line into a secondary beam of charged particles and high-energy bremsstrahlung photons;

- a large area single side *x*-*y* silicon strip chamber (C1);

- a dipole bending magnet (BM), deflecting on the horizontal plane the charged particles exiting from the target;

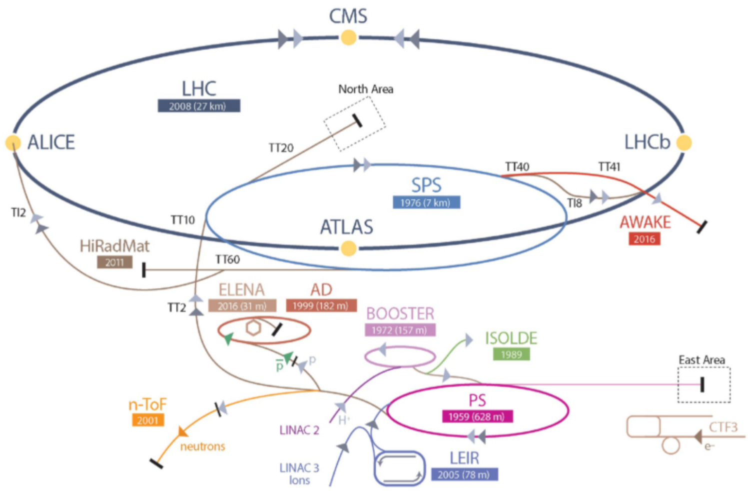

Figure 3.1: The CERN accelerators complex is composed by a chain of six main acceleration stations (both linear and circular), placed in sequence. Low energy protons are injected by LINAC 2 and 3 to the PS Booster where they reach a 4 GeV energy; then particles are sent to the PS (Proton Syncrothron, 24 GeV) and subsequently to the SPS (Super Proton Syncrothron), reaching an energy of 400 GeV. Finally, they are injected in LHC, where they are finally accelerated to approximately 7 TeV. Along the entire complex there are several secondary branches that lead to the experimental areas: H2 is a secondary beamline extracted from the SPS ring in the North Area site [109].

Figure 3.2: The North Area H2 beamline from above; the particle beam goes from the top right to the bottom left of the picture.

- a helium bag (He-BAG) used to considerably reduce the material on the path followed by photons and to avoid interactions with air molecules;
- a large area plastic scintillator (VETO) used as a photon veto;
- two different crystal samples (CRYS) mounted on a high-precision goniometer with a resolution of a few μrad in both the horizontal and the vertical axial rotations;
- a second large area plastic scintillator (S3, with dimensions comparable to the photon veto) employed as multiplicity counter;
- a large area single side x-y silicon strip chamber (C2), similar to that in front of the bending dipole;
- a modular electromagnetic Cherenkov calorimeter (GAMMA+eCAL), arranged and used as energy spectrometer;
- finally, two very large area silicon strip detectors (B1+B2) placed in front of the post-target charged beam deflected by the magnet.

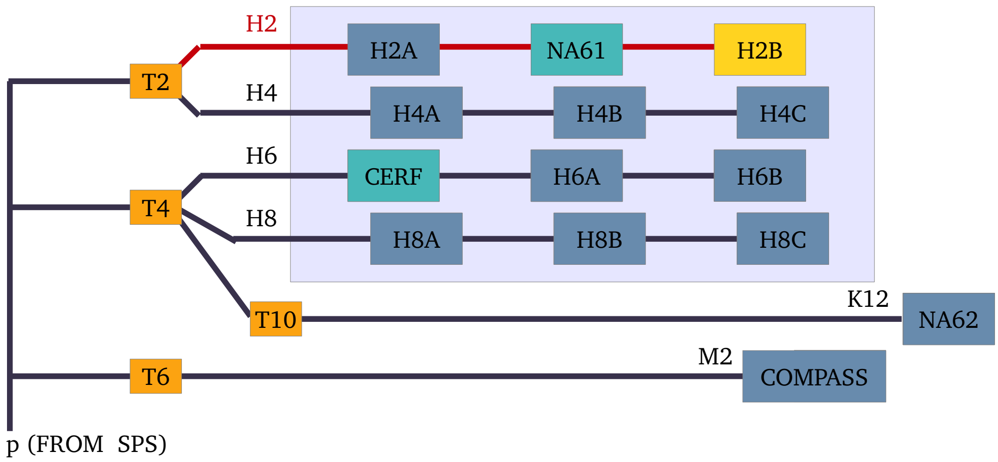

Figure 3.3: A schematic view of the CERN North Area beamline plan: the H2 line is highlighted in red on the top of the picture; the K_LEVER setup was installed in the H2B experimental area at the end of the beamline [110].

The two crystals mounted on the same holder used in the test are interchangeable along the beamline by means of the goniometer motion system; each one (as shown in fig. 3.6) has different dimensions, features, purposes and peculiarities:

- W(111) is a 10×10×10 mm^3 crystalline tungsten commercial sample by Princeton Scientific [112], which has been used in the K_LEVER setup as a photon converter;

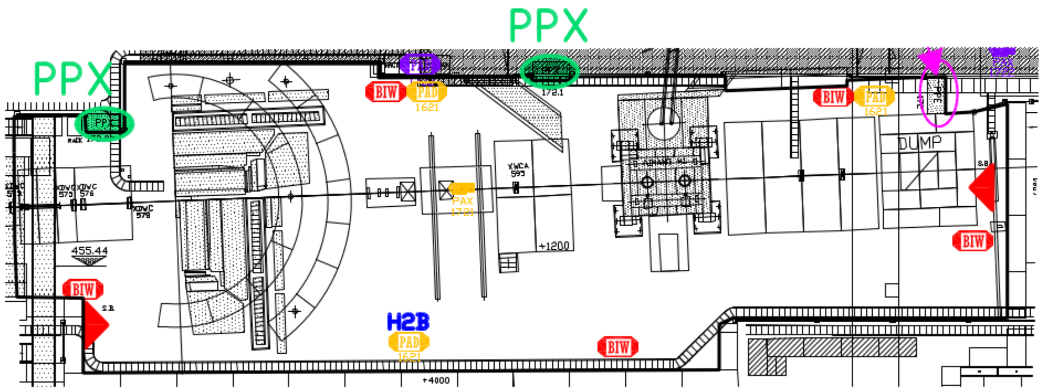

Figure 3.4: A map of the CERN North Area H2B experimental area; the beam is delivered along the horizontal line placed in the middle of the image, from left to right. The two arcs on the left belong to the CMS R&D calorimeter motion system [111].

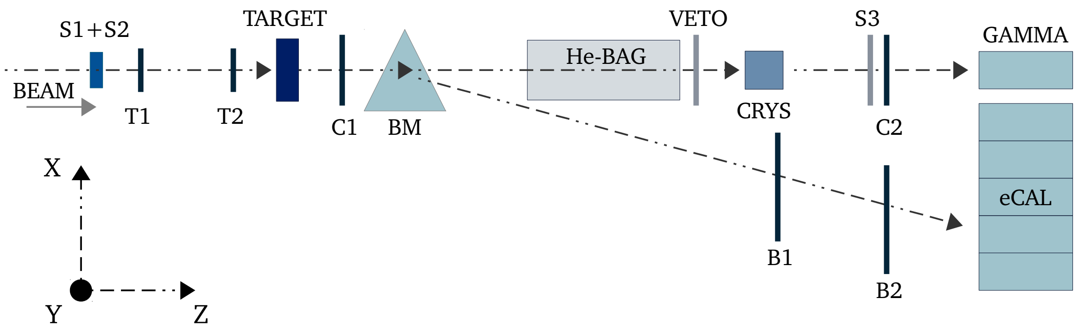

Figure 3.5: A schematic view of the K_LEVER setup on the H2 beamline in August 2018; from left to right, the beam crosses different elements and detectors: four plastic scintillators (S1+S2, S3 and VETO), four different size silicon microstrip detectors (T1 and T2, C1 and C2, B1 and B2), and finally the electromagnetic Cherenkov spectrometer (GAMMA+eCAL). In addition, along the beamline a copper target, a bending magnet and a helium bag are placed; the tested crystals (CRYS) are mounted on the goniometer and remotely interchangeable. The picture is not to scale.

- W(100) is, on the other hand, a high purity and high quality 2.2 mm thick tungsten crystal from RAS ISSP - Moscow [113], used to verify the coherent effects expected from the MC simulation.

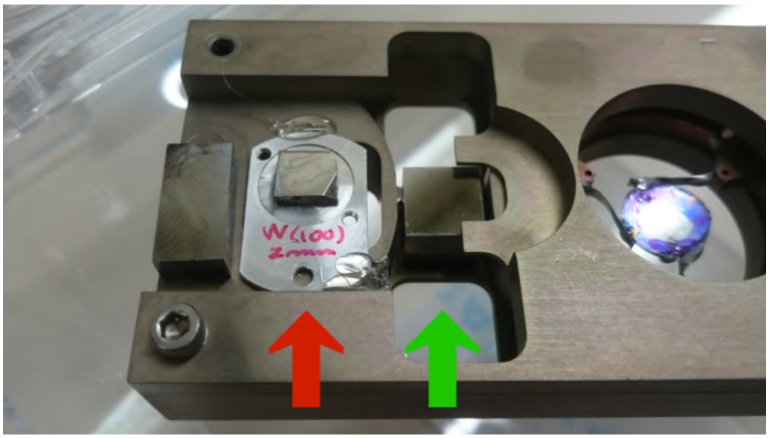

Figure 3.6: The two tested crystals mounted on the holder structure for the test performed by K_LEVER: the red arrow indicates the W(100) high purity crystal, while the green one points to the W(111) commercial sample.

3.1.2 THE TRIGGER SYSTEM

The very upstream section of the setup is used for the trigger generation before the beam impacts the copper target. Two plastic scintillators (S1 and S2) of $4{\times}9$ cm^2 of area and 7 mm of thickness in the z-direction, both mounted on the front face of the first silicon detector (T1) and read by standard high voltage PMTs[1] (fig. 3.7), form the first part of the trigger apparatus. The S1 scintillator has a hole of $3.5{\times}9$ mm^2, so that the trigger is given by the coincidence of the beamline spill[2] signal (sent by the accelerator monitoring systems), and the signal from S2 and the anticoincidence signal from S1. In this way, the system is forced to acquire only events that cross the hole of S1, collimating the beam and at the same time defining a maximum beam spot size.

3.1.3 THE TRACKING SYSTEM

The T1 and T2 detectors measure the incoming beam particle position with high accuracy: the choice of using double side microstrip silicon detectors for the tracking has been dictated by their many features, in particular a good spatial resolution both in the horizontal and in the vertical direction combined with a small amount of material

1 PhotoMultiplier Tube.
2 The beam extracted from the SPS ring is fed into the line in “bunches”; the single bunch is called “spill” and lasts about 4 s each cycle (whose period is variable between 20 and 45 seconds, depending on the machine).

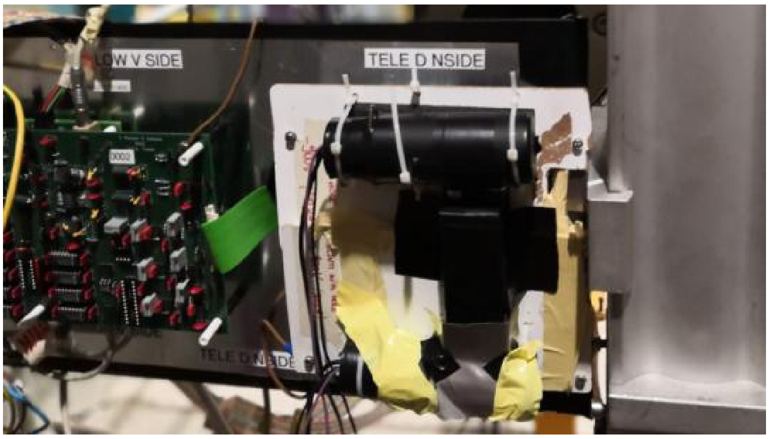

Figure 3.7: The S1 and S2 trigger scintillators assembled in front of the T1 detector.

in the beam direction (300 μm of silicon per module), thus excluding a considerable multiple scattering contribution. Each module covers an area of 1.92×1.92 cm^2 and it is composed by a junction side (p+ edge of the silicon tile) and an ohmic side (the n+ one). The two sides of the detector have the following features:

- the junction side consists of 768 25 μm wide strips; a floating strip readout scheme is applied, that is only 1 strip over two is actually read, resulting in a total of 384 channels with a 50 μm readout pitch;

- the ohmic side consists of 384 50 μm wide strips, so that both the physical pitch and the readout pitch are 50 μm.

The silicon strips of the detectors are fully depleted when a bias voltage in the 36-54 V range is applied. In both modules the silicon tile is glued onto a ceramic hybrid that hosts three 128 channel VA2 ASICs[3] connected to the strips via coupling capacitors. The entire structure is assembled on a fiberglass frame, contained in a steel box which holds the frontend electronics and the ADC[4] boards [114]. A picture of a detector module is presented in fig. 3.8. The last part of the readout chain is located in a VME[5] crate, placed near the DAQ PC.

The high spatial resolution of the two modules (5 μm on the junction side and 10 μm on the ohmic side [115]) allows to measure with high precision the trajectory and the input angle of the charged particles impinging on the 1 mm thick copper target, shown in fig. 3.9: this is a crucial step for the analysis and the reconstruction of the path of bremsstrahlung photons, assuming that they exit from the target at an angle that differs in the least from that of the incoming particle.

3 Application-Specific Integrated Circuit.
4 Analog to Digital Converter.
5 Versa Module Eurocard.

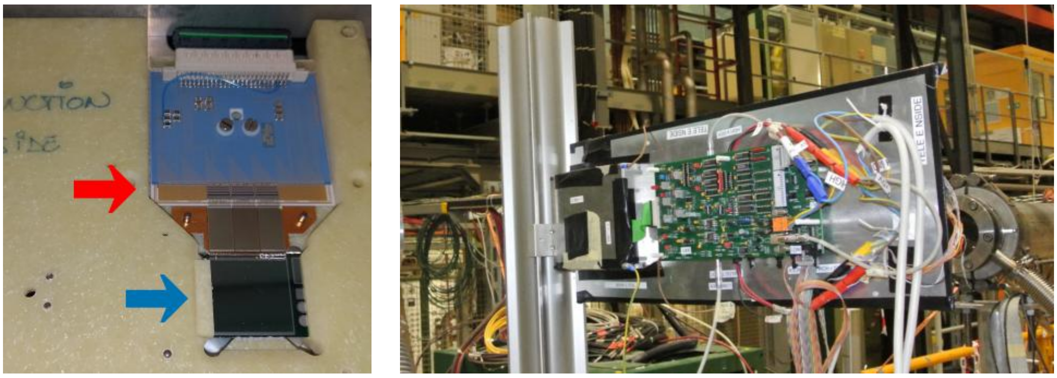

(a) Silicon detector & ASICs

(b) T1 module

Figure 3.8: (a) The detector of a silicon small area module: the blue arrow points to the silicon tile, while the red one points to the three ASICs; (b) a small area detector ready on the beam.

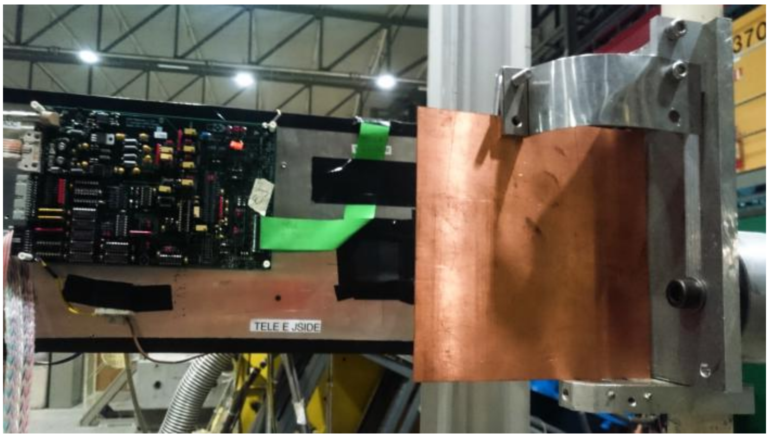

Figure 3.9: The copper target employed to generate the bremsstrahlung photon beam, mounted on its holder.

Just before the dipole bending magnet a silicon detector (C1) larger than the ones of the tracking section is used as beam monitor and as a single-cluster[6] event selector: the detector hosts two single side x-y microstrip silicon tiles (fig. 3.10), each one covering an area of 9.29×9.29 cm^2, and with a thickness of 410 μm. As in the small area modules, a floating strip readout scheme is used in such a way that, although the physical pitch of the strips is 121 μm, the readout pitch is 242 μm, resulting in 384 readout strips and a spatial resolution of 30 μm [116]. The signal readout chain is similar to the one used with the tracking system, employing three TA1 ASICs per layer (which provide a preamplifier, a shaper and a sample&hold circuit for each channel), a two-channel ADC board directly assembled on the detector and the remaining part of the data taking system located in a VME crate (fig. 3.11). The MBPL magnet used to separate both the primary electrons and secondary charged particles produced by collisions in the copper target from the bremsstrahlung photon beam is a 2 m gap uniform field dipole magnet, generating a nominal magnetic field of 4.0578 T·m at 850 A.

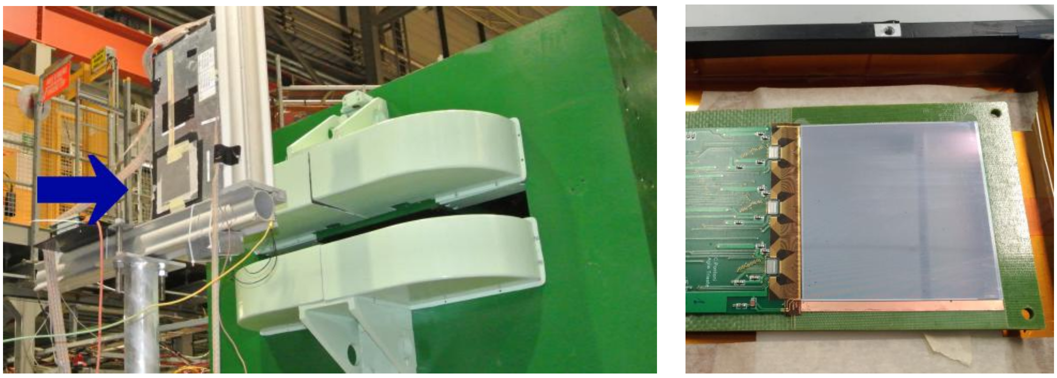

(a) A silicon beam chamber

(b) The silicon detector & ASICs

Figure 3.10: (a) The C1 detector (blue arrow) mounted on its support in front of the bending magnet and (b) the silicon microstrip detector of the beam chamber.

3.1.4 THE DOWNSTREAM SECTION

The large area ($\approx 15 \times 30$ cm^2) plastic scintillator shown in fig. 3.12 acts as a VETO detector, and it is used to discriminate, during the offline analysis, photons from charged particles using its output signal, or Pulse Height (PH). A 10×10 cm^2, 10 mm thick plastic scintillator detector, read by a standard high voltage HAMAMATSU PMT [117] placed behind the goniometer and the crystal along the beam trajectory, is used as a multiplicity counter. A similar task is performed by the silicon chamber positioned immediately behind the scintillator. The C2 detector has the same features as the C1

6 A "cluster" is defined as the group of contiguous strips hit by a particle, whose signals are all above a given threshold.

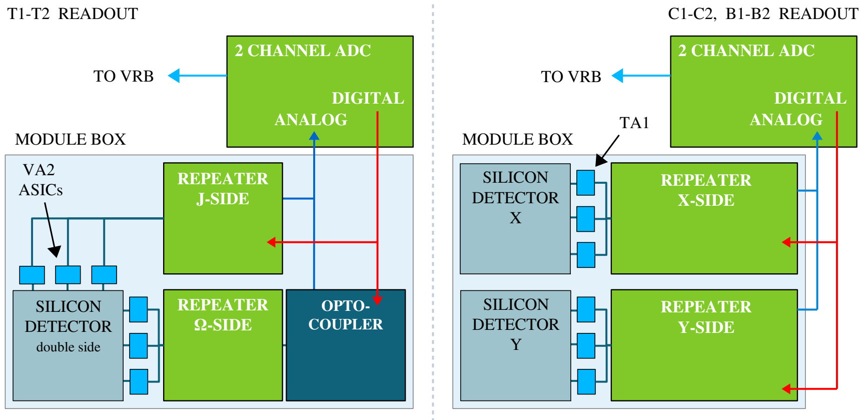

Figure 3.11: A schematic view of the silicon detectors readout chain: (left) the small area modules scheme, and (right) the beam chamber modules scheme.

beam monitor and it is used to study the pair production enhancement caused by the crystal looking at the cluster distribution in the detector itself.

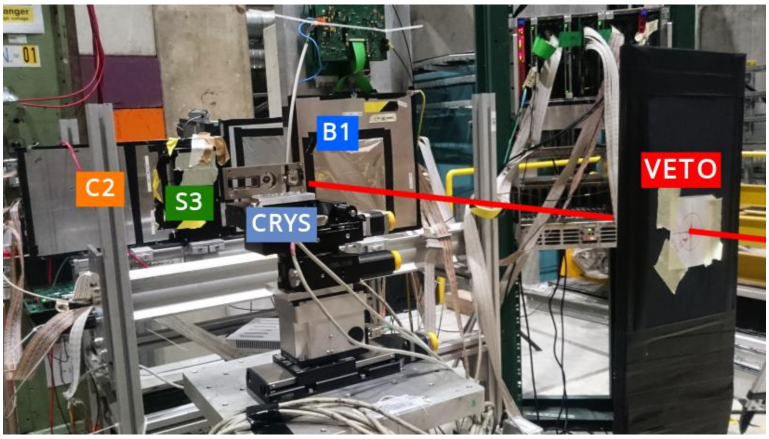

Figure 3.12: A frontal view of the last part of the K_LEVER setup. From right to left, the VETO plastic scintillator, the upstream large area silicon detector (B1), the crystal holder placed above the goniometer system and the S3 plastic scintillator fixed to the C2 silicon chamber; the red line indicates the beam trajectory.

In the downstream section two very large area silicon strip detectors (B1 and B2) identify the path of the primary and secondary charged particles deflected by the bending magnet. As shown in fig. 3.13, each module covers an area of 18.58×18.58 cm^2 obtained using four single side silicon detectors similar to those used for C1 and C2. Each couple of detectors is connected with bonding wires to form a 9.29×18.58 cm^2 ladder, as shown in fig. 3.14. Three 128 channel TAA1 ASICs are employed as frontend electronics and a strip floating scheme is applied, resulting in a readout pitch of 456 μm, given the fact that the physical pitch of the strips is 228 μm. A 4 mm small gap is present in the middle of the detector, due to the tile borders (fig. 3.13b).

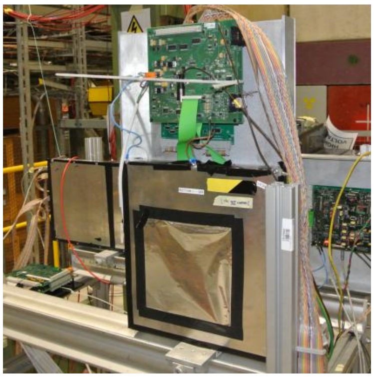

(a) A very large area silicon microstrip module

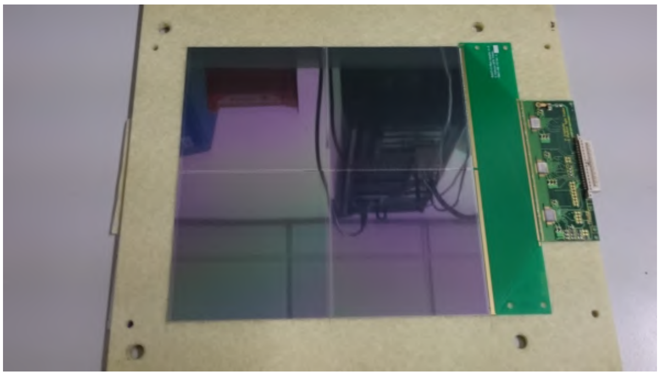

(b) The silicon tiles & ASICs

Figure 3.13: (a) The very large area detector with its readout electronics and (b) the silicon tile inside the box.

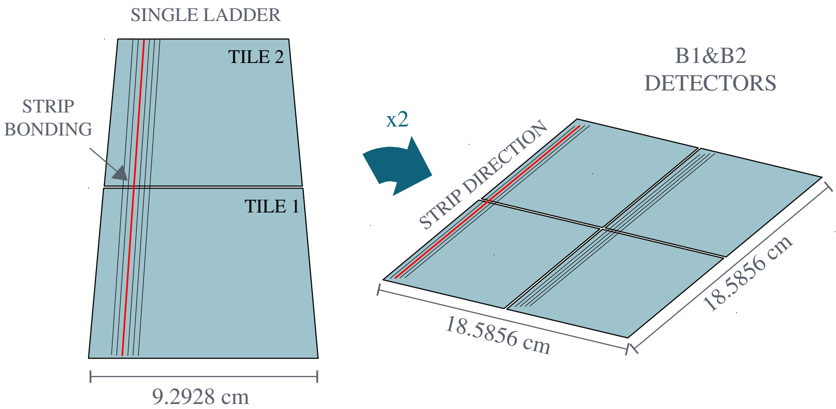

Figure 3.14: A schematic view of the B1 and B2 large area silicon detectors: two single side silicon tiles are bonded one to each other to form a single ladder; two ladders are matched side by side to form the detector.

3.1.5 THE SPECTROMETER

The experimental setup is completed by two different groups of detectors that act as spectrometer: one (called GAMMA) dedicated to the beam exiting the crystal (along the beamline) and the other (named eCAL) to the charged particles deflected by the magnet. The spectrometer is designed to measure the energy E_p of the charged particles after the bending magnet and the energy E_γ of the photon, where $E_\gamma = E_{beam} - E_p$. The core of the spectrometer consists of homogeneous Cherenkov lead glass calorimeters (≈24.6 radiation lengths and $\sigma_e/E(\%) = 6.3/\sqrt{E} + 0.2$ [118]) spare modules of the OPAL[7] [119] electromagnetic calorimeter: although they are largely reliable and well known instruments, during the test an evident drift of the signal amplitude as a function of time required an offline calibration method to compensate the unexpected effect. A few photos of the spectrometer are presented in fig. 3.15, while the offline correction procedure is described in Sec. 3.6. The whole spectrometer is positioned on a movable stage ("Desy table").

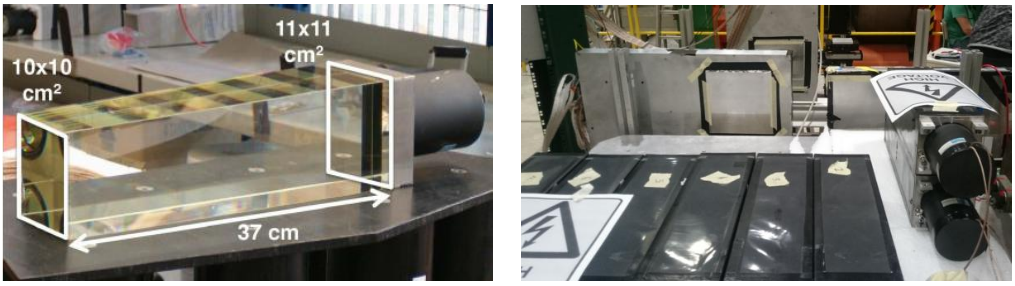

(a) a OPAL Cherenkov calorimeter [120] **(b)** The electromagnetic spectrometer

Figure 3.15: (a) A OPAL Cherenkov lead glass detector without the protection cover and (b) a rear view of the two sides of the spectrometer in the experimental area.

3.2 THE DAQ SYSTEM

Fig. 3.16 shows in a schematic way the structure of the Data AcQuisition (DAQ) system, based on the VME standard. The data taking procedure is the following:

- the signals exiting the S1 and S2 trigger scintillators are sent to a discriminator; if there is the anticoincidence between the two detectors, *i.e.* the S1 signal is below a given threshold and S2 shows a signal, the discriminator generates a digital signal. The coincidence between this signal and the SPS spill generates the trigger;

7 OPAL (Omni-Purpose Apparatus for LEP) was one of the LEP experiments.

- the trigger is sent to the master VRB[8], which generates a busy signal that acts as trigger for the slave VRBs (the ones of the other silicon detectors) and for the digitizer (the one for the calorimeter);
- each VRB generates the hold (*i.e.* the time needed for the ASICs to shape the input signal) for all the silicon detectors;
- in the readout phase the output signals from the silicon detectors are digitized by dedicated two channel ADCs, and then sent to the corresponding VRB where they are stored until the end of the spill, when they are transferred to the PC disk;
- at the same time, the signals coming from the veto and S3 scintillators and the spectrometer channels are read and digitized by the CAEN V1730c digitizer and stored temporarily in the PC memory; at the end of the spill, they are saved on disk;
- the readout of the angular and linear stages of the goniometric system is performed by optical encoders, remotely controlled by the DAQ;
- the data are saved in HBOOK ntuples [121];
- an online pre-processing procedure selects the events that present a single cluster in the T1 and T2 detectors and it produces ASCII[9] files in which all the information of the single event are arranged in columns: the number and the Unix time of the event, the time from the beginning of the run, the positions of the goniometer stages, the positions and the number of the clusters (up to a maximum of 5) identifying the hits on the silicon detectors, the pulse heights of the VETO, the S3 scintillator and of all the spectrometer channels.

3.3 PRELIMINARY BEAM STUDY

This section is dedicated mainly to the preliminary studies on the particle beam without the target and the crystals, acquiring runs with beams of different energy and in presence or absence of the deflecting field of the magnet, in order to characterize the beam features as accurately as possible. 120 GeV/c electrons are used as primary beam: they are obtained as secondary products of the SPS 400 GeV/c protons interaction with appropriate targets, collimators and selectors distributed along the first part of the H2 line. The nominal intensity of the beam per pulse is $\approx 4\times 10^6 e\pm$ at 150 GeV/c [110]. The dimensions and the beam spot shape have been determined using the T1 and T2 detectors: the beam profiles are shown in fig. 3.17 in the x and y directions, while fig. 3.18 presents a 2D plot of the beam on the T1 detector. The particular beam shape

8 VME Readout Board.
9 American Standard Code for Information Interchange.

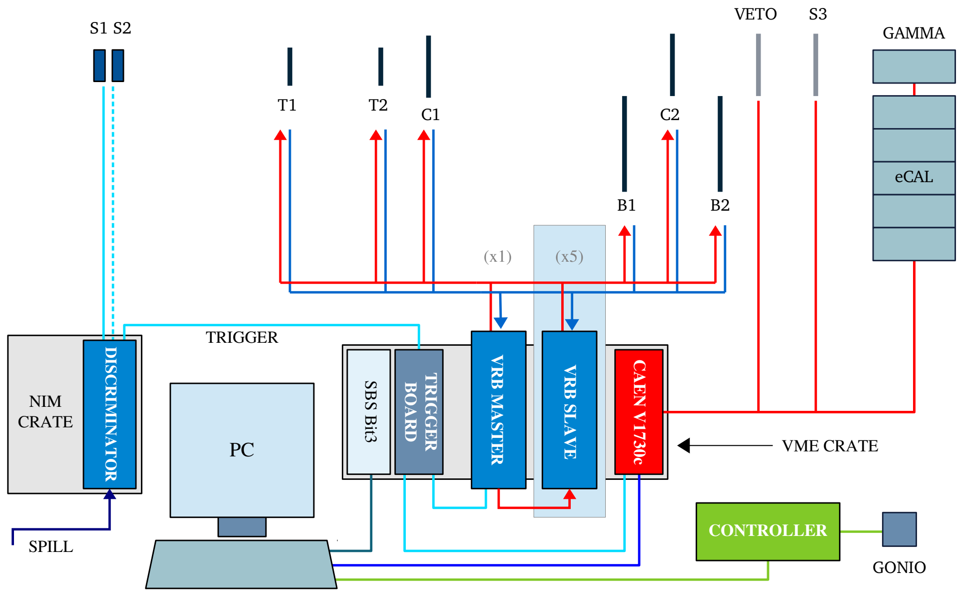

Figure 3.16: The DAQ layout.

is due to the trigger system, based on the anticoincidence of the signals coming from S1 and S2, placed both just before the first silicon small area module; the shape along the y axis corresponds to the shape of the S1 hole. The beam spot diameter has been measured to be about 3.5 mm in x and 8.5 mm in y.

3.3.1 THE ALIGNMENT PROCEDURE

To obtain the particle input angles and precisely reconstruct their trajectory, it is crucial that all the detectors are correctly aligned along the whole setup. The preliminary manual alignment does not allow to correct any relative shifts between the detectors in the x-y plane perpendicular to the beam direction; these shifts turn into an incorrect reconstruction of the input particle track. It is therefore necessary to perform a precise alignment via software.

The procedure consists in aligning all the detectors with respect to one taken as a reference (T1) in the following way:

- the distribution of the differences (also known as residuals) between the positions recorded on the detector to be aligned x_i and on the reference one x_r is computed as x_i-x_r (as shown in fig. 3.19);
- a fit of each distribution with a Gaussian function is then performed;
- the alignment is obtained by subtracting to x_i the average value of the Gaussian, in order to center the difference in zero.

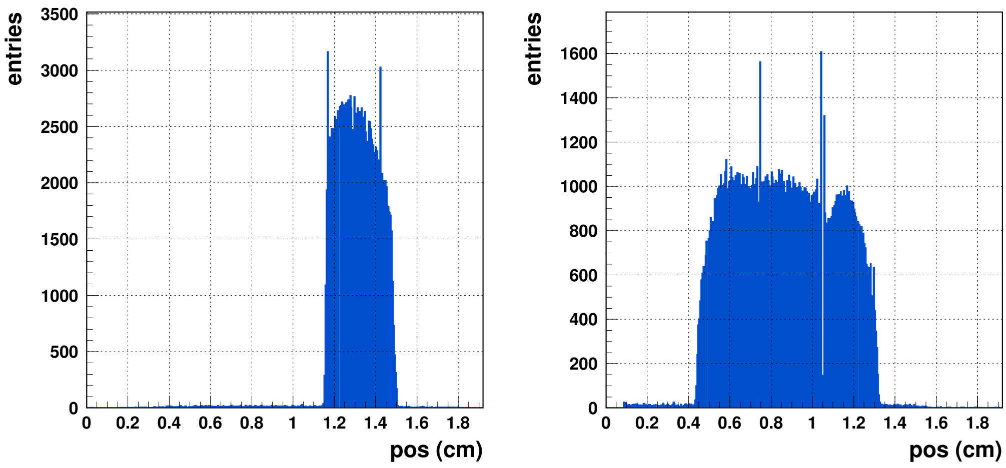

(a) T1 x profile

(b) T1 y profile

Figure 3.17: (a) x and (b) y beam profiles on the T1 silicon detector. The presence of peaks superimposed on the general profile of the beam is due to some noisy strips of the detector itself; however, they do not influence the subsequent data analysis.

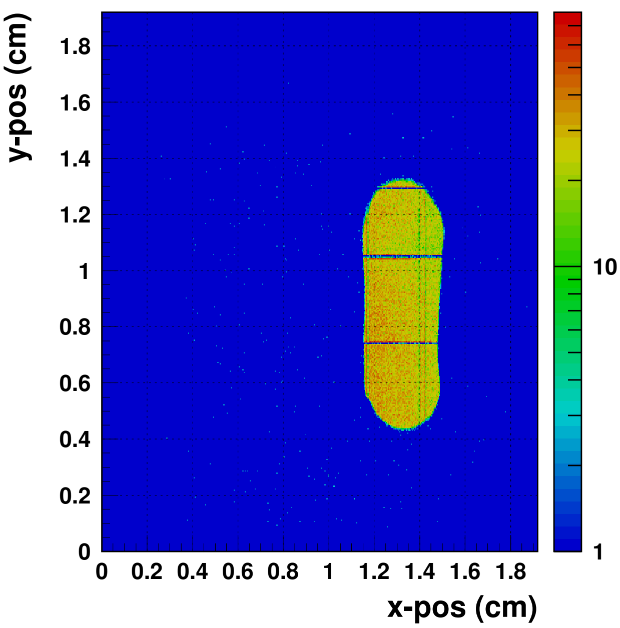

Figure 3.18: T1 beam profile; the shape of the beam is due to the hole of the S1 trigger detector.

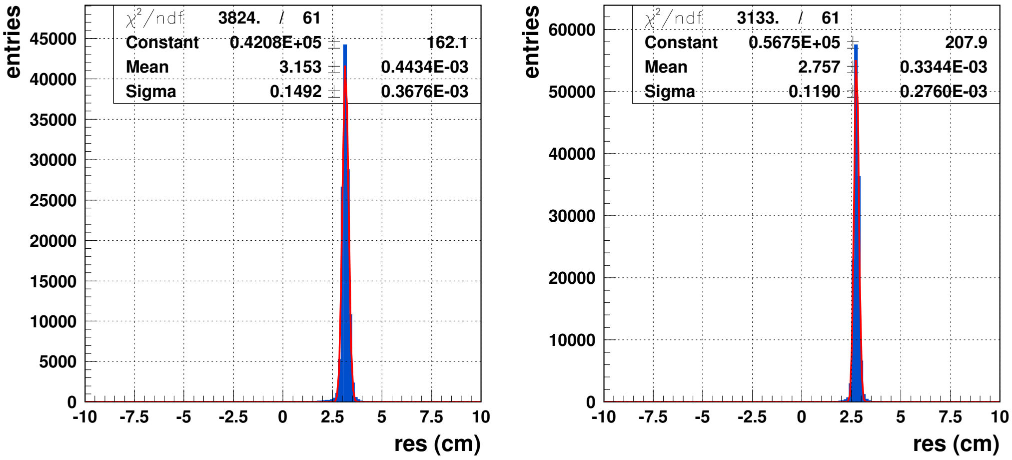

(a) C1 x residual distribution **(b)** C1 y residual distribution

Figure 3.19: (a) x and (b) y residual distributions of the C1 silicon chamber with respect to the T1 detector.

The described procedure is performed for both the x and y directions. The translations necessary for the alignment procedure are listed in tab. 3.1, while an example of the residual distribution after the alignment is shown in fig. 3.20. It is now possible to study the divergence of the beam, defined as the spread of the angular distribution of the incident particles; this distribution is obtained with the following formula:

$$\alpha_{in}^{(x)} = \arctan\left(\frac{x_2 - x_1}{d}\right) \tag{3.1}$$

where x_1 and x_2 are the x positions recorded by the two detectors, while d is their distance. The same procedure is performed along the y direction. The distributions obtained in the two directions after the alignment process are shown in fig. 3.21. For a well-aligned tracking system, the distribution of the input angles must be centered in zero: this is verified performing a Gaussian fit on each detector distribution. The beam divergence extracted from the fit parameters results to be 78 μrad in x and 64 μrad along the y direction. The divergence of the beam is small enough to allow the study of the coherent phenomena with a good statistics in the angular acceptance of the effect (assumed to be about 1 mrad).

The last step is the study of the deflected beam performed with the spectrometer. It is essential to evaluate the energy range covered by the "electron" section of the calorimeter array, to determine the total energy of the charged particles deflected by the bending magnet and to compare it with the energy collected by the detector placed along the beamline (the one detecting the photon beam impinging on the crystal). A pure positron beam energy scan in the range 20-120 GeV is performed while maintaining the bending magnet on at the operative current level; each PH spectrum is then studied for each energy step (fig. 3.22 shows a schematic of the procedure), combining data from

Detector #	x-shift (cm)	y-shift (cm)
T1	0.	0.
T2	-0.069	0.285
C1	3.153	2.756
C2	6.145	1.832

Table 3.1: x and y shifts applied to the silicon detectors along the beamline during the alignment procedure.

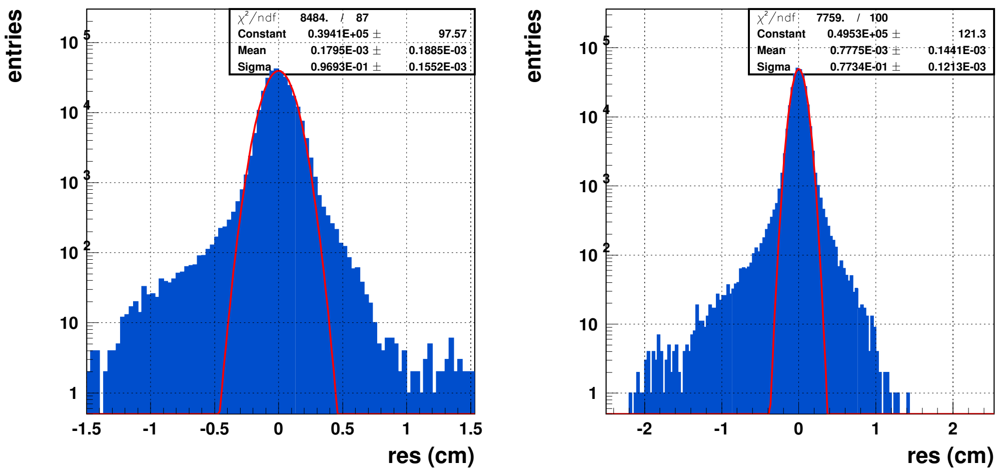

(a) C1 x residual distribution

(b) C1 y residual distribution

Figure 3.20: (a) x and (b) y residual distributions of the C1 silicon chamber with respect to the T1 detector after the alignment procedure.

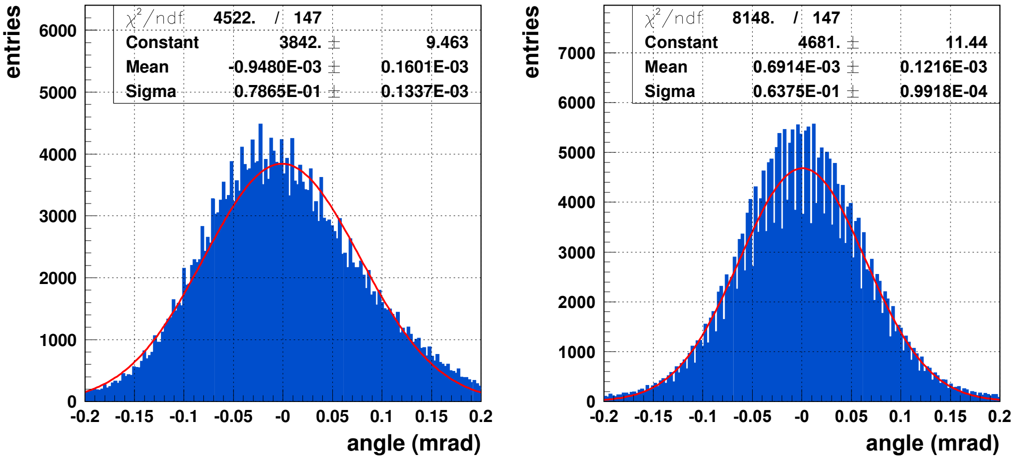

(a) beam x angular distribution

(b) beam y angular distribution

Figure 3.21: (a) x and (b) y angular distributions after the alignment procedure: a Gaussian fit is performed, in order to obtain the beam divergence.

each calorimeter into a single plot: in this way it is possible to obtain the spectrum seen by the whole spectrometer in its single channels as a function of the beam energy. As shown in fig. 3.23, the beam moves from one Cherenkov detector to the following going down in energy: at 120 GeV it is located in the channel closest to the non-deflected beamline (on the left side of the plot), while it is in the region out of the spectrometer at 20 GeV.

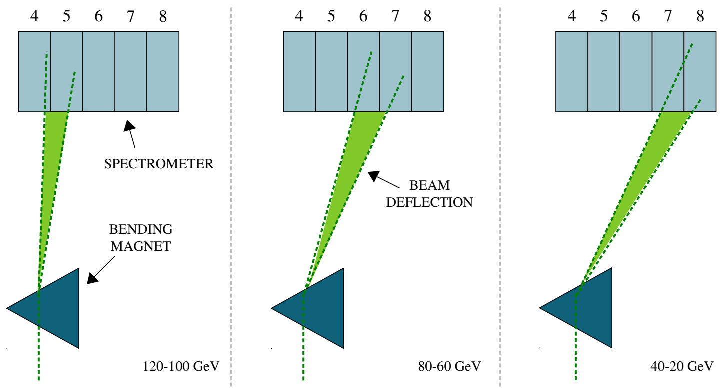

Figure 3.22: The schematic of the spectrometer scan: decreasing the energy, the beam is increasingly deflected towards the outer part of the spectrometer, crossing its different sections.

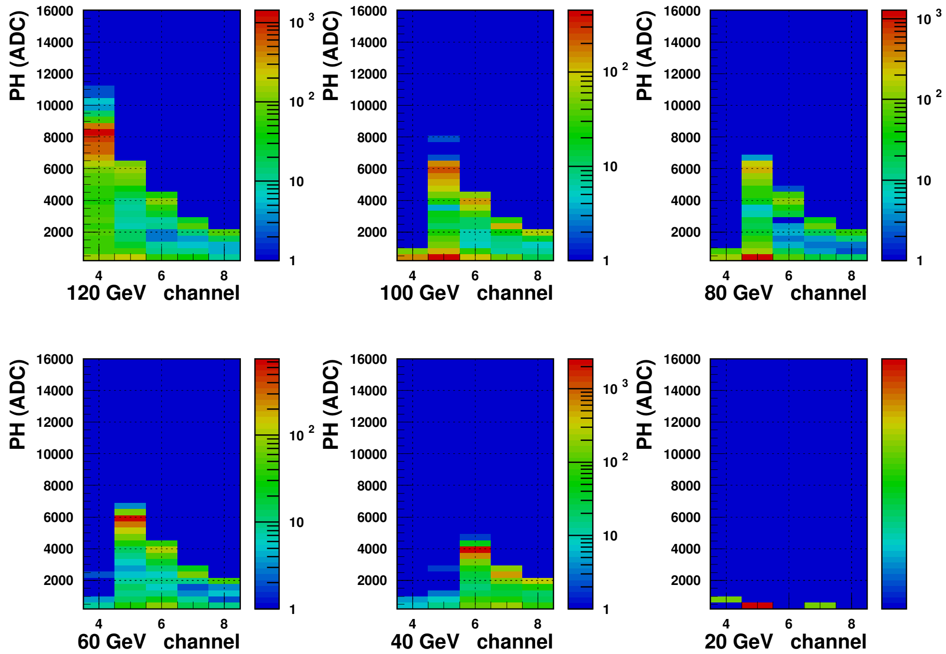

Figure 3.23: The spectrometer momentum scan: from top-left to bottom-right, the positron PH spectra (from 120 GeV to 20 GeV) of the Cherenkov detectors; notice the shift of the energy peak towards the right channels while the beam energy decreases.

3.4 CRYSTAL POSITIONING

The study of coherent phenomena of hard photons in a crystal lattice requires a very accurate alignment system to orient the crystals with respect to the neutral beam. The measurements described in this work use a high precision goniometric system, controlled by the DAQ to allow the precise positioning of the crystal along the beam and to reach the needed angular alignment between the lattice planes and the direction of the impinging photons. A picture of the system is shown in fig. 3.24. The goniometer consists of different components:

- a linear stage for the horizontal movement along the x direction;
- a vertical one;
- a rotational stage to align the crystal lattice with respect to the incoming beam on the x-z plane, with an accuracy of the order of a few μrad;
- an additional rotational stage (named cradle) to align the crystalline planes in the y-z direction.

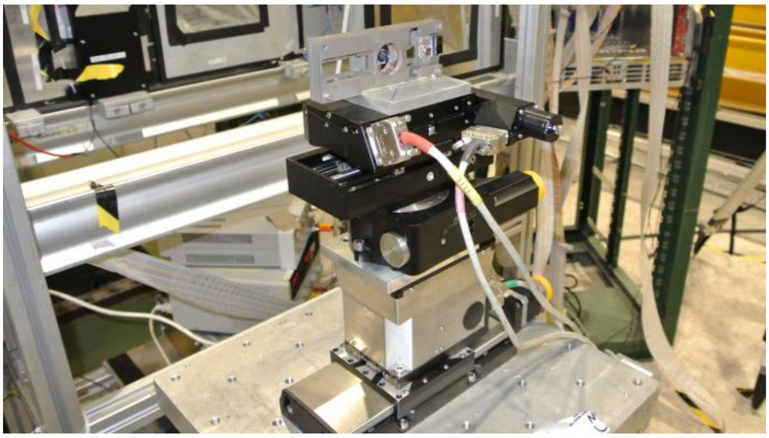

Figure 3.24: The crystal goniometer.

3.4.1 THE LASER ALIGNMENT

Firstly a coarse pre-alignment is performed by means of a laser light aligned with the direction of the beam, as described in fig. 3.25a. A pentaprism (fig. 3.25b) directs the light beam perpendicular to the direction of the particles; the laser is then reflected by a mirror previously mounted on the holder containing the crystalline samples. Once the incoming and the reflected beam overlap, crystals are in good approximation aligned with (and so perpendicular to) the incoming beam.

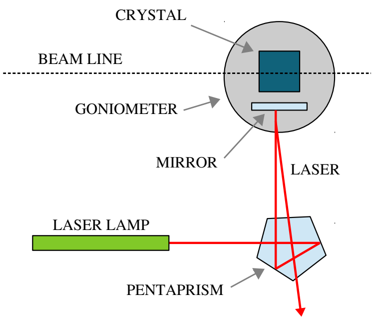

(a) A schematic of the coarse laser alignment

(b) The pentaprism

Figure 3.25: (a) The laser pre-alignment technique and (b) the pentaprism glued to its holder.

3.4.2 THE FINE ALIGNMENT

Each crystal is then positioned along the beam trajectory by means of a lateral scan, acquiring data with the goniometric system and the GAMMA calorimeter; the position of the crystal with respect to the beam is inferred from the study of the PH of the rear calorimeter as a function of the step of the lateral and the vertical scan, as shown in fig. 3.26. To confirm the alignment position, it is possible to visualize the crystal shadow inside the beam halo: a 2D plot of the x and y positions at a z corresponding to that of the crystalline sample is created considering the constraint of a single cluster both in x and in y on the C2 chamber, as shown in fig. 3.27.

The search procedure ends with an angular and a cradle scan, determining the exact channeling position (fig. 3.28). For each performed scan, the optimal position of the goniometer (and therefore of the crystal) corresponds to the maximum change obtained in the PH of the Cherenkov calorimeter:

- in the lateral and the vertical scans, the beam interacts with the crystal which causes multiple scattering and thus a reduction of the PH;
- on the other hand, in the angular and the cradle scans secondary particles of energy smaller than that of the primary beam are produced by the channeling condition. A secondary peak appears in the PH of the calorimeter, and its maximum evidence defines the optimal position.

The procedure was performed on both crystals.

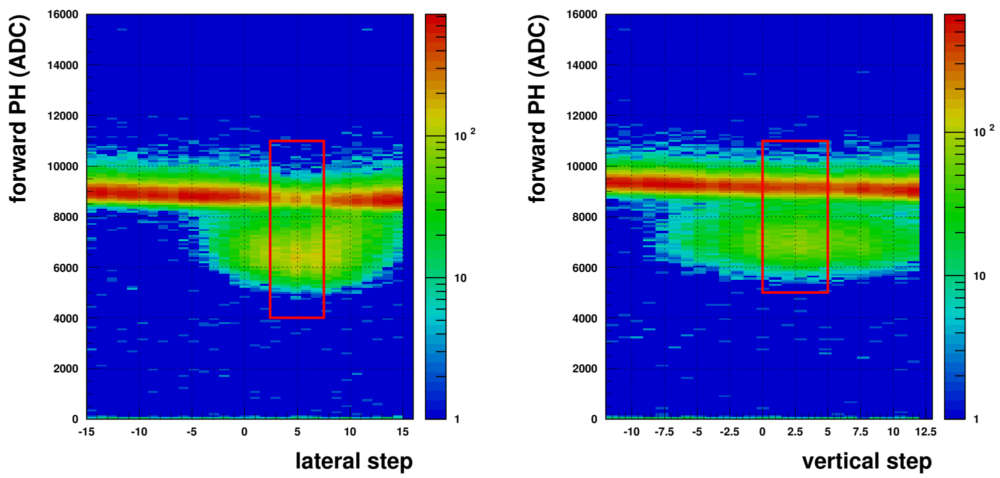

(a) Lateral scan

(b) Vertical scan

Figure 3.26: (a) The lateral and (b) the vertical scan used to obtain the right W(111) crystal position with respect to the beam, which corresponds to the maximum change in the PH of the rear calorimeter: the red boxes indicate the correct step number of the goniometer to be used.

For each of the crystalline samples, tests in the channeling condition and in amorphous condition (completely disaligned) were performed in order to check the crystal behaviour. In addition, some points in a quasi-channeling condition (*i.e.* at an angle

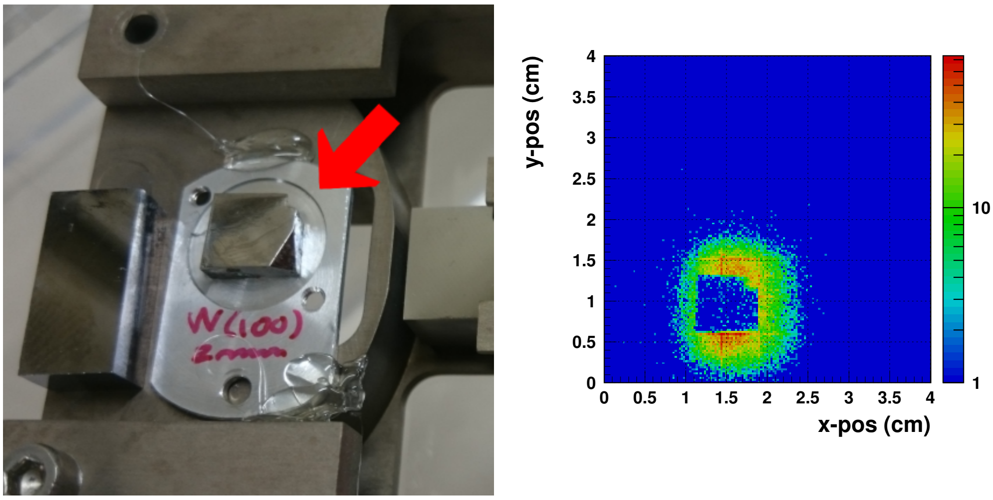

(a) The W(100) crystal **(b)** The W(100) beam halo

Figure 3.27: (a) A picture of the W(100) crystal and (b) the W(100) crystal halo; the red arrow points to the chipped corner of the crystal, visible in the beam profile.

of misalignment with respect to the channeling direction of the order of 2.5 mrad for W(111) and 0.5 mrad for W(100)) have been taken for a more in-depth study of the characteristics of the crystals.

3.5 ONLINE CALIBRATION

These last two sections describe the characterization, the calibration and the offline compensation of the Cherenkov spectrometer. The calibration routine matches the signal from the detectors (encoded by the DAQ digitizers as numbers) to the energy of the impinging particle, which is obtained from the beam setting. The calibration procedure is performed in dedicated runs (in which the copper target and the crystals are removed from the beamline) in the following way:

- the Cherenkov detector to be calibrated is aligned with the beamline by means of the Desy table;
- a few low statistics runs are acquired using electron beams with increasing energy directly hitting the detector. The incident particles release their energy within the detector in the form of Cherenkov light, which is collected by the photomultiplier tube placed in the rear part of the calorimeter;
- the output signal from the PMT is digitized by the acquisition system by means of a CAEN V1730c digitizer [122];
- the particles that cross the central area of the detector are selected via software, in order to limit the lateral leakage of the electromagnetic shower (fig. 3.29);

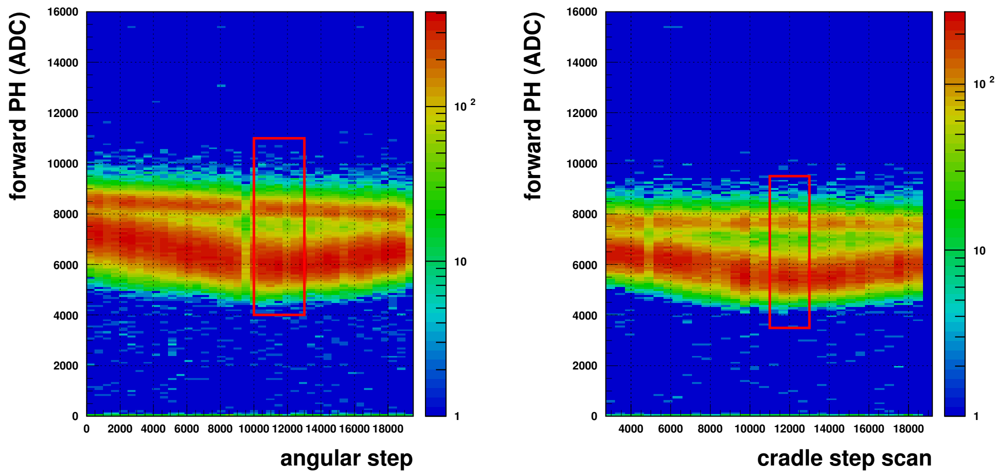

(a) Angular scan **(b)** Cradle scan

Figure 3.28: (a) The angular and (b) the cradle scan used to obtain the channeling condition for the W(111) crystal; as in the previous case the red boxes indicate the correct goniometer position.

- a fit with a Gaussian function of the PH of the ADC spectrum thus obtained is performed; the peak position, expressed in arbitrary units, is directly proportional to the energy of the beam particles (fig. 3.30);
- the mean values are then plotted as a function of the corresponding primary energy and fitted with a linear function (fig. 3.31).

The calibration scan was performed daily using energies of 40, 80 and 120 GeV; the calibration parameters obtained from the preliminary analysis and used in the data analysis are collected in tab. 3.2.

3.6 OFFLINE COMPENSATION

The last section of this chapter describes the offline routine conceived to correct the PH deviations in some of the detectors of the spectrometer. Further offline analysis of the collected data has been performed after the end of the beamtest, at the INSULab laboratory of the Insubria University in Como. In particular, the focus of this second analysis has been a software correction of the unexpected drift in the Cherenkov calorimeters response. In literature [123] drift problems of any kind in these detectors are not cited. In the K_LEVER beamtest, however, the change in response over time was evident: as an example, fig. 3.32 shows the PH of the first Cherenkov calorimeter as a function of time (expressed as event number), in which the decrease in the value of the detector signal is clearly visible.

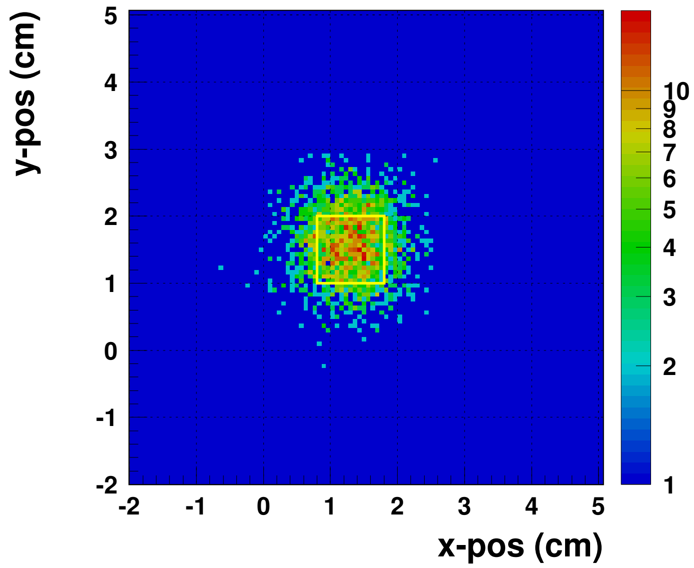

Figure 3.29: An example of the position cut performed via software; the yellow box defines the selected area.

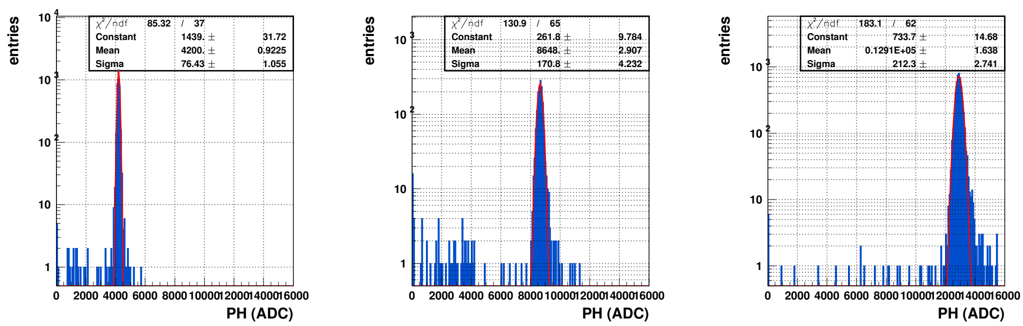

(a) 40 GeV **(b)** 80 GeV **(c)** 120 GeV

Figure 3.30: Examples of a (a) 40 GeV, (b) 80 GeV and (c) 120 GeV positron PH of the fifth Cherenkov detector fitted with a Gaussian function during the calibration procedure.

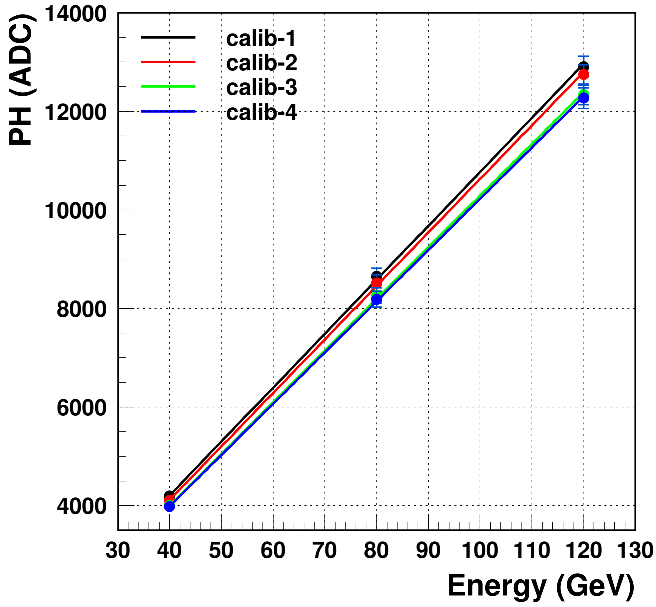

Figure 3.31: The ADC *vs.* energy plot for the fifth calorimeter; each line refers to a single calibration procedure.

Spectrometer channel #	Calibration #1	Calibration #2	Calibration #3	Calibration #4
1	79.47	102.01	110.03	95.94
	-111.60	-217.03	-210.64	-167.05
2	78.80	72.95	80.50	77.11
	-123.34	-149.41	-195.68	-195.33
3	109.04	108.03	107.20	104.25
	-132.83	-183.24	-169.26	-143.97
4	101.93	101.90	102.76	100.69
	-74.46	-77.93	-82.33	-109.00
5	80.00	82.54	82.43	82.16
	-169.47	-173.80	-171.44	-168.00
6	83.01	85.21	84.90	85.11
	-115.17	-141.42	-148.60	-169.02

Table 3.2: The parameters used for the calibration procedure: for each detector and each scan, the first value refers to the conversion factor ($\frac{ADC}{GeV}$), the second one to the offset (ADC).

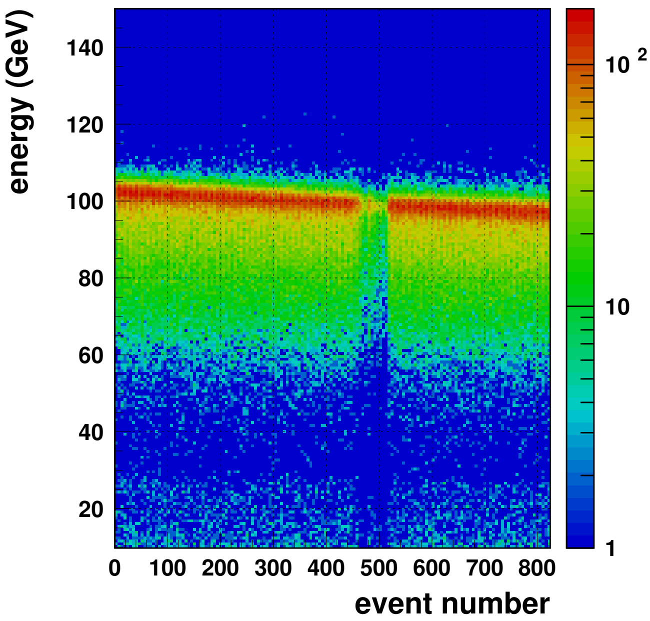

Figure 3.32: The PH variation as a function of time of the first Cherenkov detector of the spectrometer; the hole at the midpoint of the plot is due to the beam temporary absence during the acquisition time.

The correction procedure has been performed taking into account three elements:

- the beam parameters have not been modified for the duration of the whole beamtest, therefore the drift is not due to a change in the energy of the incoming particles;
- no bending magnet malfunction has been found studying the beam position on the B1 and B2 detectors;
- a drift due to the change in the environmental temperature of the experimental zone has been excluded, since the behavior was not related to the day-night alternation and was not the same in all the detectors.

A possible cause of this anomalous behavior has then been attributed to a malfunction of the voltage divider of the readout PMTs: this has been confirmed by observing in the innermost calorimeter of the spectrometer an evident deviation of the signal, which occurred about halfway through the test week (fig. 3.33).

Two software correction routines have been proposed, described in the following sections: in the first one a general rectification of the detector response is performed considering only the initial and final conditions of the detector in a single run; the second procedure follows a more sensitive approach to the substantially non-linear variation of the PH over time.

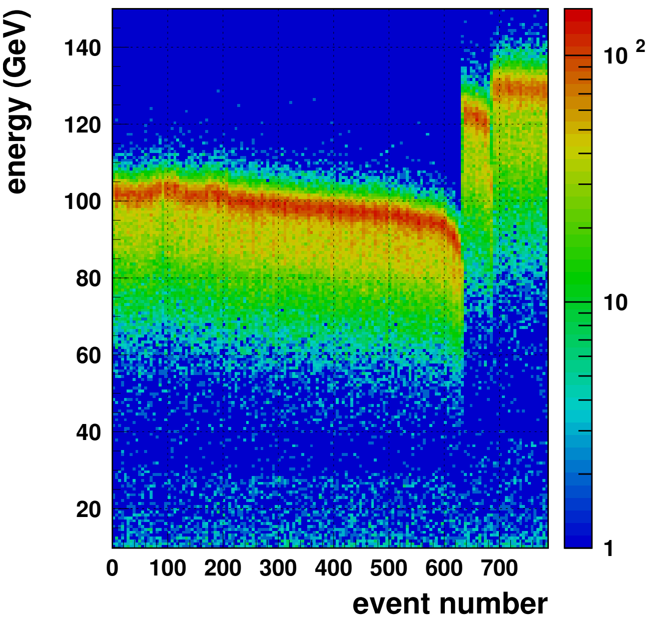

Figure 3.33: The evident deviation of the signal level in the first Cherenkov detector of the spectrometer; the detector has been promptly replaced.

3.6.1 THE LINEAR APPROACH

Each run consists of a set of ASCII files, as many as the spills recorded by the experimental setup during the acquisition time; the correction procedure is applied to all the files composing a single run. Each run file is distinguished by the number of the run (the same for all) and by the spill number (in ascending order); within each individual file, individual events read by the DAQ are saved as data strings, as described in Sec. 3.2. The first correcting procedure of the detectors signals assumes that the variation of the detectors PH follows a linear trend along the whole duration of a single run. Once the trend line has been found, the descending trend of the signal is corrected by adding to the PH of each detector a corrective factor (fig. 3.34).

The procedure is applied as follows:

- for each detector (i) the mean PH value $M_{i,in}$ considering only signals above a given threshold (fig. 3.35) is computed for the first 20 files of the run; the channel mean value is computed as:

$$M_{i,in} = \frac{\sum_{20\ file} (PH\ over\ threshold)_i}{(\#\ events)_i} \tag{3.2}$$

  so that $M_{i,in}$ is the sum of each row of each file of each detector PH divided by the total number of lines read by the subroutine;

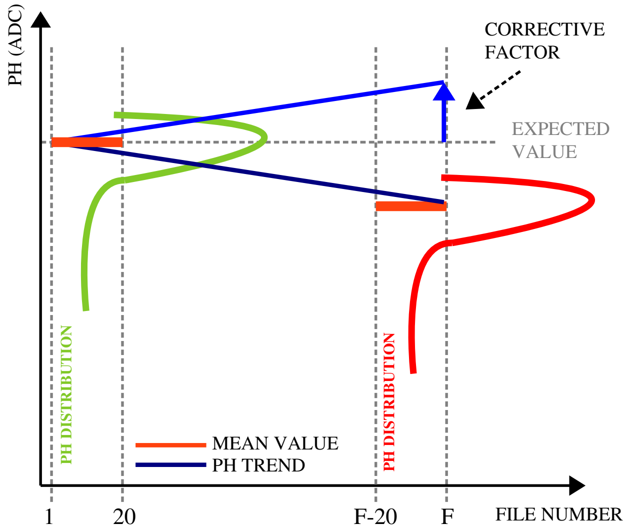

Figure 3.34: A schematic of the linear approach routine; the algorithm computes the average of the first 20 and of the last 20 files of the run (red lines), and finds a trend line (dark blue line). The signal decreasing trend is compensated by adding to the raw PH a corrective factor according to the trend line as a function of the corresponding file number (blue line).

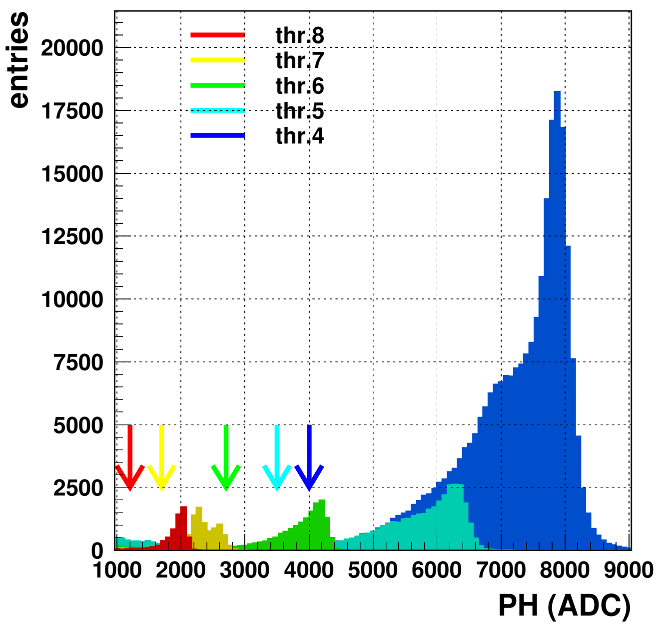

Figure 3.35: The PH distributions of the spectrometer detectors; each arrow points to the threshold of the corresponding channel.

- a second subroutine selects the last 20 spills and computes the mean PH value $M_{i,last}$ for each channel in the same way as in the previous step;

- a trend line is computed for each detector, according to the formula (fig. 3.36):

$$M_{i,last} - M_{i,in} = \alpha_i \cdot (file_{last} - file_{in}) \tag{3.3}$$

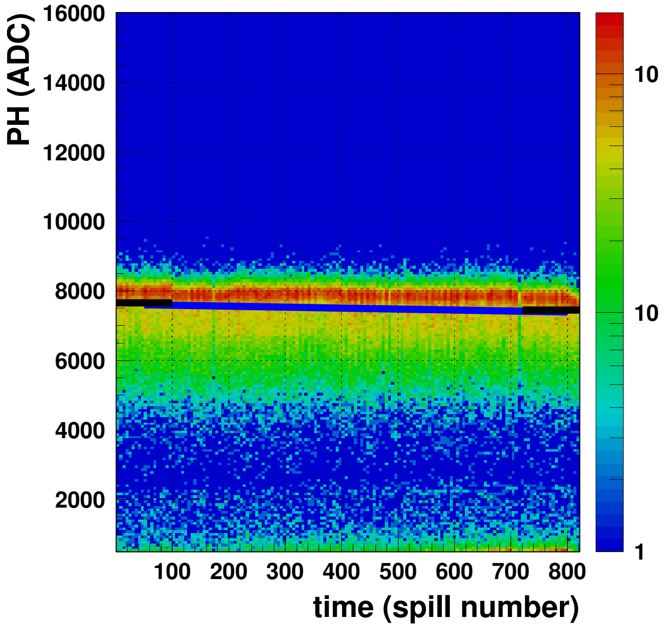

Figure 3.36: An example of PH distribution as a function of time; the mean values of the initial and final events (black lines) and the trend line obtained from the correction routine (in blue) are shown.

- the angular coefficients α_i are used in the data correction, performed on a second cycle on all the files:

$$PH_{i,corr} = PH_i - [\alpha_i \cdot file] \tag{3.4}$$

- in this way, a corrective factor is added to the PH value, opposing the detector signal trend (fig. 3.37);

- the corrected data are then used in the data analysis routine.

An example of the results obtained by applying this first correction routine is shown in fig. 3.38; the goodness of the correction procedure is verified by means of a linear fit on the new PH values with respect to the file number, as shown in fig. 3.39.
The linear procedure manages to rectify the response of the detector, although it slightly

underestimates the PH value in the mean computation: the lower value can be explained by the presence of a low energy queue in the PH distribution of the detector; nevertheless, to face with longer runs, a more accurate procedure is used.

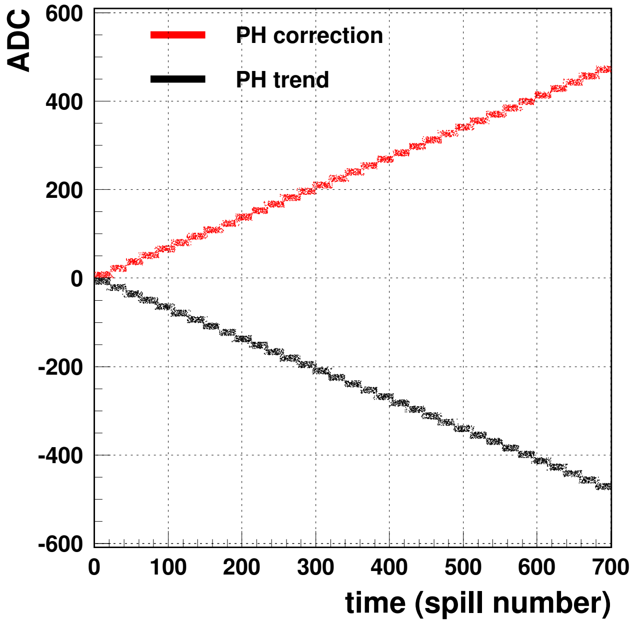

Figure 3.37: An example of the PH trend and the corrective factor as a function of time applied to the Cherenkov detector n.4, in the linear approach procedure.

3.6.2 THE SEGMENTED APPROACH

The second procedure is in many ways an improvement of the first: it has been designed to take into account the non-linear trend as a function of time of the calorimeter signals. The basic concept is to divide each run into segments of 60 files each [10] as shown in fig. 3.40, and then apply the same procedure used in the linear approach (fig. 3.41). The procedure is the following:

- the same compensation described in Sec. 3.6.1 is performed on the first 60 files;
- for each computed correction function, the average value of the PH at the end of the segment is stored in memory; the value is then compared with the average value of the initial part of the following group of 60 files, to obtain an offset $B_{i,section}$ to be added to the correction procedure, so that:

10 The number of files in which the run has been divided is chosen based on the length of the spill cycle: assuming 40 seconds per single cycle, a period of 60 spills corresponds to 40 minutes, a time interval in which the decrease of the signal can be considered linear.

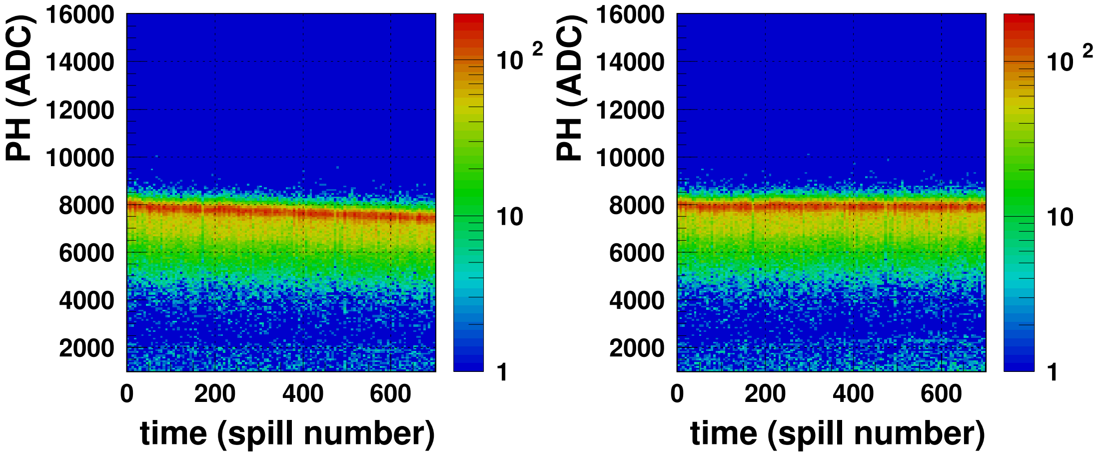

Figure 3.38: A comparison between the PH of the spectrometer channel n.4 (left) before performing the linear approach procedure and (right) after the correction process.

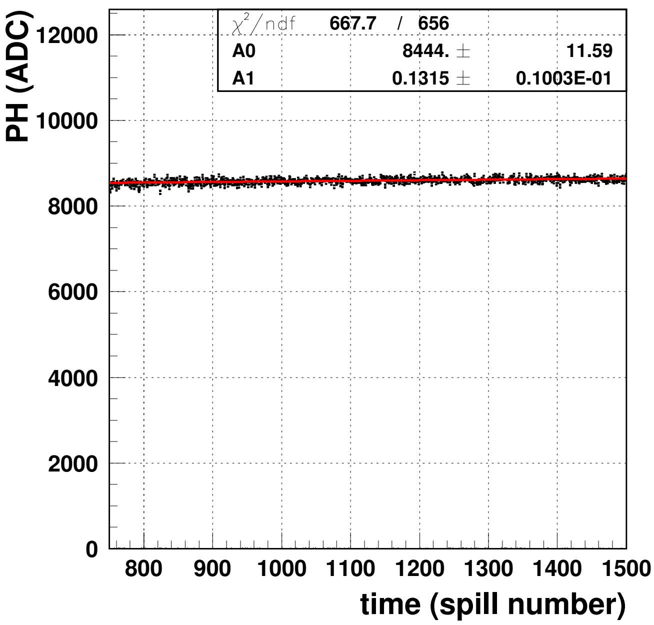

Figure 3.39: An example of the new computed PH trend as a function of time of the Cherenkov detector n.4, in the linear approach procedure; the red line shows the linear fit performed to verify the goodness of the procedure.

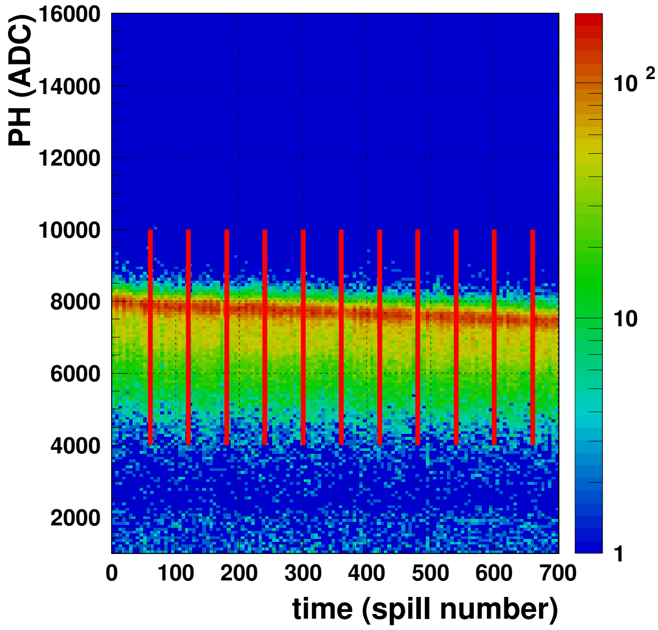

Figure 3.40: An example of the subdivision of a run into segments of 60 spills each (detector n.4).

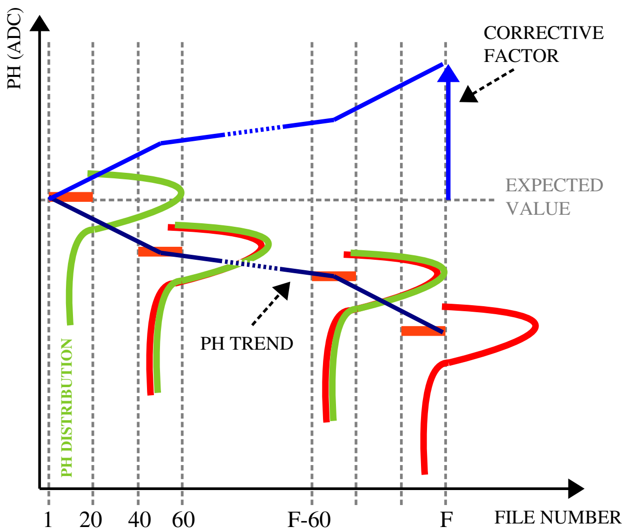

Figure 3.41: A schematic of the segmented approach routine; the algorithm, as in the linear approach, computes the average of the first 20 and of the last 20 files of each 60 files section (red lines), and finds a trend line (dark blue line). The signal decreasing trend is compensated by adding to the raw PH a corrective factor as a function of the corresponding file number (blue line), taking into account the mean PH value of the previous section.

$$PH_{i,corr} = PH_i - [\alpha_i \cdot (\#file_{mod60})] + B_{i,section-1} \quad (3.5)$$

- the analysis subroutine moves to the next segment of 60 files and so on, until all the run files are completely reprocessed.

An example of the results obtained by applying this correction routine is shown in fig. 3.43; fig. 3.44 shows the new computed PH trend. Also in this case the correction procedure manages to rectify the response of the detector.

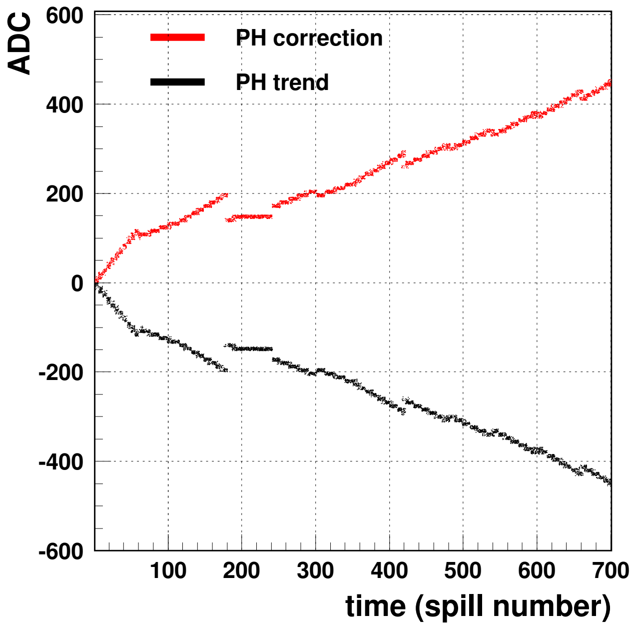

Figure 3.42: An example of the PH trend and the corrective factor as a function of time applied to the Cherenkov detector n.4 in the segmented approach procedure.

Both the procedures show encouraging results in linearising the non-constant response over time of the individual detectors, so they can be used in the data reprocessing; given the lenght of the runs, the second approach has been chosen to reprocess the data.

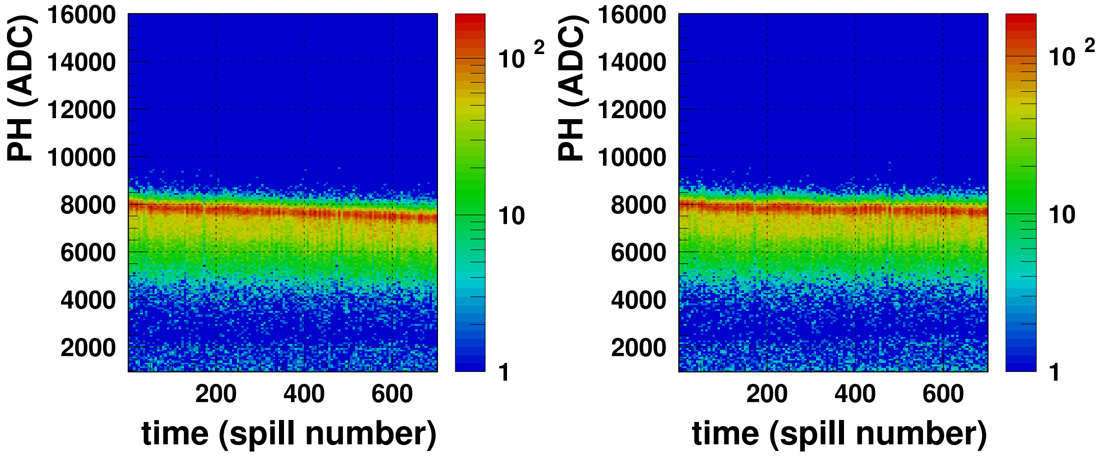

Figure 3.43: A comparison between the PH of the spectrometer channel n.4 (left) before performing the segmented approach procedure and (right) after the correction process.

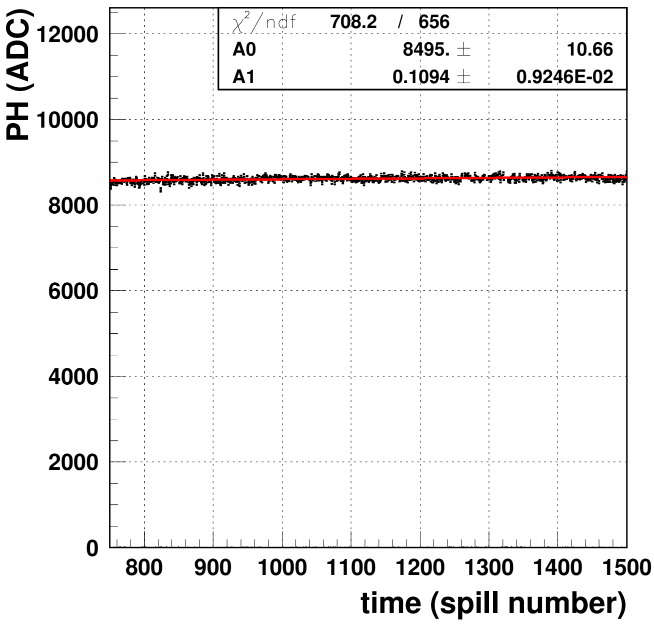

Figure 3.44: An example of the new computed PH trend as a function of time of the Cherenkov detector n.4, in the segmented approach procedure; the red line shows the linear fit performed to verify the goodness of the procedure.

4

DATA ANALYSIS & RESULTS

This chapter will present the experimental results of the beamtest performed by the K_LEVER collaboration. The main goal of the test was to characterize the increase of the electromagnetic interaction probability in a crystalline tungsten sample for an impinging photon in channeling condition.
The interaction process presents two fundamental features: a large energy deposit in the crystal lattice with respect to the amorphous situation, resulting in a smaller amount of the total energy downstream the sample, and a larger number of charged particles after the crystal, due to the reduction of the effective radiation length of the medium (and therefore a larger development of the electromagnetic shower within the lattice). Both the effects can be measured by the experimental setup: a smaller signal in the GAMMA calorimeter with respect to the one of the amorphous condition and the increase of the pulse height of the S3 scintillator immediately after the sample are the evidence of the coherent interaction.
Sec. 4.1 deals with the characterization of the tagged photon beam; then, each crystal is analyzed as a function of the goniometer angular position (and thus of the photon beam misalignment angle), as described in Sec. 4.2. Finally, Sec. 4.3 and Sec. 4.4 present respectively the data analysis performed on the Princeton crystal and on the RAS-ISSP sample and the results, together with the enhancement factor of the forward charged multiplicity in the axial condition with respect to the amorphous one.

4.1 THE TAGGED PHOTON BEAM

The first step of the test focused on the study of the photon beam impinging on the crystalline sample, produced by means of the copper target after the tracking section. The photon beam has been characterized as follows:

- by means of dedicated electron runs (in which the bremsstrahlung target is brought out of the beamline and the bending magnet is switched off), the position of the crystal is determined with respect to the beam and to the silicon detectors; thus, a position cut is made on the beam projection at a z distance corresponding to that of the goniometer. In this way, for each crystalline sample a fiducial area smaller than the size of the crystal can be considered. The position cuts performed on the two crystals are summarized in tab. 4.1;

Crystal	x-pos (cm)	x-cut (cm)	y-pos (cm)	y-cut (cm)	cut size (cm^2)
W(111)	0.80 - 1.80	0.90 - 1.70	0.40 - 1.40	0.50 - 1.30	0.64
W(100)	1.15 - 1.85	1.25 - 1.75	0.60 - 1.30	0.70 - 1.20	0.25

Table 4.1: x and y position cuts applied to the reconstructed crystal projection.

- a selection in the angular distribution at the T2 high resolution silicon telecope (fig. 4.1-4.2) collects only primary 120 GeV electrons with a divergence up to 60 μrad, thus minimizing their incidence angle with respect to the copper bremsstrahlung converter. The outgoing photon is thought to have the same direction of the primary electron, and therefore has a small divergence which is fundamental to collect a statistics large enough of particles entering the crystal in channeling condition;

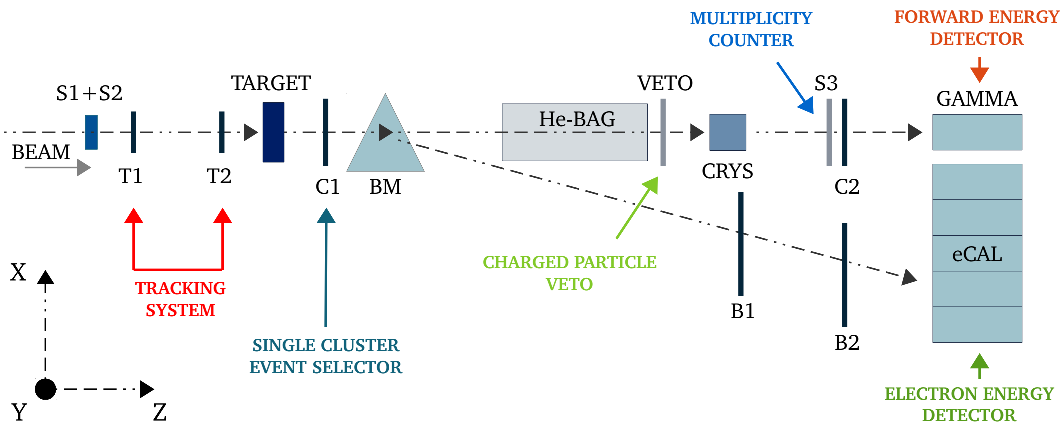

Figure 4.1: The schematic view of the K$_L$EVER setup. The upstream section (the T1 and T2 high resolution silicon detectors) determines the photon track and direction at the crystal position; the S3 scintillator is used as a multiplicity counter, while the GAMMA and the eCAL sides of the spectrometer measure respectively the forward energy spectrum of the secondary particles produced by the photon in the electromagnetic shower inside the crystal (or the energy of the non-interacting photon itself) and the electron energy.

- the cluster distribution of the C1 detector allows to select only single-track events (both in the x and the y direction, fig. 4.3) in order to have a single charged particle (detected by the silicon chamber and steered to the spectrometer) and the corresponding undetected bremsstrahlung photon;

- events with a VETO PH value above a given threshold are rejected (fig. 4.4), to discriminate photons from the background of charged particles (due to photon pair production processes) in the downstream section of the beamline;

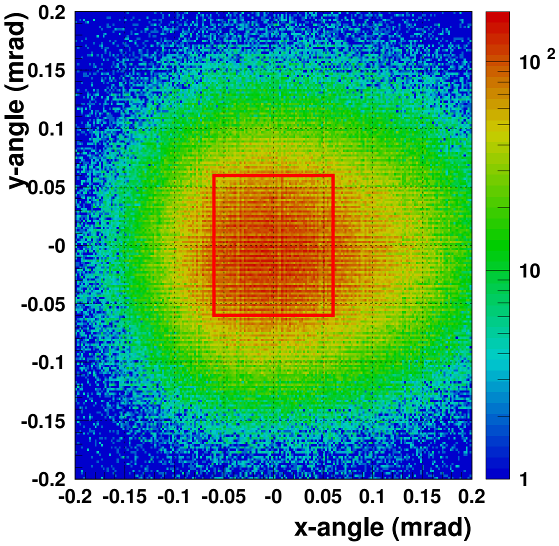

Figure 4.2: The 2D plot of the beam angular distribution at the T2 silicon detector with the divergence cut (red box) to select particles entering the crystal in channeling condition.

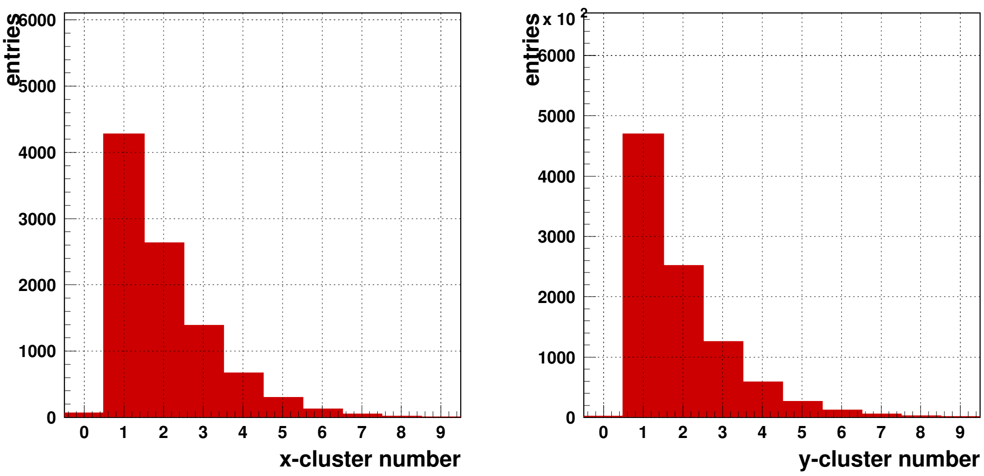

(a) x cluster distribution

(b) y cluster distribution

Figure 4.3: The C1 detector (a) x and (b) y cluster distribution; only single cluster events in both the silicon detectors are considered for the tagged photon beam analysis.

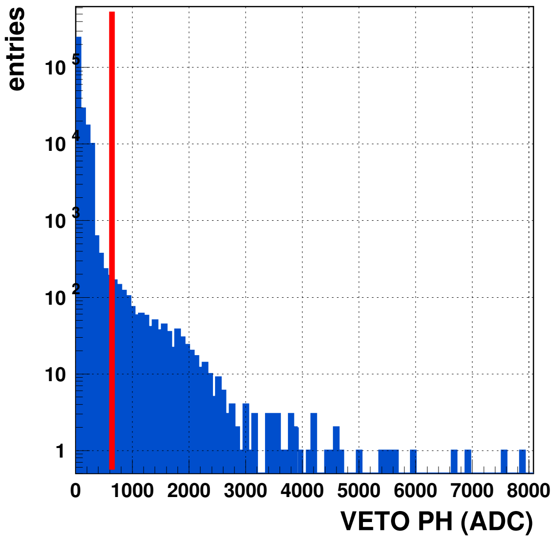

Figure 4.4: The PH distribution of the VETO detector; the red line corresponds to the threshold (700 ADC) used to select events that involved neutral particles along the beamline in the downstream section.

- the total energy of the steered electron is computed as the sum of the calibrated pulse heights of all the eCAL spectrometer channels;
- the total eCAL energy is then summed to the energy measured by the GAMMA calorimeter in order to check if it is equal to 120 GeV, *i.e.* the energy of the primary particle. In order to verify the correct correlation between the two measured energies, the spectra of the detectors are compared in a 2D plot: since the energy of the 120 GeV primary electron impinging on the copper target must be conserved, the (electron, photon) energy points must lay on the region of the plot corresponding to this value, that is a straight line through the values (120 GeV, 0 GeV) and (0 GeV, 120 GeV), as shown in fig. 4.5.

In this way, it is possible to compare the energy of the photon impinging on the crystal "tagging" it with the corresponding electron energy detected by the spectrometer.

4.2 THE CRYSTAL CHARACTERIZATION

The main test goal is to show the increase in the probability of the photon interaction within the tungsten lattice in channeling condition with respect to the amorphous configuration. As described in Chap. 2, a particle crossing a crystalline medium with a small angle relative to the crystal axis and planes direction is induced to interact with it in a coherent way: the effect results in a decrease of the electromagnetic radiation length X_0, so that the probability of interacting with the crystal lattice increases. Thus

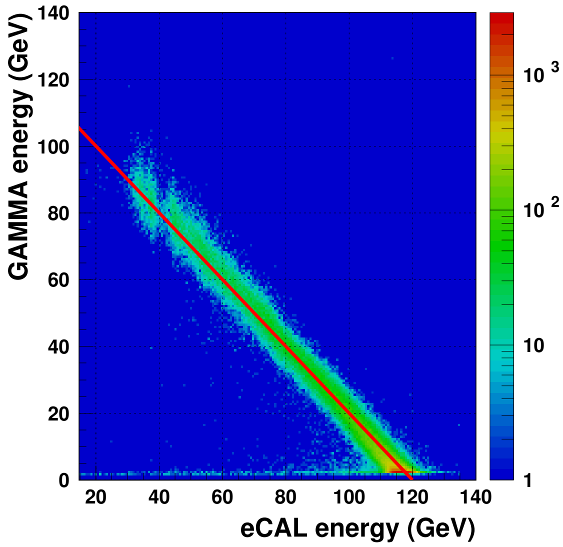

Figure 4.5: The γ-e$^-$ energy correlation. The red line shows the expected total energy correlation (120 GeV); the lack of statistics in the region corresponding to (0, 25) GeV of the eCAL spectrum is due to the electron spectrometer energy coverage limits. This energy range cannot be measured, thus the related events are placed along the 0 GeV axis of the electron spectrum.

in the case of a high energy photon, the pair production probability increases with respect to the amorphous case: the electromagnetic shower started by the photon will therefore produce a larger number of secondary particles, with an energy smaller than the one of the amorphous interaction, as shown in fig. 4.6.

According to the experimental layout, the difference of the effects between the amorphous and the axial configuration can be observed in two ways, one complementary to the other:

- the coherent interaction of the photon in the crystal results in an electromagnetic shower depositing in the sample a larger amount of energy than in the amorphous case, due to the increase in the electromagnetic interaction probability. The secondary particles that reach the GAMMA calorimeter will therefore have a smaller energy, and the detector will measure a smaller total forward energy then the one obtained in the amorphous case;

- on the other hand, in the channeling configuration the reduction of the radiation length of the crystal produces a larger number of secondary charged particles than the amorphous case. The PH of the S3 scintillator depends directly on the number of charged particles that cross it: thus, the increase of the multiplicity of secondary particles, leaving the crystal, results in the increase of the total PH of the detector just behind the sample.

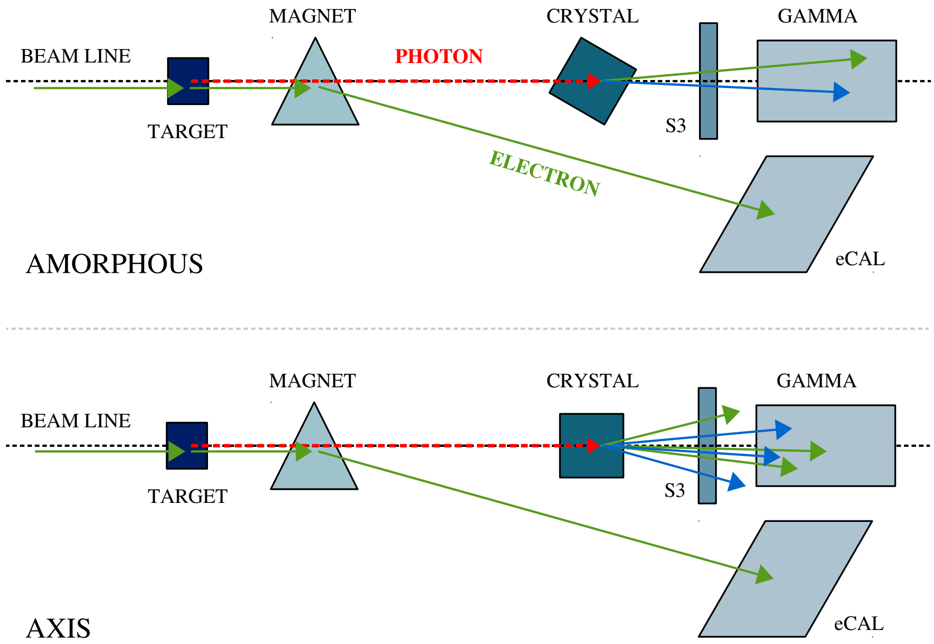

Figure 4.6: A schematic view of the amorphous (top) and the coherent (bottom) interaction in the experimental setup; the effect depends on the impinging particle angle with respect to the crystal plane: in the amorphous case the electromagnetic shower develops according to the characteristic X_0 radiation length of the medium. Given the reduced thickness of the sample, the number of produced secondary particles is smaller than the axial case, but they carry a larger energy. The signature of these events is therefore a reduced pulse height of the S3 scintillator, with a larger energy deposit in the GAMMA calorimeter. On the other hand, in the axial case the shortening of the radiation length (and therefore the increase in the photon probability to interact and to deposit a larger amount of energy in the crystal) leads to a larger number of secondary particles in the shower, each one with a smaller energy: the S3 scintillator thus detects a larger PH and the GAMMA calorimeter measures a smaller forward energy.

In order to verify the effective presence of coherent effects in the photon/crystal interaction and the reduction of the effective crystal radiation length X_0 in channeling condition, each of the crystalline samples is characterized as follows:

- the spectrum measured by the GAMMA calorimeter is compared to the one obtained by the eCAL spectrometer. A decrease of the photon energy deposit inside the GAMMA calorimeter (and thus an increase in the energy loss inside the crystal sample) shows the effective coherent interaction of the photon within the crystal lattice, as the Cherenkov detector is reached by secondary particles of lower energy compared to those of the amorphous interaction;
- furthermore, the S3 plastic scintillator PH distribution is studied as a function of the GAMMA and the eCAL energy, to verify the expected increase in its ADC value due to the enhancement of the charged pair production in the axial condition;
- the S3 detector pulse height is studied also as a function of the goniometer misalignment angle (and thus the angle of the impinging photon); the charged particles multiplicity in the aligned case is larger than the one obtained in the amorphous condition, due to the decrease of the crystal electromagnetic radiation length, and an increase of its PH value is expected as the crystal approaches the axial condition;
- the trend of the multiplicity enhancement is characterized as a function of the goniometer angular position and the energy detected by the electromagnetic spectrometer;
- finally, the multiplicity enhancement factor in the S3 PH is computed in the amorphous and the axial condition as a function of the photon energy.

4.3 THE PRINCETON SAMPLE

The W(111) tungsten sample from Princeton Scientific is a cubic commercial crystal of considerable thickness (10×10×10 mm^3, ≈2.86 X_0) but with lower quality crystalline characteristics compared to the Russian sample. However, the possibility of producing a crystal of this kind in an industrialized way and on a large scale, combined with the non-trivial thickness, makes this sample a possible candidate for its use in the K_LEVER final setup, in particular as TAX photon converter, and in the development of the SAC detector (the Small Angle Calorimeter described in Sec. 1.2.10). The modular structure of the SAC requires tungsten crystals made according to a standardized procedure, combining acceptable crystalline features with an appropriate thickness, in order to satisfy the detector requirements.
The crystal test starts with the positioning and the alignment of the sample on the beamline, as described in Sec. 3.4; after that, several data runs are acquired according to various angular positions of the goniometer, in order to simulate different angles of

incidence of the photon beam with respect to the crystal. The angular scan performed in the W(111) test is summarized in tab. 4.2. Fig. 4.7 shows a picture and a schematic view of the W(111) sample, while fig. 4.8 shows the crystal beam shadow and the position cuts made during the analysis procedure.

(a) A picture of the W(111) sample

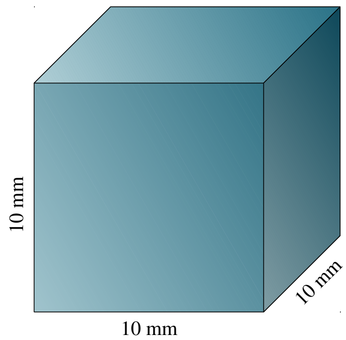

(b) The W(111) schematic

Figure 4.7: (a) A picture of the W(111) Princeton sample in its holder and (b) a schematic view of the crystal.

step scan	angular position (mrad)
1	0 (axis)
2	2.5
3	5.0
4	7.5
5	12.5
6	amorphous

Table 4.2: The W(111) test angular scan steps.

4.3.1 FORWARD ENERGY SPECTRUM

Fig. 4.9 shows the GAMMA energy spectrum in comparison with the total energy detected by the eCAL spectrometer, in logarithmic scale, in the amorphous (left side) and the axial (right side) condition. The two plots differ since there is an evident decrease in the energy detected by the GAMMA calorimeter as the photon energy deposit in the crystal lattice increases in the axial case with respect to the amorphous one: the photon interacts with the crystalline lattice in a coherent way, and therefore it crosses the sample producing a more extensive and populated electromagnetic shower. Due to the decrease of the EM radiation length, particles of smaller output energy are generated as final products, and for this reason the GAMMA detector pulse height decreases.

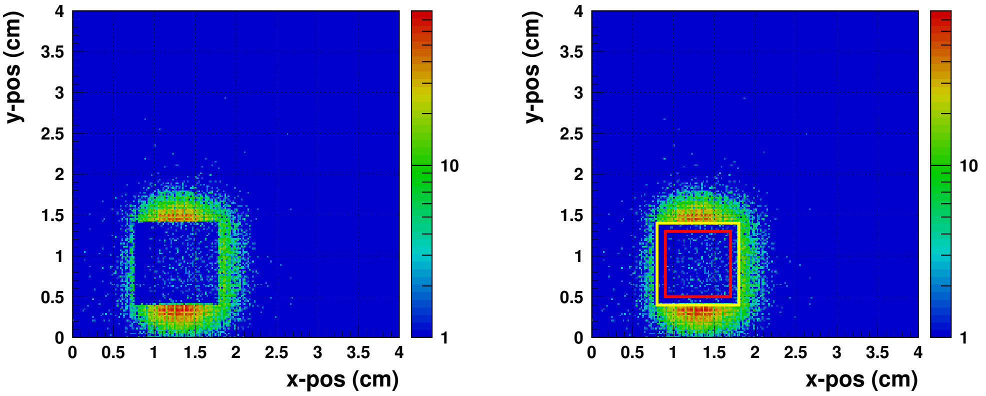

(a) The W(111) crystal shadow **(b)** The position cut

Figure 4.8: (a) The W(111) crystal shadow at the C2 detector, obtained by imposing a single cluster in the x and the y cluster distribution of the C2 silicon detector and (b) the position selection (red box) made at the reconstructed goniometer distance; the yellow box shows the crystal position.

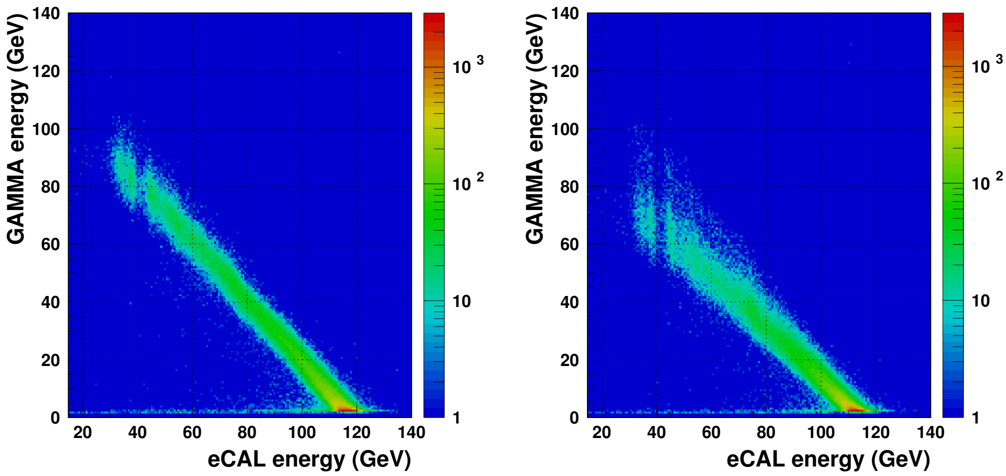

(a) Amorphous **(b)** Axis

Figure 4.9: E_γ distribution of the GAMMA calorimeter versus the E_{eCAL} of the electromagnetic spectrometer in (a) the amorphous case and (b) in the axial case; in the axial case there is an evident decrease of the energy measured by the GAMMA calorimeter compared to the amorphous case.

To highlight the increase in the interaction probability of the photon in the crystal lattice in channeling condition, a plot is filled with a selection on the cluster number in the C2 silicon detector, positioned after the S3 scintillator, both located after the crystal. Both in the amorphous and in the axial condition, events that do not have clusters in the x and the y directions and those that have at least 5 clusters in both the detector tiles are compared to the total event population, as shown in fig. 4.10. In the amorphous case, both the selected groups are located in the same region of the plot (the one corresponding to the energy conservation of the primary beam particle), observing only a slight forward energy decrease for events with more than 5 clusters. Since the photon crosses an unordered structure, its interaction with the sample (and thus the energy loss) is ruled by the amorphous interaction: given the thickness of the crystal, only a little amount of energy is released in the lattice and the electromagnetic shower is developed only in a partial way, so that the GAMMA calorimeter measures a transmitted energy comparable to that of the non-interacting photon.
On the other hand, in channeling condition the energy lost by the photon in the crystal is larger the more energetic the impinging photon is, so that the two groups separate much more clearly the larger the impinging photon energy is.

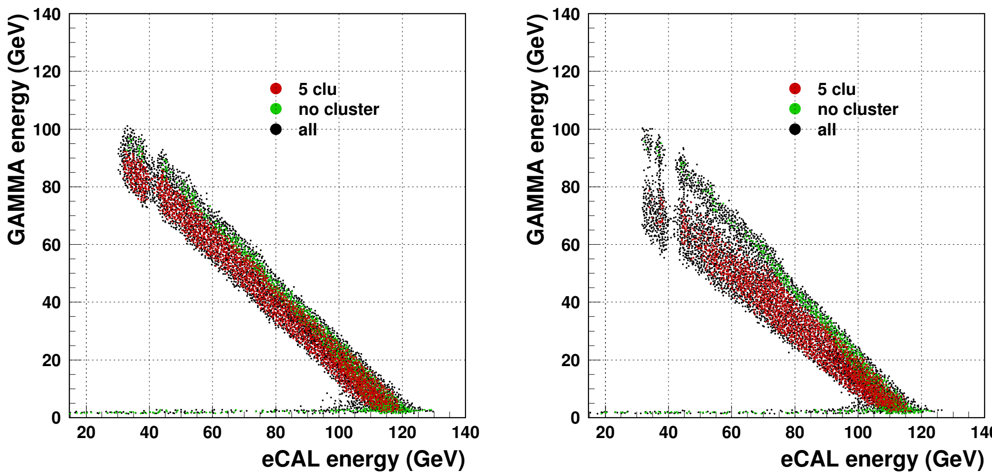

(a) Amorphous **(b)** Axis

Figure 4.10: E_γ versus E_{eCAL} for events in (a) the amorphous case and (b) in the axial case, selected as a function of the corresponding number of clusters (in both the x and y direction) in the C2 detector; the black points refer to all the events, while the red and the green ones correspond respectively to ≥ 5 clusters and zero cluster events.

Finally, the mean energy of the GAMMA calorimeter as a function of the electron spectrum for different crystal angular positions is studied, as shown in fig. 4.11. The GAMMA spectrum mean energy gets smaller as the misalignment angle approaches the axial condition, due to the larger energy deposit in the crystal lattice. The effect does not present substantial differences for angles smaller than 5 mrad. Once again, the decrease in the average signal detected by the GAMMA calorimeter for an electron energy of about 20 GeV is due to the lack of statistics of the electron values in this range, due to the size of the spectrometer.

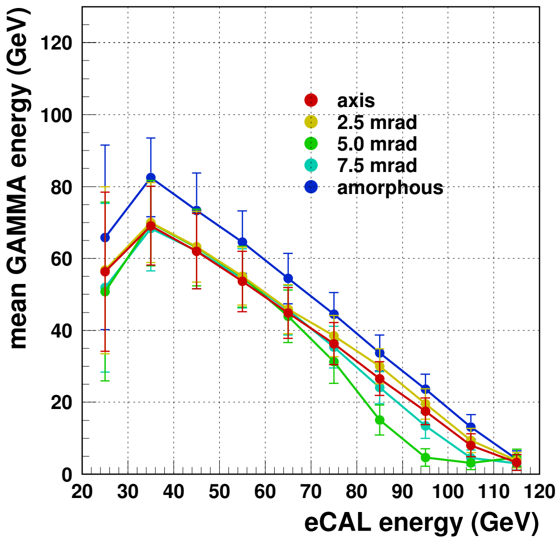

Figure 4.11: The GAMMA energy distribution as a function of the eCAL spectrum and the crystal misalignment angle. The GAMMA spectrum mean energy gets smaller as the misalignment angle approaches the axial condition, due to a larger energy deposit in the crystal lattice.

4.3.2 MULTIPLICITY ENHANCEMENT

This section describes the study of the pulse height of the S3 scintillator as a function of the forward energy measured by the GAMMA calorimeter, of the spectrum of the steered electron in the eCAL spectrometer and of the crystal angle with respect to the direction of the impinging photon beam. The effect expected in the scintillator is the increase in the values of its PH as the crystal approaches the channeling condition. Fig. 4.12 shows the S3 PH distribution as a function of the spectrometer energy, both in the amorphous and the axial case. The multiplicity enhancement effect measured by the S3 detector is shown in fig. 4.13: as the misalignment angle moves from the amorphous to the axial condition, the S3 PH distribution maximum value increases; the trend becomes constant for angle smaller than 5 mrad.
The PH distribution of the S3 detector is also compared with the energy measured by the GAMMA calorimeter and with the energy measured by the spectrometer. As shown in fig. 4.14, the scintillator PH clearly increases from the amorphous to the axial case.

The S3 signal trend is then characterized as a function of the crystal misalignment angle, as shown in fig. 4.15. The plot presents the mean PH values of the detector

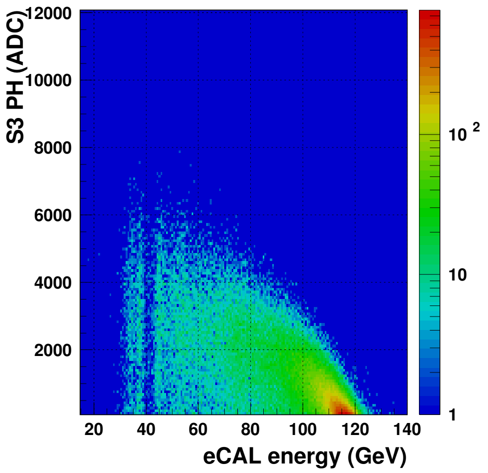

(a) Amorphous

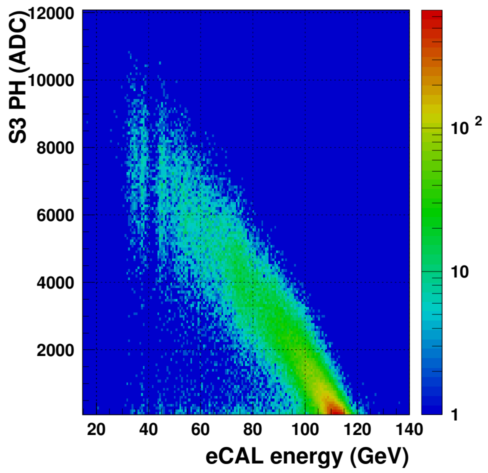

(b) Axis

Figure 4.12: The pulse height distribution of the S3 scintillator versus the spectrometer energy in (a) the amorphous case and (b) in the axial case; the PH values increase in the axial case with respect to the amorphous one.

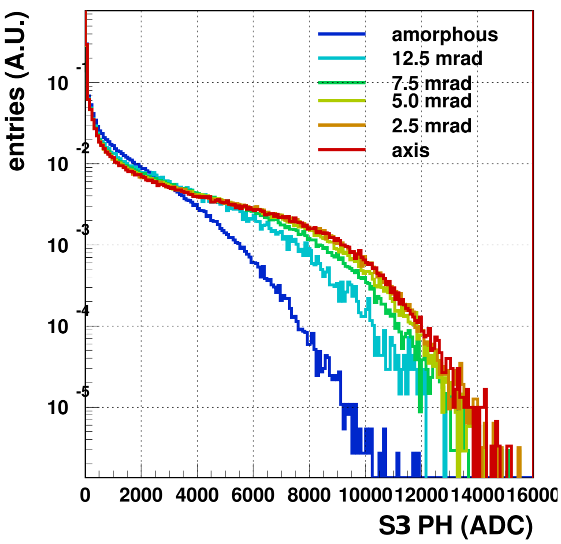

Figure 4.13: The S3 PH distribution as a function of the goniometer position. The PH distribution maximum value increases as the misalignment angle moves from the amorphous to the axial condition: below 5 mrad, the effect does not change as a function of the angle and the distributions overlap with the axial one.

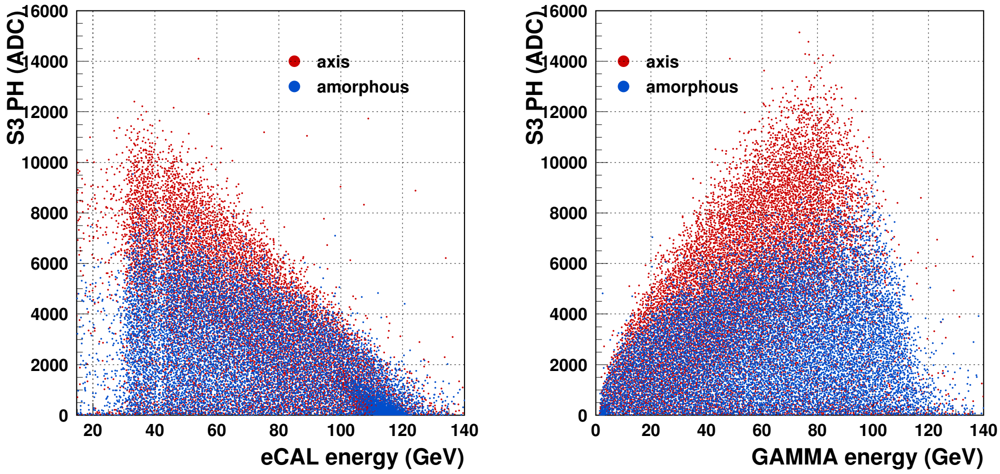

(a) S3 PH *vs.* eCAL **(b)** S3 PH *vs.* GAMMA

Figure 4.14: The S3 PH distribution as a function of (a) the eCAL spectrum and (b) the GAMMA spectrum in the amorphous case (blue dots) and in the axial case (red ones): it is clear the increase in the multiplicity detected by the S3 scintillator in the case in which the photon impinges on the crystal in channeling condition with respect to the amorphous one.

downstream the crystal as a function of the eCAL spectrum according to the different angular positions of the goniometer. The aligned condition increases the forward charged multiplicity due to the photon interaction by about a factor of 2 at high photon energies (80 - 100 GeV), and the effect is clearly visible for a wide angular range with respect to the amorphous condition.

The final test of the multiplicity increase due to the photon coherent interaction inside the crystal is given computing the enhancement factor (*i.e.* the ratio of the mean PHs) in the axial condition with respect to the amorphous one. In this way, it is possible to compute the increase of the interaction probability of the impinging photon, and therefore the effective reduction of the medium radiation length X_0 due to the coherent effects involved in the axial condition. As shown in fig. 4.16, the S3 signal is amplified more than twice when the energy of the impinging photon exceeds 80 GeV. In terms of the interaction between the photon and the crystal, this approximately corresponds to one extra shower generation in the crystal lattice in the aligned case with respect to the amorphous one.

A rough estimation of the effective decrease of the radiation length can be obtained, thus giving an extimation of the virtual increase in the physical crystal length "seen" by the photon. The mean longitudinal profile of the energy deposit by an electromagnetic shower is usually described by a gamma distribution [124]:

$$\frac{dE}{dt} = E_0 b \cdot \frac{(bt)^{a-1} e^{-bt}}{\Gamma(a)} \tag{4.1}$$

where $t = x/X_0$ is the distance crossed by the particle, measured in units of radiation length. b is assumed to be ≈0.5, and one can find the value of a from $2(a-1) = \ln(y) + b$, where $y = E_\gamma/E_c$ is the energy of the primary photon ($E_\gamma = 80$ GeV) as a function of the critical energy ($E_c = 1.8$ MeV in W). The multiplicity N of charged particles crossing the S3 detector may be considered proportional to the energy deposit dE/dt, both in the amorphous and in the axial case [125]. Considering ≥80 GeV photons, the enhancement multiplicity factor of fig. 4.16 is given by:

$$2 = \frac{N_{axis}}{N_{amorph}} \propto \frac{t_2^{a-1} e^{-bt_2}}{t_1^{a-1} e^{-bt_1}} \tag{4.2}$$

t_2 is the distance in the axial case, while $t_1 = 10$ mm$/3.5$ mm $= 2.86$ in the amorphous one. Imposing $t_2 = \beta \cdot t_1$ and solving eq. 4.2 in the β parameter, one can obtain:

$$\beta = \frac{t_2}{t_1} = 1.2 \tag{4.3}$$

that is, a virtual 2 mm thickness is added to the tungsten crystal, due to the coherent interaction with the high energy photon: in the axial case, the sample is then equal to 3.4 X_0, *i.e.* X_0 is virtually reduced by 20%.

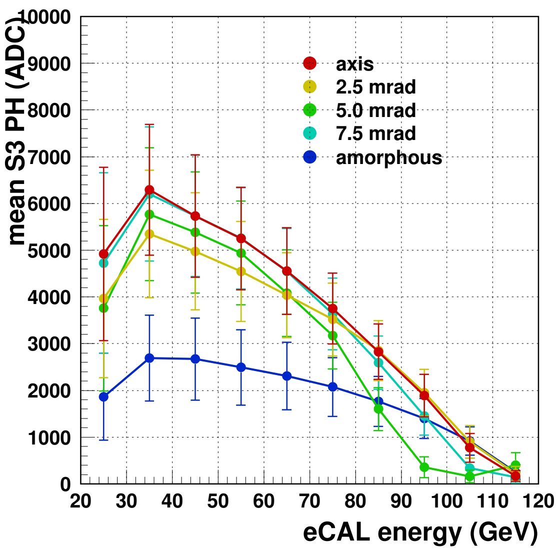

Figure 4.15: The S3 PH distribution as a function of the eCAL spectrum and the crystal misalignment angle. The PH distribution reaches larger values as the misalignment angle moves from the amorphous to the axial condition, increasing the forward charged multiplicity by about a factor of 2 at high photon energies (E_γ ≥80 GeV).

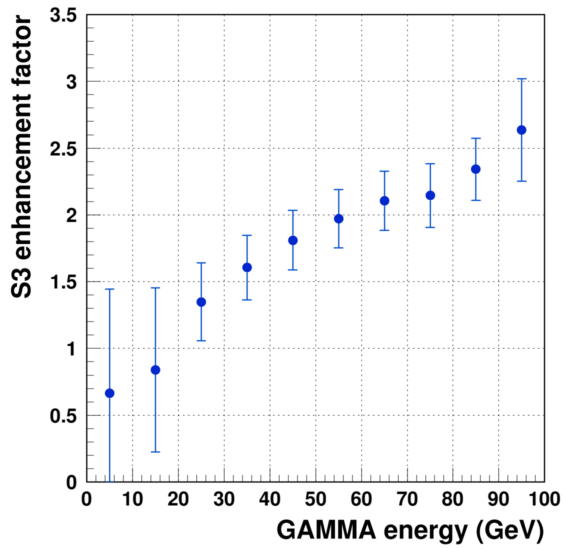

Figure 4.16: The charged multiplicity enhancement factor of the axial condition with respect to the amorphous one (computed as the ratio of the S3 mean PH values in the two configurations), as a function of the photon energy; it is possible to observe that the charged multiplicity is enhanced by a factor ≥2 for $E_\gamma \approx 80$ GeV.

4.4 THE RAS-ISSP SAMPLE

The W(100) RAS ISSP crystal is a high purity and high quality 2.2 mm thick tungsten crystalline sample, with an irregular section and a smaller area than the one of the Princeton sample (as shown in fig. 4.17). Although the use of crystals of this type is not foreseen in the final K_LEVER experimental setup, the W(100) sample was tested to obtain useful data for the Monte Carlo simulations for the SAC and the TAX designs. The tests performed on the W(100) sample are the same of the Princeton crystal, with a difference concerning the angular range and the number of steps of the measurement as a function of the photon angle, as shown in tab. 4.3. A picture and a schematic view of the RAS sample are presented in fig. 4.17, while the crystal beam shadow and the position cuts are plotted in fig. 4.18.

4.4.1 FORWARD ENERGY SPECTRUM

Once the RAS-ISSP crystal has been aligned to the beam, several measurements have been performed as a function of the goniometer angle, moving from the axial position towards the amorphous one.
The small crystal thickness (≈0.63 X_0) does not allow to identify clearly the presence of coherent phenomena in the photon/sample interaction just using the transmitted spectrum. Even the average value of the GAMMA calorimeter as a function of the electron energy according to the crystal misalignment angle does not help (fig. 4.19).

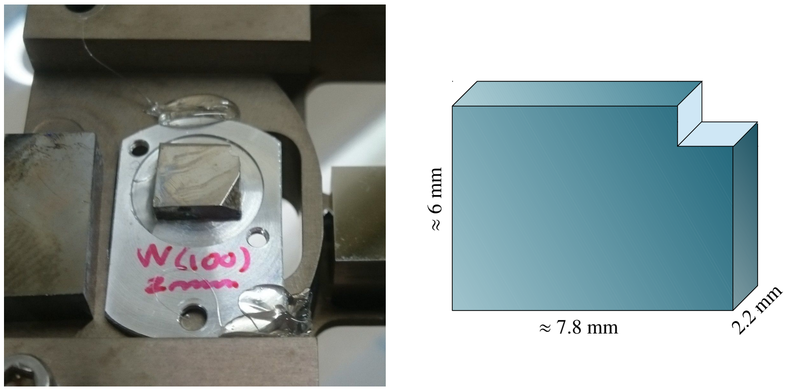

(a) A picture of the W(100) sample **(b)** The W(100) schematic

Figure 4.17: (a) A picture of the W(100) RAS ISSP sample in its holder and (b) a schematic view of the crystal.

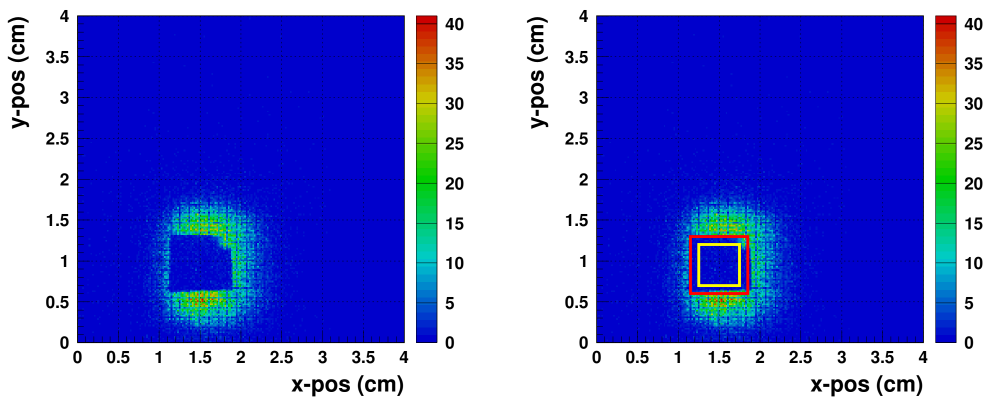

(a) The W(100) crystal shadow **(b)** The position cut

Figure 4.18: (a) The W(100) crystal shadow at the C2 detector and (b) the position cut (yellow box); the red box shows the crystal position with respect to the beam.

step scan	angular position (mrad)
1	0 (axis)
2	0.5
3	1.0
4	1.5
5	2.5
6	5.0
7	amorphous

Table 4.3: The W(100) test angular scan steps.

The difference in the photon energy loss within the crystalline lattice in the amorphous and the axial condition can be only slightly noticed: almost all the secondary particles produced in the coherent interaction exit the crystal and reach the downstream detector, inducing a signal comparable to the one of the non-interacting photon.

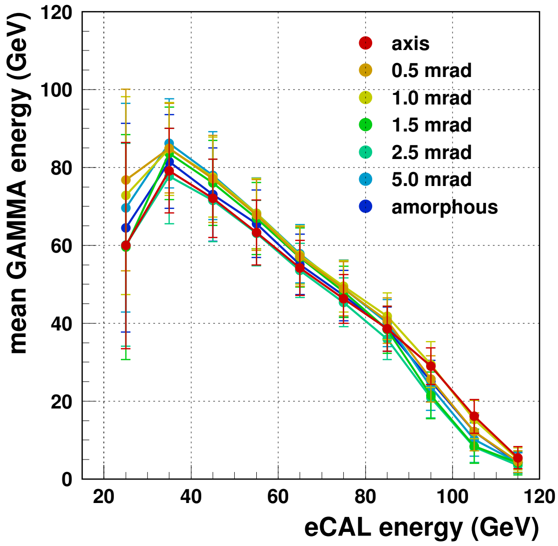

Figure 4.19: The GAMMA energy distribution as a function of the eCAL spectrum and the crystal misalignment angle for the W(100) sample. Given the reduced W(100) thickness with respect to the W(111) sample, the decrease in the radiation detected by the GAMMA calorimeter is barely visible, since almost all the secondary particles produced in the coherent interaction exit the crystal and reach the downstream detector.

4.4.2 MULTIPLICITY ENHANCEMENT

As in the Princeton test, the S3 scintillator PH distribution was studied as a function of the energy measured by the spectrometer (fig. 4.20-4.21) and the crystal angular position (fig. 4.22). The expected effect in the RAS - ISSP sample will be a smaller S3 PH value in all the configurations compared to the thicker Princeton crystal, due to the reduced EM shower development (and thus a limited pair-production process).

The increase of the PH value as a function of the spectrum measured by GAMMA and by the eCAL spectrometer is clearly visible in the axial condition with respect to the misaligned configuration. Moreover, the S3 PH maximum value distribution as a function of the goniometer angle increases approaching the axial condition, although being lower than those observed for the Princeton sample. The effect does not change only for a misalignment angle smaller than 1 mrad: the sample angular acceptance is therefore smaller than the one of the commercial crystal.

The trend of the mean S3 PH value has been compared with the electron energy spec-

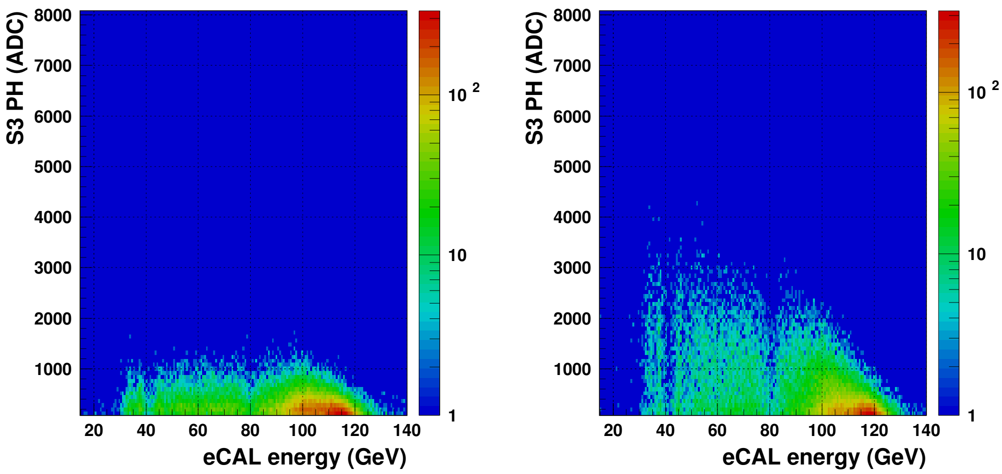

(a) Amorphous **(b)** Axis

Figure 4.20: The pulse height distribution of the S3 scintillator versus the spectrometer energy in (a) the amorphous case and (b) in the axial case; also in the W(100) sample the S3 signal increases in the axial case with respect to the amorphous one.

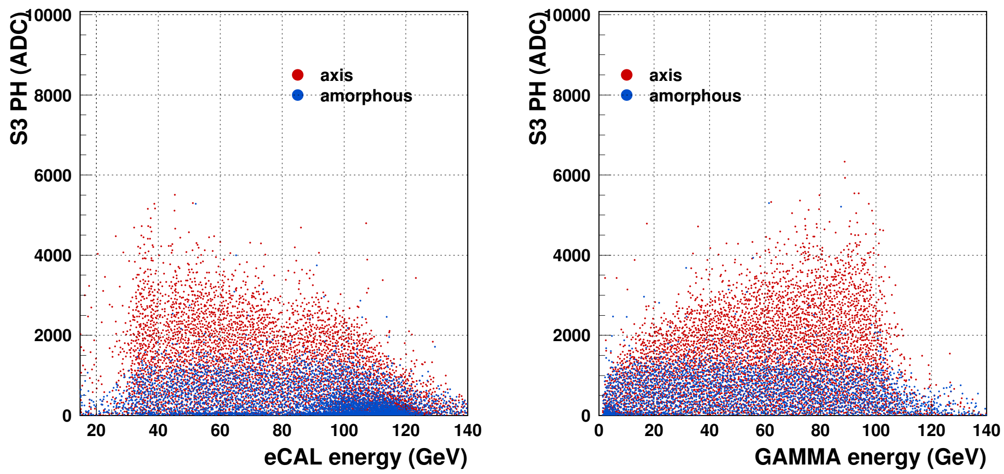

(a) S3 PH *vs.* eCAL **(b)** S3 PH *vs.* GAMMA

Figure 4.21: The S3 PH distribution as a function of (a) the eCAL spectrum and (b) the GAMMA spectrum in the amorphous case (blue dots) and in the axial case (red ones) for the W(100) sample: also in this test the S3 scintillator PH increases in the case in which the photon impinges on the crystal in channeling condition with respect to the amorphous one.

trum measured by the eCAL spectrometer, as a function of the angular position of the crystal. In fig. 4.23 the mean value of the S3 signal varies significantly according to the angle, and a large enhancement ratio (up to a factor 4 for ≥80 GeV photons) may be obtained comparing the amorphous and the axial cases. The process becomes independent from the misalignment angle only below 1 mrad. Lastly, in order to show the coherent effects dependence with respect to the photon energy, the mean S3 PH value is compared as a function of the misalignment angle for several photon energy values (fig. 4.24), highlighting a larger energy loss in the crystal lattice the higher the energy of the impinging photon is.
Also for the RAS-ISSP crystal the charge multiplicity enhancement factor of the axial condition with respect to the amorphous case is computed as a function of the energy of the photon impinging on the sample (fig. 4.25). A huge increase in the multiplicity downstream of the crystal is evident; however, it is not possible to roughly estimate the effective radiation length, as in the other crystal, since the model foresees a medium thick enough to allow a partial electromagnetic shower development. The analysis results, however, provide useful information on the energy and the angular dependence of the coherent pair production process, that will be used for the Monte Carlo simulation of the K_LEVER crystalline elements (the TAX converter and the SAC calorimeter) foreseen in its final layout.

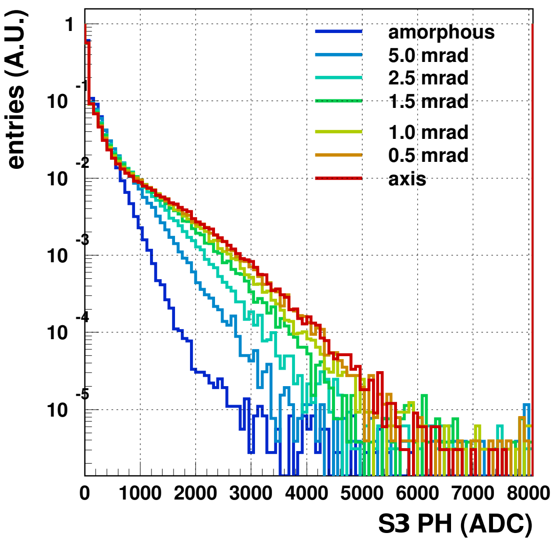

Figure 4.22: The S3 PH distribution as a function of the goniometer position in the W(100) test. The PH distribution gets larger maximum values as the misalignment angle moves from the amorphous to the axial condition; however, in this case the effect becomes constant with respect to the goniometer angular position only below 1 mrad.

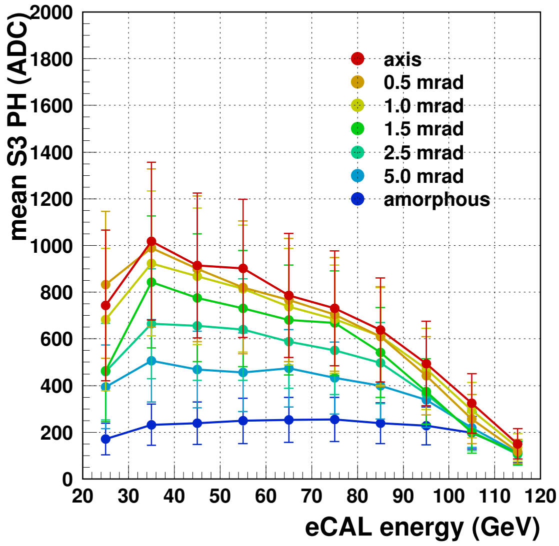

Figure 4.23: The S3 PH distribution as a function of the eCAL spectrum and the crystal misalignment angle in the W(100) test. Unlike the effect seen in the Princeton sample, the multiplicity increase detected by S3 varies clearly according to the angular position of the crystal. A much larger enhancement factor is reached comparing the amorphous and the axial cases (up to a factor 6 for a high energy photon). The effect does not change only for angles smaller than ≈1 mrad, thus the acceptance of the coherent effect is smaller than the one of the thick sample.

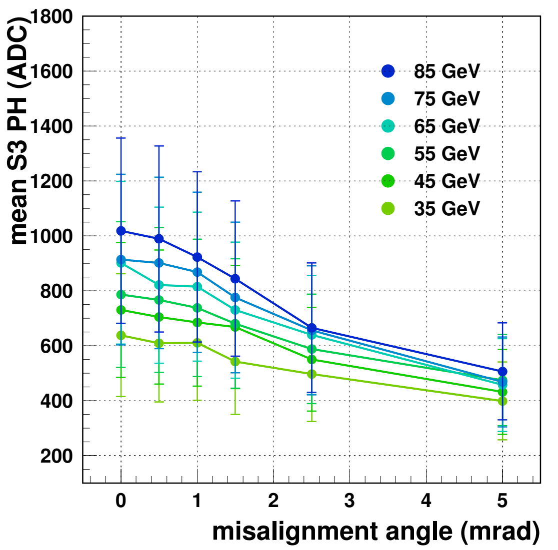

Figure 4.24: The S3 mean PH distribution as a function of the crystal misalignment angle, for several E_{γ} values for the RAS-ISSP sample. The increase of the S3 signal approaching the axial condition reaches larger values the higher the photon energy is, thus highlighting the proportionality between the energy of the impinging photon and the energy loss in the crystal lattice, for the same angle of incidence.

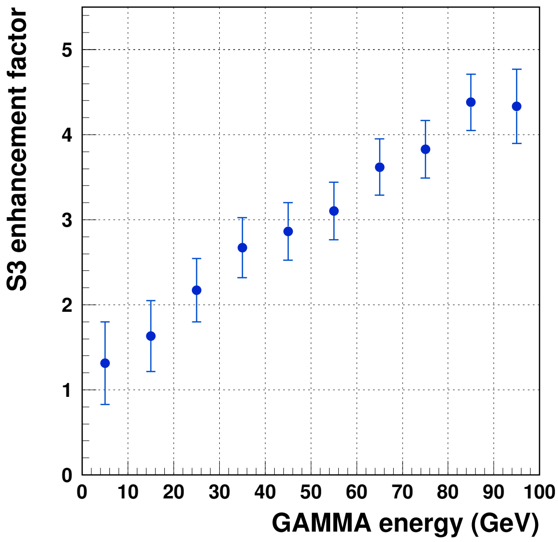

Figure 4.25: The charged multiplicity enhancement factor in the axial condition with respect to the amorphous configuration, as a function of the photon energy for the RAS-ISSP sample. A clear increase in the charge multiplicity enhancement measured by the S3 detector is evident; most of the secondary particles produced by the coherent interaction of the photon do not stop inside the crystal and arrive in the detector, considerably increasing its PH values.

CONCLUSIONS

The K_LEVER collaboration is investigating the possibility to measure the $K_L \rightarrow \pi^0\nu\bar{\nu}$ branching ratio, that is, between all the observables in the quark-flavor sector, the most sensitive to a possible new physics scenario beyond the Standard Model. The main goal of the experimental group is to reach a sensitivity of about 60 $K_L \rightarrow \pi^0\nu\bar{\nu}$ decay events in five years of data taking, by means of a high energy neutral kaon beam ($\approx$40 GeV/c of average momentum) generated by the SPS primary proton beam.
The neutral decay signature is rather simple: two correlated photons due to the pion decay, and nothing else. However, the two particles must be recognized in the huge background induced by the high energy boosted neutral beam. For these reasons, K_LEVER aims to include in its experimental layout the challenging use of tungsten crystals in channeling condition, in order to exploit the effects induced by the coherent interaction of photons with the crystal lattice.
In this framework, a preliminary beamtest was performed at the CERN-SPS North Area that represents the heart of this thesis work. The beamtest (which took place in August 2018) primary goal was the characterization of a compact tungsten crystalline converter with a variable sensitivity with respect to the energy of an impinging photon, thus verifying its future use in the K_LEVER very upstream TAX beam collimator, to efficiently convert high-energy beam photons into charged leptonic pairs minimizing the scattering of the beam hadronic component, and in the SAC, which must reject high energy photons between the foreseen intense neutral beam background.
By means of a high-energy (up to 120 GeV) tagged photon beam, two crystalline samples (respectively 10 mm and 2.2 mm thick, produced by Princeton Scentific and RAS - ISSP) have been characterized.
To measure the increased interaction probability of the photon beam impinging on the samples and the increase in the output charged particle multiplicity in the channeling condition with respect to the amorphous one, the experimental setup was based on a high resolution tracking system (consisting of two silicon microstrip detectors), a bremsstrahlung target, a bending magnet, a micrometric goniometric system, a multiplicity counter plastic scintillator and a multichannel Cherenkov spectrometer, along with several secondary detectors.
In order to accurately characterize the beam features, a preliminary study was performed without the target and the crystals on the beam, acquiring runs with beams of different energy and with or without the magnet deflecting field. At the same time, the alignment via software allowed to obtain the particle input angles, and reconstruct their trajectory, correcting any relative shifts between the detectors in the plane perpendicular to the beam direction.
Each Cherenkov detector has been calibrated several times during the data taking, us-

ing dedicated electron runs with different energies. Each sample has been precisely positioned and oriented with respect to the photon beam by means of a high resolution goniometer, remotely controlled by the DAQ. The alignment procedure consisted of a laser-based coarse pre-alignment, to position each sample with respect to the beamline, and a fine crystal alignment, by means of a position scan of the goniometric system.
Because of the non perfect performance of some of the spectrometer detectors during the data taking, the collected data needed a offline non trivial analysis, performed after the end of the beamtest at the INSULab Laboratory of the Insubria University.
The interaction between the photon and the crystal has been characterized in terms of the photon energy (measured by means of the steered electron energy in the spectrometer), the goniometer position angle and the pulse height of the scintillator detector positioned immediately after the sample.
The effective presence of a coherent interaction process in the axial configuration was evinced by observing in the neutral beamline calorimeter a signal smaller than the one obtained in the amorphous case, combined with an increase of the pulse height measured by the scintillator detector: the two effects demonstrated a larger energy deposit in the crystal lattice and a larger number of produced secondary charged particles, showing the reduction of the "effective" radiation length of the medium and therefore the larger development of the electromagnetic shower within the crystalline sample.
Finally, the multiplicity enhancement factor (*i.e.* the ratio of the scintillator mean pulse height values in the axial and the amorphous condition) for both the crystals was computed: in the case of the 10 mm thick Princeton sample, for a photon beam of energy $\geq$80 GeV the downstream charged multiplicity is enhanced by a factor of 2, corresponding to a reduction of the effective tungsten radiation length of 20%. On the other hand, the RAS-ISSP sample analysis provided useful information on the angular dependence of the coherent pair production, which will be used for the Monte Carlo simulations of the K_LEVER layout.
The beamtest performed was the very first step to test the use of crystalline components in the K_LEVER experiment, and the results were confined to a few essential points for several reasons:

- the reduced number of samples to be tested;
- the two samples thicknesses and their crystalline features, very different one from the other;
- the spectrometer limited coverage of the electron energy range;
- the limited performance of some of the setup detectors.

An additional analysis work can be performed further optimizing the offline data correction routine, in order to linearize each detector response as a function of the overall data taking period, and not just of the single runs. On the other hand, a future feasibility test may use several crystal samples of variable thickness with comparable crystalline features, in order to study the coherent effects induced by the crystalline lattice as a function of the sample thickness crossed by the impinging photon, along with a spectrometer able to adequately cover the steered electron full energy range, to determine precisely the energy of the tagged photon beam. The encouraging results, however, suggest to continue with the K_LEVER R&D on the possibility of using crystalline materials for the final experiment.

LIST OF ACRONYMS

ADC Analog to Digital Converter
AFC Active Final Collimator
APD Avalanche PhotoDiode
ASCII American Standard Code for Information Interchange
ASIC Application-Specific Integrated Circuit

BM Bending Magnet
BR Branching Ratio

CEDAR ChErenkov DifferentiAl counteR
CERN European Organization for Nuclear Research
CKM matrix Cabibbo-Kobayashi-Maskawa matrix
CP violation Charge-Parity violation
CPV Charged Particle Veto

DAQ Data AcQuisition system

Ecal Electromagnetic calorimeter
EM ElectroMagnetic

FCC Future Circular Collider
FCNC Flavour-Changing Neutral Currents
FS Forward Spectrometer
FV Fiducial Volume

GIM mechanism Glashow-Iliopoulos-Majani mechanism
GEANT4 for GEometry ANd Tracking

HL-LHC High-Luminosity LHC

IHEP Institute of High Energy Physics

J-PARC Japan Proton Accelerator Research Complex

KEK KEK - High Energy Accelerator Research Organization
K_LEVER K_L Experiment for VEry Rare events

LAV	Large Angle Veto
LEP	Large Electron-Positron Collider
LH	Littlest Higgs model
LHC	Large Hadron Collider
LINAC	LINear ACcelerator
LKr	Liquid Krypton
LYSO	Lutetium-Yttrium oxyorthosilicate
MC simulation	Monte Carlo simulation
MEC	Main Electromagnetic Calorimeter
MPGD	MicroPattern Gas Detector
NA48	North Area 48 experiment
NA62	North Area 62 experiment
OPAL	Omni-Purpose Apparatus for LEP
$\bar{P}$ANDA	anti-Proton ANnihilations at DArmstadt
PC	Personal Computer
PH	Pulse Height
PMT	PhotoMultiplier Tube
PS	Proton Synchrotron
PSD	PreShower Detector
QCD	Quantum ChromoDynamics
RAS - ISSP	Institute of Solid State Physics - Russian Academy of Sciences
RICH	Ring-Imaging Cherenkov detector
SAC	Small Angle Calorimeter
SiPM	Silicon PhotoMultiplier
SM	Standard Model
SPS	Super Proton Synchrotron
TAX	Target Attenuator to eXperimental areas
UV	Upstream Veto
VME	VersaModule Eurocard
VRB	VME Readout Board
VVS	Vacuum Veto System

WLS WaveLength Shifter

LIST OF FIGURES

LIST OF TABLES

BIBLIOGRAPHY

[1] W. Cottingham et al. *An introduction to the Standard Model of particle physics.* Cambridge University Press, 2007.

[2] H. Haber et al. “The search for supersymmetry: probing physics beyond the Standard Model”. In: *Physics Reports* 117.2-4 (1985).

[3] M. Petric. “Flavour-Changing Neutral Currents”. In: *University of Ljubljana, Department of Physics: Seminar and Colloquia* (2008).

[4] A. J. Buras et al. “$K^+ \to \pi^+ \nu\bar{\nu}$ and $K_L \to \pi^0 \nu\bar{\nu}$ in the Standard Model: Status and Perspectives”. In: *Journal of High Energy Physics* 2015.11 (2015).

[5] The NA62 Experiment at CERN. `https://na62.web.cern.ch/na62/Home/Home.html`.

[6] The KOTO Experiment at J-PARC. `http://koto.kek.jp/`.

[7] M. Moulson. *K_LEVER: An experiment to measure BR($K_L \to \pi^0 \nu\bar{\nu}$) at the CERN SPS.* INFN LNF Frascati, 2018.

[8] C. Jarlskog. *CP Violation.* Advanced Series on Directions in High Energy Physics. World Scientific, 1989.

[9] UZH University of Zurich. *The Standard Model.* `https://www.physik.uzh.ch/en/researcharea/lhcb/outreach/StandardModel.html`.

[10] J. F. Donoghue. “The effective field theory treatment of quantum gravity”. In: *AIP Conference Proceedings.* Vol. 1483. 1. 2012.

[11] S. V. Troitsky. “Unsolved problems in particle physics”. In: *Physics-Uspekhi* 55.1 (2012).

[12] H. Arkani et al. “The hierarchy problem and new dimensions at a millimeter”. In: *Physics Letters B* 429.3-4 (1998).

[13] H. Murayama. “Physics beyond the Standard Model and dark matter”. In: *arXiv preprint arXiv:0704.2276* (2007).

[14] B. A. Campbell et al. “Cosmological baryon asymmetry constraints on extensions of the Standard Model”. In: *Physics Letters B* 256.3-4 (1991).

[15] The IceCube Collaboration. “Extremely high energy neutrinos in six years of IceCube data”. In: *Journal of Physics: Conference Series.* Vol. 718. 6. IOP Publishing. 2016.

[16] K. Oide. *Accelerator design for circular high-energy e^+e^- colliders.* `https://www2.kek.jp/accl/seminar/file/HEColliders_Oide_161221.pdf`.

[17] O. Buchmueller et al. "Predictions for supersymmetric particle masses using indirect experimental and cosmological constraints". In: *Journal of High Energy Physics* 09 (2008).

[18] F. Zimmermann. "Future colliders for particle physics - Big and small". In: *Nuclear Instruments and Methods in Physics Research A* A909 (2018).

[19] S. M. Bilenky et al. "Glashow-Weinberg-Salam theory of electroweak interactions and the neutral currents". In: *Physics Reports* 90.2 (1982).

[20] M. Gell-Mann. "The axial vector current in beta decay". In: *Il Nuovo Cimento (1955-1965)* 16.4 (1960).

[21] N. Cabibbo. "Unitary symmetry and leptonic decays". In: *Physical Review Letters* 10.12 (1963).

[22] Y. Nambu. "Axial vector current conservation in weak interactions". In: *Physical Review Letters* 4.7 (1960).

[23] S. Glashow et al. "Weak interactions with lepton-hadron symmetry". In: *Physical Review Letters D* 2.7 (1970).

[24] L. Maiani. "The GIM Mechanism: origin, predictions and recent uses". In: *arXiv preprint arXiv:1303.6154* (2013).

[25] Wikipedia. *GIM mechanism.* `https://en.wikipedia.org/wiki/GIM_mechanism`.

[26] J. L. Rosneret al. "Classical illustrations of CP violation in kaon decays". In: *American Journal of Physics* 69.1 (2001).

[27] M. Kobayashi and T. Maskawa. "CP-violation in the renormalizable theory of weak interaction". In: *Progress of Theoretical Physics* 49.2 (1973).

[28] Wikipedia. *Weak interaction.* `https://en.wikipedia.org/wiki/Weak_interaction`.

[29] L. L. Chau et al. "Comments on the parametrization of the Kobayashi-Maskawa matrix". In: *Physical Review Letters* 53.19 (1984).

[30] L. Wolfenstein. "Parametrization of the Kobayashi-Maskawa matrix". In: *Physical Review Letters* 51.21 (1983).

[31] C. Amsler et al. "Review of particle physics". In: *Physics Letters B* 667.1-5 (2008).

[32] F. C. Correia. "Neutral meson mixing induced by box diagrams in the 3-3-1 model with heavy leptons". In: *Physical Review Letters D* 92.11 (2015).

[33] CKMfitter Group. *Preliminary results as of Summer 2018 (ICHEP 2018 conference).* `http://ckmfitter.in2p3.fr/www/results/plots_summer18/ckm_res_summer18.html`.

[34] G. D'Ambrosio. "Theory of rare K decays". In: *9th International Workshop on the CKM Unitarity Triangle.* Vol. 291. SISSA Medialab. 2017.

[35] G. Isidori. *Recent progress and future prospects in Kaon physics.* `https://www.ggi.infn.it/talkfiles/slides/talk1434.pdf`.

[36] W. Altmannshofer. *The Flavor Puzzle*. https://www.aspenphys.org/science/colloquia/2014_slides/altmannshofer.pdf.

[37] C. Patrignani et al. "Review of particle physics". In: *Chinese physics C* 40.10 (2016).

[38] A. Lai et al. "Measurement of the radiative K_{e3} branching ratio". In: *Physics Letters B* 605.3-4 (2005).

[39] A. J. Buras et al. "K→ $\pi\nu\bar{\nu}$ and ϵ'/ϵ in simplified new physics models". In: *arXiv preprint arXiv:1507.08672* (2015).

[40] M. Moulson. *Prospects to measure BR($K_L \to \pi^0\nu\bar{\nu}$) at the SPS*. Physics Beyond Colliders - CERN, 2016.

[41] The NA48 Collaboration. "The NA48 experiment at the CERN SPS". In: *Nuclear Physics B-Proceedings Supplements* 78.1-3 (1999).

[42] The NA62 Experiment at CERN. *The NA48 CEDAR Detector*. https://na62.web.cern.ch/na62/Documents/Chapter_Cedar_extract_full_doc_v10.pdf.

[43] M. Fiorini. "The P326 (NA48/3) GigaTracker: Requirements and design concept". In: *Nuclear Instruments and Methods in Physics Research A* 572.1 (2007).

[44] The NA62 Experiment at CERN. *The NA62 Straw Tracker Detetctor*. https://na62.web.cern.ch/NA62/Documents/Chapter_StrawTracker_extract_full_doc_v10t.pdf.

[45] A. Del Rosso. *A very cool cooling system for NA62*. https://home.cern/news/news/experiments/very-cool-cooling-system-na62.

[46] E. Cortina Gil et al. "The Beam and detector of the NA62 experiment at CERN". In: *Journal of Instrumentation* 12.05 (2017).

[47] *J-PARC - Japan Proton Accelerator Complex*. https://www.kek.jp/en/Facility/ACCL/J-PARC/.

[48] *KEK - High Energy Accelerator Research Organization*. https://www.kek.jp/en/.

[49] R. Miskimen. "Neutral pion decay". In: *Annual Review of Nuclear and Particle Science* 61 (2011).

[50] T. Yamanaka. *Presentation at the 26th J-PARC Program Advisory Committee*. https://kds.kek.jp/indico/event/28286/contribution/11/material/slides/1.pdf.

[51] S. Su. "Kaon-Scatter introduced backgrounds in the KOTO experiment". In: *Proceedings, Meeting of the APS Division of Particles and Fields: Fermilab, Batavia, Illinois, USA*. 2017.

[52] P. D. Rubin. "Prospects for Measuring BR($K_L \to \pi^0\nu\bar{\nu}$) at CERN SPS". In: *Journal of Physics: Conference Series*. Vol. 770. 2016.

[53] S. Ghithan et al. *Feasibility Study for BioLEIR*. 2017.

[54] The CKMfitter Group. *Studies on rare K decays - EPS 2015 (Preliminary).* 2015.

[55] A. Ferrari et al. *FLUKA: A multi-particle transport code (Program version 2005).* Tech. rep. 2005.

[56] S. Agostinelli et al. "GEANT4 — a simulation toolkit". In: *Nuclear Instruments and Methods in Physics Research A* 506.3 (2003).

[57] J. Beacham et al. *Physics Beyond Colliders at CERN: Beyond the Standard Model Working Group Report.* Tech. rep. Geneva: CERN, 2018.

[58] T. Ladzinski. *SPS - PPS Renovation project impact on North Area and AWAKE.* `https://www.aspenphys.org/science/colloquia/2014_slides/altmannshofer.pdf`.

[59] F. Ambrosino et al. *K_LEVER: An experiment to measure BR($K_L \to \pi^0 \nu\bar{\nu}$) at the CERN SPS.* Tech. rep. arXiv:1901.03099. 2019.

[60] M. Moulson. "K_LEVER: An experiment to measure BR($K_L \to \pi^0 \nu\bar{\nu}$) at the CERN SPS". In: *arXiv preprint arXiv:1812.01896* (2018).

[61] R. Moore et al. "Measurement of pair-production by high energy photons in an aligned tungsten crystal". In: *Nuclear Instruments and Methods in Physics Research B* 119.1-2 (1996).

[62] V. Fanti et al. "The beam and detector for the NA48 neutral kaon CP violation experiment at CERN". In: *Nuclear Instruments and Methods in Physics Research A* 574.3 (2007).

[63] R. Arcidiacono. *Calorimetry in particle physics experiments: the NA48 ECAL example (LKR) - Unit n.9.*

[64] D. A. Morozov et al. "Test beam study of the PANDA shashlik calorimeter prototype". In: *Journal of Physics: Conference Series.* Vol. 160. 1. IOP Publishing. 2009.

[65] G. S. Atoian et al. "Development of Shashlik calorimeter for KOPIO". In: *Nuclear Instruments and Methods in Physics Research A* 531 (2004).

[66] T. Kimble et al. "Scintillation properties of LYSO crystals". In: *Nuclear Science Symposium Conference Record, 2002 IEEE.* Vol. 3. 2002.

[67] E. Ramberget al. "A photon veto detector for the CKM experiment". In: *Nuclear Science Symposium Conference Record, 2003 IEEE.* Vol. 1. 2003.

[68] N. Brene et al. "On the $K_{\mu 3}$ and K_{e3} decay modes". In: *Nuclear Physics* 22.4 (1961).

[69] J. Kepler. *Strena seu de Nive Sexangula.* Frankfurt, Gottfied Tampach, 1611.

[70] R. J. Haüly. *Essai d'une théorie sur la structure des crystaux.* Chez Gogué et Née de la Rochelle, Paris, 1784.

[71] V. Milman et al. *Electronic structure, properties, and phase stability of inorganic crystals: A pseudopotential plane-wave study.* Wiley Online Library, 2000.

[72] J. F. Nye. *Physical properties of crystals: their representation by tensors and matrices.* Oxford University Press, 1985.

[73] U. Hoyer. *Work on Atomic Physics (1912 - 1917).* Niels Bohr - Collected Works. Elsevier Science, 2013.

[74] J. Lindhard. "Motion of swift charged particles, as influenced by strings of atoms in crystals." In: *Physics Letters B* 12 (1964).

[75] E. N. Tsyganov. "Estimates of cooling and bending processes for charged particle penetration through a mono crystal". In: *Fermilab TM-684* (September 1976).

[76] L. Bandiera et al. "Strong reduction of the effective radiation length in an axially oriented scintillator crystal". In: *Physical Review Letters* 121.2 (2018).

[77] W. H. Miller. *A treatise on crystallography.* For J. & JJ Deighton, 1839.

[78] D. S. Gemmell. "Channeling and related effects in the motion of charged particles through crystals". In: *Reviews of Modern Physics* 46 (1974).

[79] J. U. Andersen. "Notes on Channeling". In: *University of Aarhus* (1986).

[80] V. N. Baier et al. "Interaction of high-energy electrons and photons with crystals". In: *Soviet Physics Uspekhi* 32.11 (1989).

[81] H. Yukawa. "On the interaction of elementary particles. I". In: *Proceedings of the Physico-Mathematical Society of Japan. 3rd Edition* 17 (1935).

[82] R. A. Carrigan. *Relativistic Channeling.* Nato Science Series B. Springer US, 2013.

[83] A. I. Sytov et al. "Planar channeling and quasichanneling oscillations in a bent crystal". In: *The European Physical Journal C - Particles and Fields* 76.2 (2016).

[84] W. Scandale et al. "High-efficiency deflection of high energy protons due to channeling along the (110) axis of a bent silicon crystal". In: *Physics Letters B* 760 (2016).

[85] S. Hasan. "Experimental techninque for deflection and radiation studies with bent crystals". PhD thesis. 2012.

[86] H. M. Fried et al. *Vacuum Structure in Intense Fields.* Nato Science Series B. Springer US, 2012.

[87] S. B. Dabagov and L. Palumbo. *Charged and Neutral Particles Channeling Phenomena: Channeling 2008, Erice, Italy, 25 October-1 November 2008.* Vol. 30. World Scientific, 2010.

[88] D. E. Groom et al. "Passage of particles through matter". In: *The European Physical Journal C - Particles and Fields* 15.1-4 (2000).

[89] D. H. Wilkinson. "Ionization energy loss by charged particles part I. The Landau distribution". In: *Nuclear Instruments and Methods in Physics Research A* 383.2-3 (1996).

[90] Y. Tsai. "Pair production and bremsstrahlung of charged leptons". In: *Reviews of Modern Physics* 46.4 (1974).

[91] J. E. Watson et al. "Coherent bremsstrahlung and channeling radiation from electrons of one to three MeV in silicon and gold". In: *Physical Review Letters B* 25.5 (1982).

[92] H. Überall. "High-energy interference effect of bremsstrahlung and pair production in crystals". In: *Physical Review Letters* 103.4 (1956).

[93] J. U. Andersen and E. Laegsgaard. "Critical angles for axial channeling". In: *Radiation Effects* 12.1-2 (1972).

[94] A. H. Sørensen. "Channeling, Bremsstrahlung and pair creation in single crystals". In: *Nuclear Instruments and Methods in Physics Research B* 119 (1996).

[95] P. L. Anthony et al. "Measurement of dielectric suppression of bremsstrahlung". In: *Physical Review Letters* 76.19 (1996).

[96] M. L. Ter-Mikaelian. *High-energy electromagnetic processes in condensed media.* Wiley-Interscience - New York, 1972.

[97] B. Ferretti. "Sulla "Bremsstrahlung" nei cristalli". In: *Il Nuovo Cimento (1943-1954)* 7.2 (1950).

[98] D. R. Mason. "Faster neighbour list generation using a novel lattice vector representation". In: *Computer Physics Communications* 170.1 (2005).

[99] I. MacGregor. "Research with real photons at the MAMI 1.6 GeV electron accelerator". In: *EPJ Web of Conferences* 72 (2014).

[100] A. Apyan. "Computer simulation of coherent interaction of charged particles and photons with crystalline solids at high energies". In: *Nuclear Instruments and Methods in Physics Research B* 255 (2006).

[101] S. Bellucci et al. "Coherent bremsstrahlung and e±-pair production in periodic nanostructures". In: *Nuclear Instruments and Methods in Physics Research B* 234.1-2 (2005).

[102] V. M. Biryukov. "Crystal Channelling in Accelerators". In: *arXiv preprint physics /0607284* (2006).

[103] R. Klein et al. "Channeling radiation measurements at Lawrence Livermore". In: *Nuclear Instruments and Methods in Physics Research B* (1989).

[104] J. C. Kimball et al. "Quantum electrodynamics and channeling in crystals". In: *Physics reports* 125.2 (1985).

[105] V. G. Baryshevski et al. "Synchrotron radiation processes in crystals and polarization phenomena accompanying them". In: *Physics-Uspekhi* 32.11 (1989).

[106] Institute of High Energy Physics. `http://english.ihep.cas.cn/`.

[107] R. Medenwaldt et al. "Detailed investigations of shower formation in Ge-and W-crystals traversed by 40–287 GeV/c electrons". In: *Physics Letters B* 227.3-4 (1989).

[108] N. Charitonidis et al. "The beam lines design for the CERN neutrino platform in the CERN North Area and an outlook on their expected performance". In: *Journal of Physics: Conference Series* (2017).

[109] C. Lefevre. *The CERN accelerator complex*. Tech. rep. 2008.

[110] CERN Engineering Department. *H2 beamline description*. `http://sba.web.cern.ch/sba/`.

[111] CERN Experimental Areas Group. *Overview over CERN SPS test beams*. `https://indico.desy.de/indico/event/18050/session/7/contribution/7/material/slides/0.pdf`.

[112] Princeton Scientific Corporation (Easton, USA). `https://princetonscientific.com/`.

[113] Institute of Solid State Physics (Moscow, Russia). `http://www.issp.ac.ru/engl/`.

[114] D. Lietti. "VISION: a Versatile and Innovative SIlicOn tracking system". PhD thesis. 2015.

[115] S. Bonfanti. "The high resolution silicon telescope of the INSULAB group". MA thesis. Insubria University, Como, 2012.

[116] M. Prest et al. "The AGILE silicon tracker: an innovative γ-ray instrument for space". In: *Nuclear Instruments and Methods in Physics Research A* 501.1 (2003).

[117] HAMAMATSU. *PMT description*. `https://www.hamamatsu.com/eu/en/product/type/H10722-01/index.html`.

[118] T. Kobayashi. "Realization of OPAL electromagnetic barrel calorimeter". In: *Calorimetry in high-energy physics. Proceedings, 2nd International Conference, Capri, Italy, October 14-18, 1991*. 1991.

[119] M. Akrawy et al. "Development studies for the OPAL end cap electromagnetic calorimeter using vacuum photo triode instrumented leadglass". In: *Nuclear Instruments and Methods in Physics Research A* 290.1 (1990).

[120] F. Ambrosino et al. "The large-angle photon veto system for the NA62 experiment at the CERN SPS". In: *Physics Procedia* 37 (2012).

[121] CERN Program Library Long Writeups Y250. *HBOOK*.

[122] CAEN Tools for Discovery. *V1720 8 Channel 12bit 250 MS/s Digitizer description*. `https://www.caen.it/products/v1720/`.

[123] The OPAL Collaboration. "The OPAL detector at LEP". In: *Nuclear Instruments and Methods in Physics Research A* 305.2 (1991).

[124] C. W. Fabjan and F. Gianotti. “Calorimetry for particle physics”. In: *Reviews of Modern Physics* 75.4 (2003).

[125] T. Ferbel. *Experimental techniques in high-energy nuclear and particle physics*. World Scientific, 1991.

IL GUSTO (E IL GIUSTO MODO) DI DIRE "GRAZIE!"

Lasciamo un attimo da parte il formalismo di una tesi magistrale.
Dimentichiamoci per un momento gli orpelli linguistici, gli orrori ortografici, i baroccheggianti *furthermore*, *insofar as* e tutte le deliziose espressioni inglesi che rendono uno scritto di un centinaio di pagine tanto *British* quanto *catchy*. Andiamo oltre i diagrammi di Feynman, i pinguini, il Modello Standard, la compitazione di *bremsstrahlung* e i calorimetri Cherenkov che svapano in un impreciso punto della loro vita ad alta tensione.

Lo abbiamo fatto?
Sicuri?

Bene bene, allora siamo tutti pronti per la parte più importante della tesi: il dirvi il più profondo, il più sentito e più meritato "grazie!" da parte mia. Perchè tutto questo faldone, ma anche colui che lo ha scritto, è sì un po' merito mio, ma soprattutto merito vostro. Sono sincero: siete in tanti, veramente tanti. Perdonatemi fin da ora se dimentico di citarvi di persona in queste righe (cosa già avvenuta nella puntata della triennale, come puntualmente mi ricordano dalla regia), ma state certi che, direttamente o indirettamente, avete il mio più grande "grazie!" di cuore.

Vorrei iniziare dalla mia famiglia. Quella d'origine, quella con cui tutti i giorni respiro, mi ci immergo e mi ci scontro, quotidiamanente ne esco e ne rientro la sera. Grazie ai miei genitori: grazie per il sostegno di questi due anni (ma anche di quelli precedenti), grazie per la pazienza infinita con un ragazzo tremendamente caparbio ed insicuro, per le molteplici lezioni di vita che tutti i giorni riuscite ad insegnarmi. Grazie Pa(olo) per la fiducia, per il voler fare le cose bene, per l'impegno con cui ti preoccupi di noi quattro. E ovviamente grazie per i passaggi in macchina strappati all'ultimo momento. Grazie Mamma. Semplicemente grazie. Perchè l'elenco delle cose per cui ringraziarti sarebbe più lungo della tesi stessa, a voler ben guardare l'argomento nel merito. Sappi che sono servite a tanto le colazioni insieme nei giorni prima di Quantistica III.
Grazie a voi due, ingegneri fino al midollo con cui devastare l'equilibrio familiare durante il pranzo della domenica. La tesi è per voi: non riuscite mai a farmi sentire solo, e questo mi basta. Grazie Ste, perchè riesci a farti voler bene in ogni momento, anche quando vorrei ribaltarti di peso. E perchè sei un punto di riferimento. Grazie Alberto (ma chiamatelo Uzi), per il continuo confronto tra una ripetizione e l'altra in palestra, per la musica classica, per i quadernini del Poli. E perchè sei l'altro punto di riferimento, opposto, reciproco e complementare al primo.
Grazie a miei nonni, Mariuccia e Giuseppe. Gli innumerevoli caffè rubati all'ultimo, le candele accese pre-esame, gli aneddoti e i ricordi di una vita raccontati a pranzo e il

continuo sostegno morale hanno avuto un grande ruolo negli ultimi due anni passati in Università: grazie di cuore!

Grazie alla improbabile famiglia di INSULab: grazie alla mia relatrice, alla Prof.ssa Michela Prest per il grande aiuto in questo lavoro di tesi. Grazie Michela per l'impegno, le infinite correzioni e la tua travolgente passione per la fisica: fanno capire quanto una persona possa essere determinata per raggiungere un obiettivo, quanto uno possa spendersi in qualcosa in cui ci crede realmente.
Grazie al mio correlatore, Dott. Valerio Mascagna: grazie Vale per l'infinita pazienza, i suggerimenti sottili e precisi, le finezze nascoste tra le righe e le immense lacune colmate. E per quella famosa passeggiata in notturna sullo Jura, che ha dato il via a queste pagine.
Grazie Tia, per la stessa passeggiata e per tanti altri dettagli. Oltre ad essere stato un "collega" di laurea e di studi, sei stato soprattutto un grande compagno di avventure in tutti i testbeam trascorsi tra il cemento del CERN, i verdi prati del RAL e le "cacio e pepe" di Frascati (e sulle spiagge dell'Elba, ovviamente: ma lì di test si è fatto poco, concordi?). Hai un grande futuro davanti a te.
Un grande grazie al mitico trio in rosa del laboratorio. Grazie Antonella, l'altra collega: il cartongesso che ci divide non ha impedito di passarne tante insieme, tra alternanze, pon-pon natalizi, improprie presentazioni teatrali sui gas letali, licei vari, piccioni supercorazzati e dimostrazioni di fisica in piazza con improbabili cartelloni sull'astronomia moderna. Grazie per gli appunti passati sottobanco, e per tutte le volte in cui sei stata capace di calmare l'ansia crescente per una qualsiasi scadenza.
Grazie Claudia, per i suggerimenti, la comprensione/compassione in-fi-ni-ta e la condivisione di più di uno stato d'animo. E avermi fatto capire che non sono invincibile di fronte a tutto.
Grazie Chiara, perchè se non ci fossi tu il mondo sarebbe nettamente carente di pazienza, diplomazia e capacità di problem solving tramite sorrisi. Grazie del soprannome, e dei mille consigli sull'autocontrollo in situazioni dove l'autocontrollo non ci azzeccava affatto.
Grazie Luca ed Evgenii, per aver portato una bella ventata di novità all'interno del laboratorio nell'ultimo periodo.
Infine, grazie Erik, per i mille aneddoti, le battute e tutto ciò che sei riuscito ad insegnarmi montando, smontando, rimontando e rismontando tutti i setup sperimentali visti insieme in questi anni.
Grazie anche a voi, Maria, Edo, Ste, Andre, Ale, Gabri e agli altri compagni di università: siamo pochi, è vero, ma è stato comunque bello condividere qualcosa con ciascuno di voi.

Grazie alla mia grande Ohana: tra una cosa e l'altra siete dieci anni di vita, avventure ed amicizie legate a doppio filo con la mia esistenza. E se ho capito cosa vuol dire tenere realmente al bene di qualcuno, anche quando si prendono strade diverse, l'ho capito in gran parte grazie a voi.

Grazie Marta per il sorriso stampato sulle labbra che ci accoglie ogni volta, per il *fil rouge* e le canzoni francesi di altri tempi. Grazie Fede per la tenacia di chi non molla, i caffè mancati al quarto piano e le acute osservazioni del venerdì sera. Grazie Valu per essere il razionale capo di un branco di sbandati, capace di portare ordine e disciplina lì dove serve, e per le passeggiate in montagna. Grazie Silvietta per il calore che porti con te nel ritrovarci insieme, come fossimo ancora compagni di banco. Grazie Cla, imprevedibile nelle tue comparse. Grazie Leo, perchè oltre a condividere l'orizzonte di studi (e della forma fisica) è una vita intera che mi sopporti. Grazie Paolo per i mille consigli, le storie e gli aneddoti più oscuri del mondo legislativo, le lunghe chiacchierate, i manicaretti di capodanno e le sfide a freccette (da estendere anche ai compagni qui attorno). Grazie Eu per le sincere risate nelle lunghe notti al Pirata, al Nelly e al PSV, e per ricordarmi che esiste qualcuno a cui può non piacere camminare, ma è comunque pieno di pregi. Grazie Aqil, per la spontaneità dei tuoi gesti e perchè riesci sempre a sorprenderci ogni volta che si intavola una discussione. Grazie anche ai piccoli del gruppo, a Riccardo e a Sandro, per le serate passate a sopportare i nostri ricordi del Liceo.

Grazie a tutta la grande compagnia olgiatese: a Martina, Daniele, Simo, Ago, Griso e Marco perchè mi hanno accolto così come sono; ai miei ragazzi del '98, del '99 e del nuovo millennio a cui devo tantissimo nel sentirmi ufficialmente un fratello maggiore per qualcuno: grazie per aver sopportato le mie divagazioni scientifiche durante lo studio "matto e disperatissimo" dei campi estivi, tra una passeggiata all'Angeloga e un roverino notturno a Gualdera. E grazie perchè siete una carica di voglia di vivere. Grazie a don Romeo, don Francesco e Andrea, per le serate davanti a una buona tisana, per la pazienza e la fiducia che continuano a mostrarmi.

Grazie alla Co.Ca. e ai ragazzi del gruppo scout Como3, a Lucrezia, Lorenzo, Mattia, Irene, Marta, Federico e tutti gli altri compagni di avventure che mi hanno fatto crescere, e di tanto, in tutti questi anni di gioco. La strada fatta insieme vale tutta la fatica del panorama raggiunto.

Grazie alla Prof.ssa Simona Rolleri, mia insegnante di matematica e fisica per i cinque lunghi anni passati al Terragni. Se può leggere queste righe, sappia che la severità e il rigore con cui ci ha insegnato tutto sono infinitamente trascurabili rispetto alla passione, alla dedizione e al bene che ci ha trasmesso tra i banchi di scuola.

Da ultimo, ma non per importanza, un sentito ringraziamento va alla collaborazione K_LEVER, al Dott. Matthew Moulson e a tutti i suoi partecipanti, per il testbeam fatto insieme, le riunioni e le mail, e per il supporto in questi mesi.

Grazie ancora, a tutti voi, di cuore!

Como, 28 Marzo 2019

G.